8-2016

Characterizing Local Order and Physical Properties of Rare Earth Complex Oxides

Thomas Jacob Shamblin
University of Tennessee, Knoxville, tshambli@vols.utk.edu

To the Graduate Council:

I am submitting herewith a dissertation written by Thomas Jacob Shamblin entitled "Characterizing Local Order and Physical Properties of Rare Earth Complex Oxides." I have examined the final electronic copy of this dissertation for form and content and recommend that it be accepted in partial fulfillment of the requirements for the degree of Doctor of Philosophy, with a major in Nuclear Engineering.

Maik K. Lang, Major Professor

We have read this dissertation and recommend its acceptance:

Haidong Zhou, Joshua R. Sangoro, Brian D. Wirth

Accepted for the Council:

Carolyn R. Hodges

Vice Provost and Dean of the Graduate School

(Original signatures are on file with official student records.)

Characterizing Local Order and Physical Properties of Rare Earth Complex Oxides

A Dissertation Presented for the

Doctor of Philosophy

Degree

The University of Tennessee, Knoxville

Thomas Jacob Shamblin

August 2016

DEDICATION

To my loving wife Aimee and our two perfect “monsters”, Kayden and Liam.

ACKNOWLEDGEMENTS

The research presented in this dissertation was performed in collaboration with Dirk Bosbach, Stuart Calder, Eun Sang Choi, Zhiling Dun, Rodney Ewing, Mikhail Feygenson, Sarah Finkeldei, Maik Lang, Minseong Lee, Weixing Li, Joerg Neuefeind, Maulik Patel, Joshua Sangoro, Caitlin Taylor, Cameron Tracy, Christina Trautmann, Fuxiang Zhang, and Haidong Zhou. I would first like to thank my major professor, Maik Lang, for the guidance he has given me throughout my doctoral studies and for introducing me to several interesting fields of research. I am also indebted to my committee members Joshua Sangoro, Brian Wirth, and Haidong Zhou for their contribution to my research efforts. I have had the pleasure of working with many colleagues and would like to specifically thank Jason Behrens, Stuart Calder, Jacob Cooper, Will Cureton, Zhiling Dun, Rodney Ewing, Mikhail Feygenson, Igor Gussev, Steve Johnston, Joerg Neuefeind, Eric O'Quinn, Raul Palomares, Sulgiye Park, Brandon Perlov, Daniel Schauries, Marcel Toulemonde, Cameron Tracy, Christina Trautmann, Ryan Unger, and Fuxiang Zhang. I am forever indebted to my parents, Tom and Terry Shamblin, along with my sisters, Jessica Winslett and Martha Cate Spencer, for their everlasting support and encouragement. Last, but most certainly not least, I would like to thank my wife Aimee and my two sons Kayden and Liam. Although it has certainly been trying, you have stuck by my side and supported me throughout this entire process. I cannot thank you all enough for the sacrifices you have made for me.

Much of this research was supported by Organized Research Unit funding through the University of Tennessee Office of Research and also by the Material's Science of Actinides, an Energy Frontier Research Center funded by the US Department of Energy, Office of Science, Basic Energy Sciences under Award No. DE-SC0001089. A portion of this research used resources at the High Flux Isotope Reactor and Spallation Neutron Source, a DOE Office of Science User Facility operated by the Oak Ridge National Laboratory. A portion of this work was performed at the National High Magnetic Field Laboratory, which is supported by

NSF Cooperative Agreement No. DMR-1157490 and the State of Florida. Some of this work is based upon data collected at the Cornell High Energy Synchrotron Source (CHESS), which is supported by the National Science Foundation and the National Institutes of Health/National Institute of General Medical Sciences under NSF Award DMR-1332208. This research used resources of the Advanced Photon Source, a U.S. Department of Energy (DOE) Office of Science User Facility operated for the DOE Office of Science by Argonne National Laboratory under Contract No. DE-AC02-06CH11357.

ABSTRACT

With more than 500 compositions, materials possessing the pyrochlore structure have a myriad of technological applications and physical phenomena. Three of the most noteworthy properties are the structure's ability to resist amorphization making it a possible host matrix for spent nuclear fuel, its exotic magnetic properties arising from geometric frustration, and fast ionic conductivity for solid-oxide fuel cell applications. This work focuses on these three aspects of the pyrochlore's many potential uses. Structural characterization revealed that pyrochlore-type oxides have a tendency to disorder from a high symmetry cubic structure to a lower symmetry orthorhombic arrangement in response to a variety of experimental conditions (*i.e.* changing composition, altering stoichiometry, and high-energy ion irradiation). The magnetic properties and structure of orthorhombic Dy_2TiO_5 [dysprosium titanate] have been successfully determined using neutron diffraction. Most notably, Dy_2TiO_5 displays a transition from two-dimensional to three-dimensional magnetic order at temperatures less than 2K and has magnetic moments that can order/disorder independently for each Dy site in response to an applied magnetic field. Broadband dielectric spectroscopy measurements also revealed that ionic conductivity in radiation-induced amorphous $Gd_2Ti_2O_7$ [gadolinium titanate] is more than 250 times larger compared with the crystalline phase. This dramatic increase is caused by a higher concentration of charge carriers coupled with enhanced mobility.

PREFACE

Research pertaining to pyrochlore oxides is largely divided into two fields: studies related to structural properties and those related to physical properties. Following this differentiation, the research described in this dissertation focuses on both aspects of pyrochlores and compositionally related oxides. Chapters I-III present the characterization of disorder in complex oxides by primarily focusing on nuclear applications of these materials (although the importance of the disordering mechanism is key to other research areas such as solid oxide fuel cells, thermal barrier coatings, and magnetic materials). These chapters form a continuous narrative and should ideally be read in order. Chapters IV and V are tailored towards characterizing the magnetic structure of the pyrochlore derivative Dy_2TiO_5 and the ionic conductivity of $Gd_2Ti_2O_7$ amorphized through ion irradiation respectively. While there is certainly relation to Chapters I-III, these two chapters can be viewed as stand-alone sections and could be read without further knowledge.

TABLE OF CONTENTS

LIST OF TABLES

LIST OF FIGURES

INTRODUCTION

Technological Applications

Unlike simple, binary oxides (*e.g.* TiO_2, Al_2O_3), complex oxides typically contain two or more aliovalent cations creating great structural and chemical diversity. Pyrochlore compounds, with the general formula $A_2B_2O_7$, are a class of complex oxides with particular technological importance. More than 500 synthetic compositions have been reported, along with numerous isostructural natural minerals [1, 2]. The A-site can incorporate a range of large cations, including rare earth elements, actinides, and some transition metals, while the B-site incorporates smaller transition metal or Group IV elements (*e.g.* Ti, Ge, Zr, Mo, Hf, Sn, and Pb). This diversity of suitable *d*- and *f*-block constituents leads to unique chemical flexibility in this system, and accompanying structural variation, giving rise to a broad range of applications. For example, the electrical conductivity of pyrochlore materials varies from insulating to superconducting, with some compounds exhibiting semiconductor-to-metal transitions, making them attractive for use in many electrical components [1-5]. The A-site tetrahedral network results in geometric frustration, giving rise to remarkable magnetic properties that are of substantial interest for condensed matter physicists such as the spin-ice state and emergent magnetic monopoles [6-9]. The remarkably low thermal conductivities of pyrochlores makes them candidates for thermal barrier coatings designed to increase the efficiency of gas turbine jet engines [10-14]. Many proposed strategies for the disposal and sequestration of nuclear wastes envision the immobilization of actinides in pyrochlore materials, taking advantage of their chemical durability and radiation tolerance [15-17]. Finally, a number of pyrochlore compounds are considered for use as electrolytes in solid oxide fuel cells due to their high ionic conductivity [18-22].

Structural Disorder in Pyrochlore

The Pyrochlore Structure

Pyrochlores exhibit a cubic unit cell with the *Fd*-3*m* space group [1]. This cell, shown in Figure 1, can be considered a 2×2×2 superstructure of the fluorite unit cell (MO2, *Fm-3m*), consisting of eight fluorite-like subcells. Deviations from the fluorite structure include the presence of two distinct, ordered cation species on the cation sublattice, one eighth of the anions replaced with vacancies, and distortion of the anion sublattice due to relaxation towards the vacant sites. A-site atoms occupy 16*d* sites, and B-site atoms occupy 16*c* sites. Thus, on the cation sublattice, rows of A and B atoms alternate in the [-1 1 0] direction. A-site cations exhibit distorted cubic (scalenohedral) coordination with oxygen, while B-site cations are in octahedral coordination. Oxygen atoms occupy two distinct sites on the anion sublattice. 8*b* sites are coordinated with four A-site cations and occupy ideal fluorite positions. This is often referred to as the "pyrochlore lattice" by the magnetic community as it is one of the most famous sources of geometric frustration (Figure 2). In contrast, the 48*f* anions are coordinated with two A-site and two B-site cations, and are slightly displaced from the ideal fluorite anion sublattice positions. Because all other sites are on fixed positions, the structure of a specific pyrochlore composition is completely described by its unit cell parameter and the fractional coordinate of the 48*f* position on the x-axis. The remaining 8*a* sites are not filled by anions, leaving constitutional vacancies in the structure. These vacant sites are not defects, because they are intrinsic to the structure and are necessitated by the aliovalent nature of these compounds. They do, however, act as a common source of defects in some compositions which makes them strong candidates for ionic conductors in solid oxide fuel cells (discussed later). Pyrochlores can be of either $A_2^{3+}B_2^{4+}O_7^{2-}$ or $A_2^{2+}B_2^{5+}O_7^{2-}$ type.

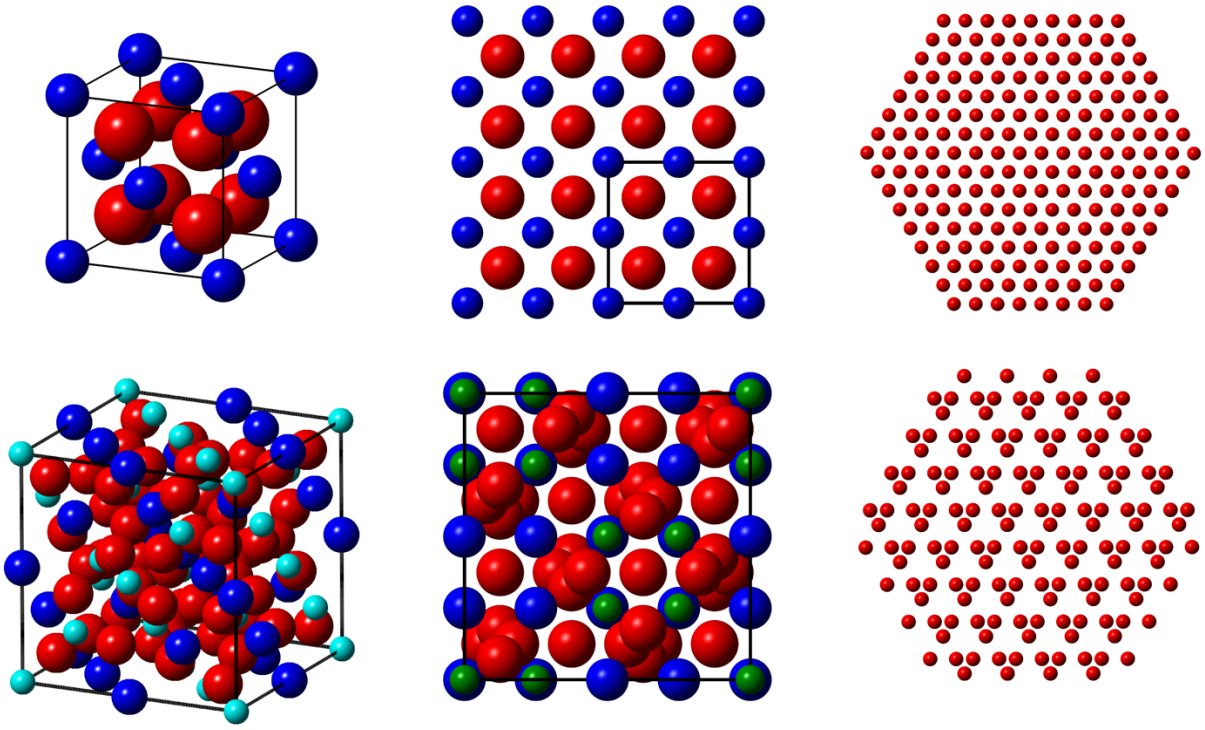

Figure 1: Pyrochlore-to-fluorite relation.

(a) Fluorite unit cell. Blue spheres represent cations, red spheres represent anions, and the black line delineates the unit cell. (b) The fluorite structure viewed in the [100] direction with the unit cell indicated by the black line. (c) The fluorite (222) anion plane. (d) Pyrochlore unit cell with dark and light blue spheres representing the A- and B-site cations, and red spheres representing oxygen. (e) The pyrochlore unit cell viewed in the [100] direction. (f) The pyrochlore (222) anion plane. Oxygen anions are displaced slightly from the fluorite structure positions, and constitutional vacancies are present.

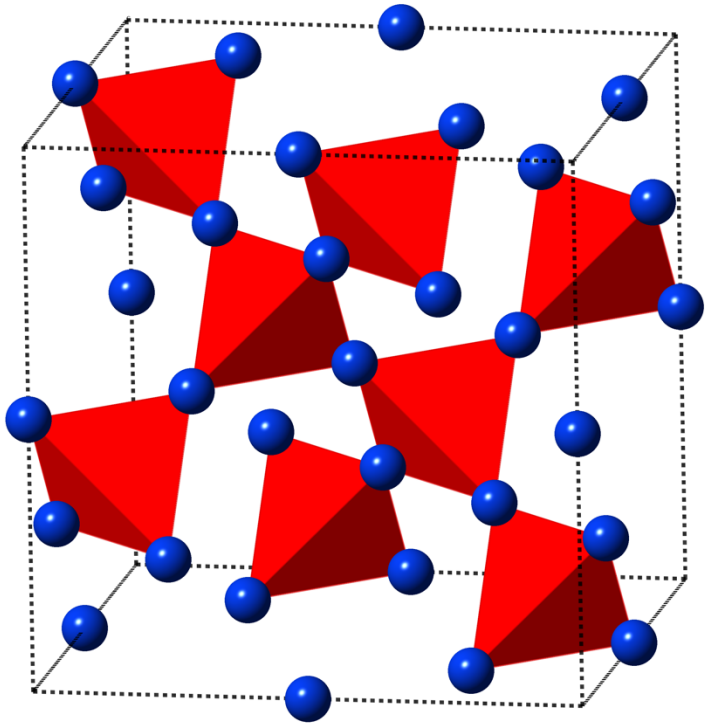

Figure 2: A-site cations form a network of corner-sharing tetrahedra often referred to as the “pyrochlore lattice”.

This tetrahedral motif extends to other structure-types such as spinel.

Current understanding of disorder

Many physical properties are strongly coupled to a materials propensity to accommodate structural disorder. Complex, highly ordered materials such as the pyrochlores are inherently prone to disordering [23]. These structures are unable to incorporate significant defect concentrations without partial or complete loss of long-range order. Because of their structural and compositional complexity, the types of defects exhibited by these compounds are diverse. Displacement of cations from their initial positions into interstitial sites produces Frenkel pairs, the effects of which are different for A- and B-site cations due to differing oxidation states and crystal chemistry. Anti- Frenkel pairs (anion vacancies and associated interstitials) can easily form when oxygen atoms are displaced into nearby 8*a* constitutional vacancies [24]. While the two defect types (Frenkel and Anti-Frenkel) accumulate on the cation and anion sublattices individually, the defects on the anion sublattice affect the coordination of atoms on the cation sublattice (and *vice versa*) due to the short- range effects of ionic-covalent bonding in pyrochlores. Finally, there are antisite defects wherein A- and B-site cations are displaced and exchange positions, producing no vacancies yet reducing pyrochlore superstructure ordering of the cation sublattice. The energetics of these defects varies with pyrochlore composition and particular emphasis has been placed on investigation of antisite defect formation enthalpies [24]. Atomistic simulations have, in general, shown that this formation enthalpy is proportional to the ratio of the ionic radii of the A- and B-site cations, r_A/r_B [25]. When the cations are similar in size, it becomes energetically favorable for them to exchange positions. Experimental evidence shows that when the $r_A/r_B < 1.46$, a disordered fluorite-type structure forms at equilibrium [1, 2]. Using conventional diffraction techniques to characterize the average structure, it has been previously shown that the order-disorder transformation involves the formation of (*i*) antisite defects wherein A- and B-site cations are displaced and randomly exchange positions and (*ii*) randomly distributed anion vacancies [23, 26, 27]. On average, the disordered phase is

therefore analogous to the mineral fluorite (*Fm*-3*m*) with a single cation site (4*a*) and anion site (8*c*) that is 7/8th occupied. The pyrochlore has essentially lost its superstructure and the unit cell parameter is reduced by 1/2. Considering the numerous elements that can occupy the cations sites in pyrochlore materials, these materials are thought to exhibit a great diversity in defect behavior. Consequently, order-disorder transformation dynamics in pyrochlores are complex and, to date, are not fully understood.

Just as many distinct defect types can form in these materials, disordering can proceed *via* several distinct mechanisms. Both the cation and anion sublattices can lose pyrochlore superstructure ordering while still maintaining, on average, fluorite-type order (*via* antisite defect and anti-Frenkel defect formation, respectively) [20]. The disorder modes on the two sublattices are not necessarily coupled, such that order can be lost on one sublattice while it is maintained on the other [20, 26]. This decoupled sublattice disorder is likely linked to a combination of: (i) competing long- and short-range ionic and covalent contributions to bonding, which varies greatly with composition [28] and (ii) differing energetics for cation antisite and anion Frenkel pair defects [24]. In some cases, the formation enthalpy for anion Frenkel pairs is actually exothermic which stabilizes the formation of more expensive cation defects [24]. The pyrochlore-to-fluorite order-disorder transformation represents a unique mechanism by which this class of materials can incorporate a very high defect concentration while still maintaining crystallinity. A small number of structurally- and compositionally-related materials have been shown experimentally to exhibit the same disordering transformation to fluorite, including $A_4B_3O_{12}$ [23] and A_2BO_5 [29-31] compounds which, like the pyrochlore, are superstructures of fluorite. In pyrochlore compositions for which this disorder transformation is not thermodynamically accessible due to, for example, unfavorable antisite defect energetics (large r_A/r_B), similar defect accumulation can instead result in amorphization [23, 25, 32-35]. In these cases, the ordering

characteristics of both the pyrochlore superstructure and the fluorite substructure are lost and the material becomes aperiodic over longer lengthscales.

Interestingly, despite fully disordered cation and anion sublattices in the average structure of disordered fluorite-type materials, recent studies probing the local structure have revealed evidence of non-random distortions at the nanoscale. For example, while the average coordination number (CN) is 7 for both cations in disordered fluorite, Reverse Monte Carlo (RMC) analysis from neutron total scattering [36] and X-ray absorption experiments [37, 38] have shown that the B-site cation CN (6-coordinated in pyrochlore) remains less than that of the A-site cation (8-coordinated in pyrochlore) suggesting that vacancies are still preferentially localized around the B-site cation. It is still unclear, however, from where this local order arises and how it relates to both the fully ordered and disordered phases.

Study of defect formation and disordering in pyrochlores is important for the development of associated technologies because many of these material's unique properties are strongly coupled to defect transport and crystallinity. For example, it has been shown that the rate at which radionuclides are leached from pyrochlore and related nuclear wasteforms can significantly following amorphization [17, 39-41]. Anti-Frenkel pair defects (48*f* oxygen → 8*a* vacancy) promote high-temperature ionic conductivity in these materials, improving their performance as fuel-cell electrolytes [18-20]. Improved understanding of defect dynamics and disordering mechanisms in these materials can enhance their performance in diverse energy-related applications.

Temperature-Induced Disorder

As the temperature of a material increases, the entropy contribution to free energy makes the formation of point defects more favorable. Thermal energy deposited to atoms provides the energy needed for their displacement to interstitial or antisite positions. Pyrochlore is no exception to this rule, and many studies have

observed high temperature order-disorder transformations to a defect- fluorite phase [20, 42, 43]. The transformation temperature, $T_{O\text{-}D}$, varies widely depending on composition, over a range of approximately 900-2700 °C [44]. Because complete disordering to a defect-fluorite structure requires the formation of antisite defects, the energetics of this high- temperature transformation are dependent on the cation ionic radius ratio r_A/r_B [1, 2, 24, 25]. As this ratio decreases and antisite formation becomes energetically favorable, the transition temperature generally drops. For materials with a ratio below 1.46, the pyrochlore superstructure is unstable at ambient conditions and the room temperature phase instead exhibits the defect-fluorite structure. Many pyrochlores with very large ratios, such as $Sm_2Ti_2O_7$ (with the largest r_A/r_B exhibited by a pyrochlore of 1.78) and $La_2Zr_2O_7$, retain the ordered pyrochlore structure up to their melting temperatures [45].

Radiation-Induced Disorder

The interaction of many insulators with energetic particles can be described as highly transient, nanoscale heating events. Ions of low specific energy (~1 keV/amu), such as moderated alpha particles emitted through radioactive decay, interact primarily through elastic collisions with target nuclei, resulting in the transfer of energy to individual, primary knock-on atoms (PKAs). Subsequent collisions of these PKAs with adjacent nuclei result in displacement cascades and localized thermal spikes. At high specific energies (≥ 1 MeV/amu), characteristic of nuclear fission fragments and cosmic rays, energy is deposited primarily through the excitation of electrons along the ion's path. Subsequent transfer of this energy to atoms through electron-phonon coupling results in heating of a cylindrical "ion track" along the particle trajectory, typically several nanometers in diameter and tens of micrometers in length [46]. Radiation in both the nuclear stopping [25, 33, 47] and electronic stopping [48-51] regimes can induce either a pyrochlore-fluorite transformation or amorphization. As with the response of these materials to bulk

heating, the propensity of a pyrochlore to disorder, rather than amorphize, is inversely proportional to its r_A/r_B value. In general, compositions that easily form antisite defects (small r_A/r_B) will disorder to a defect-fluorite phase at relatively low radiation doses, while those for which these defects are unstable will instead amorphize as atoms are displaced to interstitial positions. In pyrochlores with intermediate r_A/r_B values, both transformations have been observed to occur simultaneously. For example, high-energy heavy ion tracks in $Gd_2Ti_2O_7$ and related compounds, shown in Figure 3, exhibit amorphous cores surrounded by disordered, fluorite-structured track shells, which were independently confirmed by high-resolution transmission electron microscopy and molecular dynamics simulations [48, 52, 53].

Swift Heavy Ion Irradiation: Advanced Nanostructuring

In a constant effort to develop advanced technological devices researchers must continually improve material properties beyond what is found in nature. Swift heavy ion irradiation, for example, is a common tool to stabilize far-from-equilibrium phase transformations that could not otherwise be obtained (*i.e.* crystalline → amorphous, crystalline → crystalline) [31, 46, 54-60]. Swift heavy ions interact with a target material through electronic excitation and ionization processes [46]. Dense concentrations of electrons are excited along the ion's trajectory creating a warm electron-hole plasma. The excited electron distributions modify the interatomic potentials resulting in lattice relaxation. Excited electrons subsequently interact with the atomic subsystem through electron-phonon coupling resulting in localized heating which further displaces atoms. If cooling rates exceed recovery rates, a metastable cylindrical region of transformed material known as an ion track may form. Ion tracks are heterogeneous in nature and can range from disordered to amorphous to a mixture of the two which depends on the energy of the incoming ion, the target composition/structure, and the irradiation temperature (see Figure 3).

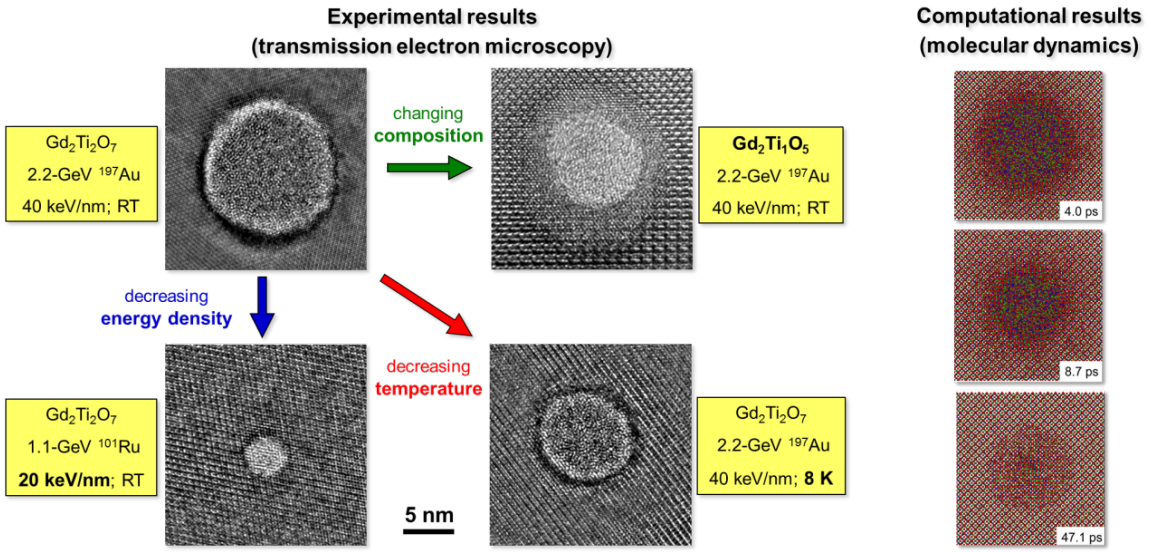

Figure 3: Swift heavy ion tracks in complex oxides.

(left) High-resolution TEM images of GeV-ion tracks in complex oxides under different conditions [46]. Track size and damage morphology can be changed significantly as a function of sample composition (green arrow), irradiation temperature (red arrow), and electronic energy loss (blue arrow). (right) The complex track structure containing non-equilibrium fluorite-type phases is independently confirmed by molecular dynamics simulation. Damage recovery and epitaxial recrystallization at the picosecond time scale determine the final morphology.

The physical properties of these far-from-equilibrium phases remain, for the most part, unexplored largely due to the small samples obtained from irradiation experiments. The limited data available, however, has shown profound effects on important structural and physical attributes. For example, ion tracks in polymers and ceramics can be chemically etched to create nanopores, nanowires, and nanotubes [61, 62]. Ion tracks in superconducting oxides act as flux pinning centers which enhance quantum locking [60, 63]. Ion irradiated $ZnFe_2O_4$ spinel displays spontaneous magnetization within single ion tracks demonstrating that new non-equilibrium magnetic phases can be created with swift heavy ions [64]. It has long been suggested that defects and phase boundaries induced by ionizing radiation could lead to a dramatic increase in ionic conductivity in pyrochlore oxides [34]. This is in agreement with a very recent computational study where it was shown that core-shell ion tracks in $Gd_2Ti_2O_7$ could lead to larger cation-cation spacing within the disordered fluorite ring [65]. This localized strain was shown to lower the activation energy for 48*f*-48*f* ion migration which showed increased the ionic conductivity within these regions.

Experimental Shortcomings for Characterizing Disorder

The order-disorder transformation of pyrochlore is very complex due to the presence of two sublattices (cation and anion sublattice) with distinct defect characteristics. This is further complicated by significant variation in material properties with chemical composition, such as structure-type and mixed bond-types within a single structure (*i.e.*, partial bond covalency). Prior investigations on the disordering process have generally addressed only the resulting long- range cation sublattice modifications, due to the limitation of present analytical techniques (*e.g.*, X- ray diffraction experiments probe long-range order and are only weakly sensitive to anion sublattice structure). It has been experimentally challenging to investigate the local environment of defects, particularly with respect to the two sublattices. Many pyrochlore properties that are critical for their

applications in energy-related technologies are strongly dependent on the atomic-scale defect configuration, such that this gap in understanding is a major hindrance to materials design. New methods for short-range structure determination are now available due to the improved capabilities of DOE user facilities.

For radiation-induced disorder, the applied methods are generally chosen with respect to the details of the irradiation experiment, such as material type and irradiation condition. The diverse responses to ion irradiation require a wide range of characterization techniques, among which X-ray diffraction (XRD) experiments and transmission electron microscopy (TEM) are probably the most utilized. High-resolution TEM provides direct insight into the internal structure of swift heavy ion tracks induced in different complex oxides (for example, amorphous track cores surrounded by defect-fluorite track shells, shown in Figure 3). While the experimentally observed concentric nm-scale damage morphologies have been independently reproduced by molecular dynamics simulations [52], the simulated atomic-scale details of the track structure revealed a much larger degree of complexity in the amorphous and disordered structure [66]. This reflects the shortcomings of TEM to analyze the atomic-scale properties of defects in complex oxides. A TEM contrast is not a ‘picture’ of the atomic positions but the result of the interactions of the electron beam with the material through its entire thickness of a few hundreds nm, which is generally a mixture of crystalline and aperiodic domains inside an ion track. X-ray diffraction data provide useful information regarding the average, long-range structure of irradiated crystalline materials. The analysis of XRD patterns as a function of increasing irradiation fluence is used, for example, to track the decrease of ordering in pyrochlore materials and the concurrent increase in the phase fraction of a disordered or amorphous phase (Figure 4) [53]. Temperature-induced order-disorder transformations are in general analyzed analogously by means of XRD experiments.

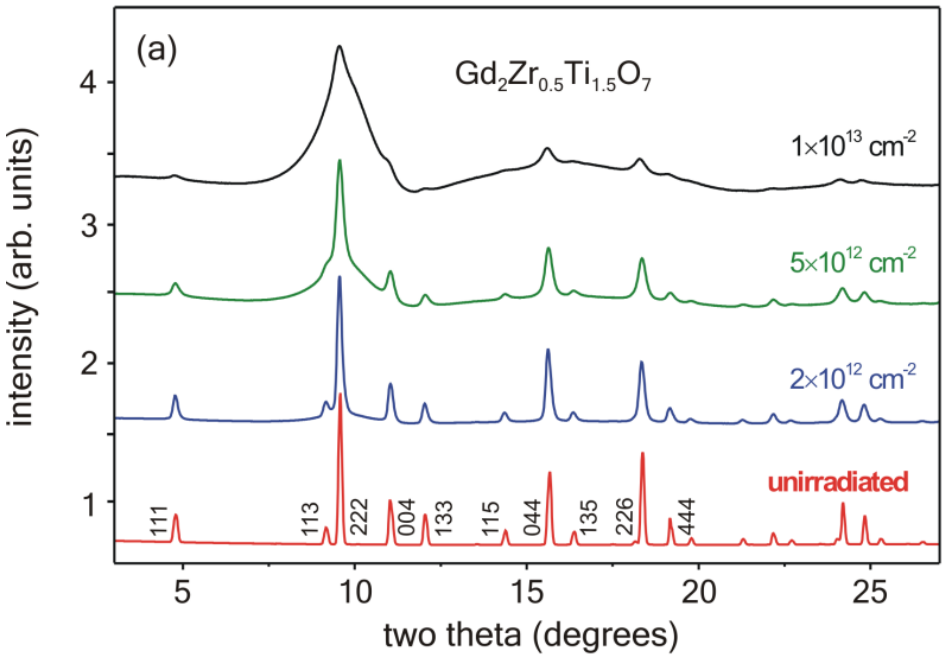

Figure 4: Synchrotron XRD pattern of $Gd_2Zr_{0.5}Ti_{1.5}O_7$ before and after irradiation with 1.43-GeV Xe ions of increasing ion fluence (bottom to top) [53].

The diffuse scattering of the amorphous phase is evident for higher fluences by the increased background. Disorder on the A- and B-cation sites is evident in the intensity of selected diffraction maxima, such as peaks with odd indices (e.g., 111) are produced solely by the ordered pyrochlore structure (super-structure diffraction maxima).

However, there are ***two major shortcomings in the use of XRD and TEM for characterizing radiation effects in complex oxides***:

(i) Due to the weak interaction of X-rays and electrons with low-Z elements, diffraction patterns represent, in general, only the structure of the cation sublattice of a complex oxide containing heavy lanthanide elements. For example, refinement of the XRD patterns in Fig. 4 will only reveal the ion-induced disordering of the Gd, Zr, and Ti cations (A- and B-site elements) with minimal information on the behavior of the oxygen atoms and associated constitutional vacancies in the pyrochlore anion sublattice. Structural information of the anion sublattice is at most indirectly detectable by subtle changes of the XRD patterns, but this often precludes accurate determination of oxygen positions, site occupancies, etc. [26]. This is a major drawback as the oxygen sublattice of pyrochlore oxides plays a critical role in the defect formation and defect migration process during exposure to ion irradiation or high temperature [20, 24, 67]. Other characterization techniques that are sensitive to different sublattices, e.g., Rutherford backscattering, provide in general no detailed information about the defect structure.

(ii) Traditional crystallographic analysis methods such as Rietveld refinement of XRD data neglect elastic diffuse scattering by focusing only on the Bragg peaks resulting from translational symmetry. For well-ordered crystals, this method has proven extremely useful as it extracts important parameters related to the long-range structure (unit-cell parameter, average bond distances/angles, etc.). However, aperiodic defect clusters and the short-range sample structure are not accessible by standard diffraction techniques. As a result, any possible local ordering of “random” defects cannot be detected. The XRD pattern of the irradiated pyrochlore sample in Fig. 4 shows almost entire amorphization at 1×10^{13} ions/cm^2 [68]. However, this reflects only the

loss of long-range order without information on the irradiated sample's local structure. The same drawbacks of standard diffraction experiments apply also if neutrons are used instead of X-rays.

Ionic Conductivity

In addition to their potential nuclear waste form applications, materials adapting the pyrochlore have shown particular promise for use in solid oxide fuel cells. Fuel cells are a broad class of devices that directly convert chemical energy into usable electrical energy [69-71]. These are particularly exciting in light of today's energy climate in that they can be utilized in remote areas with limited access to commercial electricity, have theoretical efficiencies far exceeding that of a combustion engine, and emit minimal pollutants into the atmosphere. Solid oxide fuel cells in particular, primarily consists of four components: the anode, cathode, fuel, and electrolyte. In short, air provides a source of oxygen that is reduced at the cathode to O^{2-} ions. These ions then travel across a solid oxide electrolyte and oxidize the incoming fuel at the anode directly producing an electric current. A central factor governing the performance/feasibility of solid oxide fuel cells (SOFCs) is the ability of the electrolyte to transport oxygen ions from the cathode to the anode (ionic conductivity). In particular, current technology requires that SOFCs operate at high temperatures in order for the electrolyte to efficiently conduct oxygen ions. This creates a problem for the fuel cell in general as few materials can continuously operate at elevated temperatures without structural degradation over time.

In general, ion migration occurs through defects/vacancies in the crystal structure. A perfectly ordered crystal has no available sites for atomic hopping and ionic conductivity is essentially nonexistent. There are consequently two strategies for increasing ionic conductivity: (i) choosing a material with a large concentration of intrinsic defects and (ii) doping a simple metal oxide with a cation of lower valence. Yttria stabilized zirconia (YSZ) is an example of the latter in which $Zr^{4+}O_2^{2-}$

is doped with $Y_2^{3+}O_3^{2-}$. To preserve charge neutrality, each formula unit of Y_2O_3 stuffed into the cubic ZrO_2 structure necessitates one oxygen vacancy:

$$\boldsymbol{Y_2O_3 \rightarrow 2Y'_{Zr} + 3O_O^x + \ddot{V}_O} \quad (1)$$

where Y'_{Zr} denotes a yttrium ion in a zirconium lattice site, O_O^x an oxygen atom and $\ddot{V}_O$ an oxygen vacancy [69]. Oxygen ions can then hop through these compensating vacancies. Thus, doping ZrO_2 with Y_2O_3 dramatically increases the number available charge carriers and YSZ is one of the leading electrolyte candidates for solid oxide fuel cells.

$A_2^{3+}B_2^{4+}O_7$ pyrochlore oxides are particularly interesting for electrolyte materials as many compositions are essentially a combination of (i) and (ii) described above. As mentioned previously, the aliovalent cations require that 1/8th of anion sites with respect to the fluorite structure be constitutionally vacant. However, these vacancies order over specific crystallographic sites without forming a connected network and thus do not significantly contribute to long range ionic conduction. Many pyrochlores, however, have ionic conductivity on the order of YSZ [3, 18-22, 72-79], which is due to intrinsic defects in the 48*f* oxygen sublattice [78, 79]. The ordered vacancies in the pyrochlore structure are the primary source of these defects as 48*f* oxygens can relatively easily "hop" into the constitutionally vacant 8*a* sites creating anion Frenkel pairs. Fast ion conduction can then proceed through the newly created defect in the 48*f* network. Increasing temperature creates additional anion Frenkel pairs which effectively increases the number of charge carriers [20]. Intrinsically disordered pyrochlores (*i.e.,* compositions with inexpensive defect formation energies such as $Gd_2Zr_2O_7$) therefore offer the highest potential for fast ion conduction.

Analogous to experiment, molecular dynamics (MD) simulations have shown that fully ordered pyrochlores do not show ionic conduction and only occurs

when disorder is present on the oxygen sublattice [79]. MD simulations suggest that significant cation disorder, however, increases vacancy migration energies, which suppresses ionic conductivity. Fortunately, disorder on the two sublattices are not necessarily coupled. Through neutron diffraction studies of the $Y_2(Zr_xTi_{1-x})_2O_7$ series, Heremans *et al.* have shown that, in the case of chemical substitution, the disordering process for the anion and cation sublattices are independent, with anion disorder preceding cation disorder as the Zr-content is increased [18]. To further investigate the effect of thermal expansion, Wuensch *et al*. conducted a series of dielectric measurements with complimentary Rietveld analysis of neutron and X-ray powder diffraction to probe the connection between the A- to B-site ionic radius ratio (r_A/r_B), structural disorder (induced both chemically and thermally), and ionic conductivity in different pyrochlore systems [20]. They found that larger thermal expansion of the A^{3+}−O bond length relative to the B^{4+}−O leads to increased distortion of the oxygen sublattice and drives the 48*f* atoms towards the constitutional *8a* vacancy in the pyrochlore structure which increases the intrinsic number of anion Frenkel pairs created. It was also shown that anion disorder precedes cations disorder analogous to chemical substitution. In both cases, increasing disorder on the 48*f* sublattice is the primary source of ionic conductivity.

Many pyrochlore compounds are mixed conductors in which conduction has an ionic component consisting of mobile oxygen interstitials and vacancies and an electron component consisting of mobile electrons in conduction band or holes in the valence band. The predominant conduction mechanism is complex and depends on many factors including the pyrochlores propensity to form anion Frenkel-pair defects, the band gap, the atmosphere, and acceptor/donor impurities to name a few. Harry Tuller's research group at the Massachusetts Institute of Technology has performed a lot of research on mixed ionic/electronic conductivity in pyrochlore and other fluorite-related systems and developed a relatively simple framework for separating conductivity into its individual contributions (ionic, n-type, and p-type) [21, 22, 73-75, 80].

The total conductivity for any given solid oxide material can be expressed as:

$$\boldsymbol{\sigma_{total} = \sigma_i + \sigma_e + \sigma_h} \quad \textbf{(2)}$$

where the subscripts i, e, h refer to conductivity due to charged ions, electrons (n-type), and holes (p-type) respectively. As described previously, ionic charge carriers are formed through anion Frenkel pairs in the oxygen sublattice given by:

$$\boldsymbol{O_O \leftrightarrow V_O^{\cdot\cdot} + O_i^{''}} \quad \textbf{(3)}$$

where $V_O^{\cdot\cdot}$ is a doubly positive charged vacancy on an oxygen site and $O_i^{''}$ is a doubly negative charged oxygen interstitial. For a sample in equilibrium with the external atmosphere additional ionic defects can be created by:

$$\boldsymbol{O_O \leftrightarrow \frac{1}{2}O_2 + V_O^{\cdot\cdot} + 2e'} \quad \textbf{(4)}$$

in which double charged vacancy is created along with 2 electrons. Because of the intrinsic generation of electrons and holes ($nil = e' + h^{\cdot}$), this can equally be expressed as:

$$\boldsymbol{V_O^{\cdot\cdot} + \frac{1}{2}O_2 \leftrightarrow O_O + 2h^{\cdot}} \quad \textbf{(5)}$$

where excess oxygen in the atmosphere annihilates doubly charged vacancies produced a lattice oxygen and 2 holes. Eq. (3) obviously contributes only to ionic conductivity and is not dependent on the external atmosphere. Eq. (4) and (5), however, will produce mixed conductivity. Electron and hole mobility is typically orders of magnitude larger than that of ions or vacancies. So while Eq. (4) and (5) show that the vacancy concentration, which directly affects ionic conductivity, does vary with oxygen in the atmosphere, these vacancies are an insignificant contribution to the total conductivity as they are always accompanied by highly mobile holes or electrons. Ionic conductivity can only dominate when charge carriers are produced *via* Eq. (3). According to Eq. (4) and (5) along with the law of mass action, increasing the oxygen content in the atmosphere will produce a larger concentration of holes which will increase p-type conduction while decreasing the oxygen content will produce more electrons which will increase to

n-type conduction. Given that electroneutrality must always be conserved, one can solve for the concentration of each charge carrier species and obtain the following expression for total conductivity:

$$\boldsymbol{\sigma_{total} = \sigma_i + \sigma_e + \sigma_h = A + B(pO_2)^{-1/4} + C(pO_2)^{1/4}} \quad \textbf{(6)}$$

where the coefficients A, B, and C denote the relative weights of ionic, n-type, and p-type conduction respectively. This derivation is described in more detail in [80]. Eq. (6) can be easily fit to conductivity data as a function of oxygen partial pressure to obtain the ionic/electronic contributions at any given temperature.

While ion/electron transport in homogenous pyrochlore derivatives is well understood, there has recently been an increased interest in creating heterogeneous materials with both regions of both ordered and disordered structures. For example, a 2-3 orders of magnitude increase in total ionic conductivity was observed for mixed pyrochlore/fluorite compositions compared with the ionic conductivity within single grains of either pyrochlore or fluorite structure-types [81]. Finite-element modeling suggests that this is due to dramatically increased migration associated with pyrochlore/fluorite phase boundaries. This increase is thought to be due to a strained region near the interface lowering the energy expended in ion/vacancy hopping [81].

Magnetic Ordering in Stuffed Pyrochlores

Sentence about the third law of thermodynamics and LRMO. Pyrochlores are probably most known for their geometric frustration resulting in exotic magnetic phenomenon such as the spin-ice state and emergent quasiparticles that behave like magnetic monopoles [6-8, 82]. Analogous to cubic water ice, the local point symmetry in spin-ice is incompatible with the average symmetry of the crystal lattice creating a disordered ground state with macroscopic degeneracy (Figure 5).

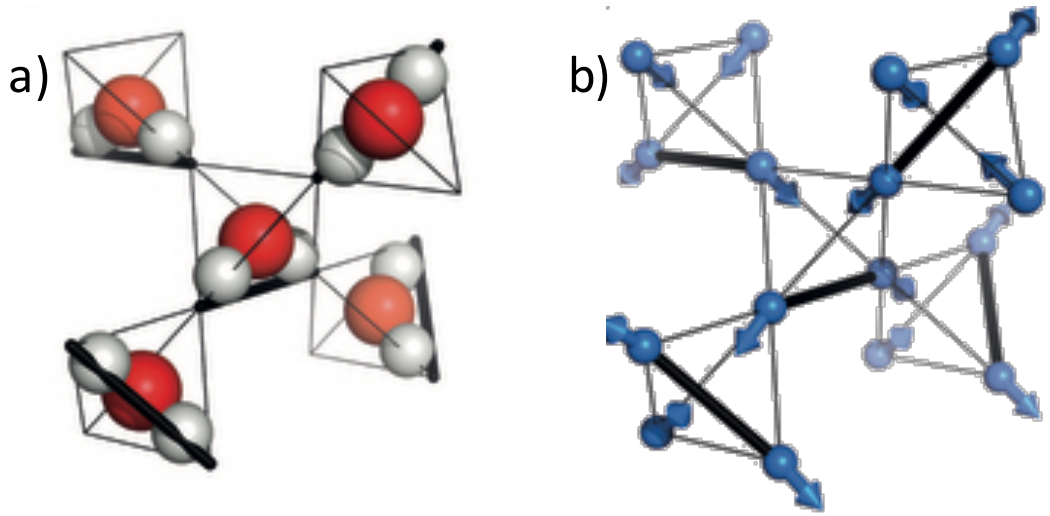

Figure 5: Origin of zero-point entropy in water ice and spin ice.

a) Each oxygen atom sits in the center of a tetrahedron in cubic water ice. Two protons are close to the oxygen while two are further away. b) Magnetic A-site atoms in the pyrochlore spin-ices form an identical network to water ice. Two magnetic moments point in while two point out. Image used with permission from Nature Publishing Group. Adapted from [83].

Magnetic moments in spin-ices follow “ice-rules” developed by Linus Pauling to describe proton disorder in water ice [84]. In cubic water ice, each oxygen is bound to four protons, two covalently and two by weaker hydrogen bonds (Figure 5a). There are many ways of fulfilling this requirement so long as each pair of covalently bound protons in corner sharing tetrahedra does not overlap (bold black lines in Figure 5a). The H_2O molecule within each corner sharing tetrahedra has multiple possible orientations with respect to the H_2O in the central tetrahedra. The total number of possible ground states is approximated as $\sim(3/2)^{N/2}$ where N is the number of water molecules [6, 8]. This degeneracy directly applies to spin orientations in spin-ice (Figure 5b) resulting in a disordered ground state with zero-point entropy. Inverting a single spin in the magnetic lattice creates a pair of emergent quasiparticles with properties analogous to magnetic monopoles [9]. It has recently been shown that the charge and current of these quasiparticles can be measured experimentally [7, 85] essentially creating a new field of research into devices based on “magnetricity” rather than electricity.

Magnetic moments in spin-ice are strongly anisotropic and lie along local $\langle 111 \rangle$ axes [6, 8]. This anisotropy results in a saturation in bulk magnetization measurements at approximately ½ of the expected free moment as the applied magnetic fields are too weak to flip each spin away from its local axis. This spin-ice state is only common to select pyrochlores (*i.e.* $Ho_2Ti_2O_7$ and $Dy_2Ti_2O_7$) and depends on a balance of nearest neighbor exchange interactions, long range dipolar interactions, and the underlying crystal structure. It is therefore fundamentally important to understand how perturbing each of these systems affects the stability of this disordered ground state. For example, it has been previously shown that stuffing additional magnetic Ho^{3+} atoms into the pyrochlore structure ($Ho_2(Ti_{2-x}Ho_x)O_{7-x/2}$) does not appreciably change the zero-point entropy and actually enhances spin relaxation times [86]. This is particularly interesting considering stuffing both increases the connectivity of the magnetic lattice and disorders the crystal structure into a defect fluorite structure at higher values of *x*.

The crystal structure magnetic properties of cubic, fully stuffed pyrochlores (Ln_2TiO_5) have been studied in detail by Lau *et. al.* [87]. None of these materials (Ln = Tb – Yb) showed evidence of magnetic ordering above 2 K. Interestingly, the cubic phase is not the equilibrium polymorph for Ln = Tb and Dy at room temperature and it must be rapidly quenched from a high temperature phase. Magnetization measurements on cubic Dy_2TiO_5 and Ho_2TiO_5 showed little change compared to their parent spin-ice pyrochlore structures ($Dy_2Ti_2O_7$ and $Ho_2Ti_2O_7$) in which the magnetization saturates at ~1/2 of the moment for free Dy^{3+} and Ho^{3+}. This suggests that despite the disordered structure and increased connectivity, the anisotropy for each spin is unchanged from that of the pyrochlore structure.

EXPERIMENTAL METHODOLOGY

Experimental sections are given in the subchapters focusing specifically on the experiments presented there. Here I will give a general introduction on the experimental procedure for characterizing the structure of irradiated and unirradiated materials and magnetic ordering by neutron scattering. This summary may be useful for new graduate students or those with limited background in experimental physics and materials characterization techniques that are interested in using such experiments in their research.

Preparing Samples for Swift Heavy Ion Irradiation and Neutron Total Scattering

Complex, ternary pyrochlore oxides require a fundamentally different analytical strategy to assess their local defect structure and to study how temperature and radiation drive the disordering mechanism. Unlike X-rays, neutrons are highly sensitive to low-Z elements making them ideal probes for the study of complex oxides under extreme conditions, particularly the oxygen sublattice. Due to a low interaction cross-section and relatively small particle flux, neutron scattering experiments require large sample volumes (sample mass of several grams for typical neutron sources) to obtain suitable signal, as compared to X-ray based methods. Irradiated sample quantities that can be produced by typical accelerator facilities (e.g., 20-MV tandem accelerator) are well below the required mass due to the limited penetration depths of such projectiles. Thus, neutron characterization has not been applied in the past to study ion-induced structural modifications in ion irradiated materials. However, the recent completion of the Spallation Neutron Source (SNS) at Oak Ridge National Laboratory (the most intense pulsed neutron source in the world) paired with irradiation experiments at the GSI Helmholtz Center for Heavy Ion Research – one of the world's largest ion accelerator facilities – has now made such experiments feasible.

The Nanoscale-Ordered Materials Diffractometer (NOMAD) beamline requires very little sample amount compared with conventional reactor neutron sources (< 100 mg *vs.* 1-5 g) and opens the door to detailed studies on irradiated materials. Key to this experimental procedure is the use of GeV ions with ranges on the order of 50-100 μm to produce sufficient sample material irradiated with a near uniform electronic energy loss. A new holder system was developed for such experiments to facilitate the preparation of enough material (Figure 6). The sample holders are machined from a 1.2 cm x 1.2 cm aluminum plate by milling a 1 cm diameter depression ($t \approx 70$ μm) into the center. Because the ion range depends on the density, packing fraction, and the sample composition, the required sample mass per holder needs to be calculated for each irradiation experiment to ensure that ions completely penetrate the entire sample thickness. This is done by using the ion range and the *area* of the depression in the aluminum holder, which serves as a circular template for holding the powder in place (depth of milled area is not crucial and must only be deep enough to hold sample). The ion range can be calculated from the electronic energy loss given by the Bethe equation:

$$-\left\langle\frac{dE}{dx}\right\rangle = \frac{4\pi}{m_e c^2}\frac{nz^2}{\beta^2}\left(\frac{e^2}{4\pi\epsilon_0}\right)^2\left[\ln\left(\frac{2m_e c^2\beta^2}{I(1-\beta^2)}\right)-\beta^2\right] \quad (7)$$

where m_e is the mass of an electron, c is the speed of light, n is the electron density of the target, z is the number of electrons in the projectile, β is the ratio of the projectile velocity to the velocity of light, e is the electron charge, ϵ_0 is the vacuum permittivity, and I is the mean excitation potential. Ion range in simply the integral of inverse energy loss. The electron density of the target, n, is determined by:

$$n = \frac{N_A Z \rho_0}{A M_u} \quad (8)$$

where N_A is the Avogadro number, Z is the atomic number, ρ_0 is the density, A is the relative atomic mass and M_u is the molar mass constant.

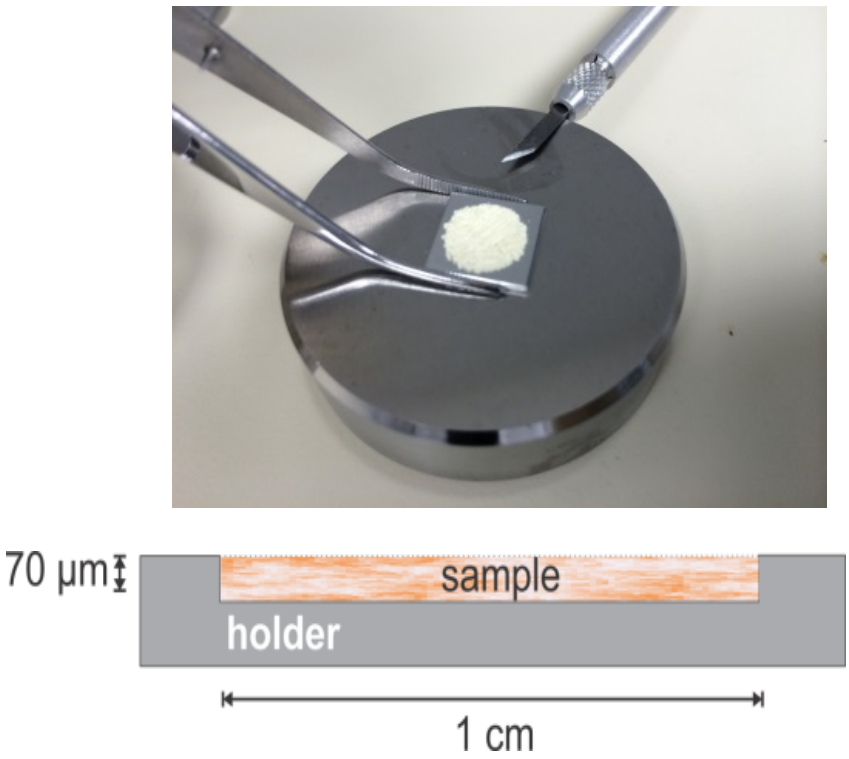

Figure 6: Sample chambers were prepared in a 0.25-mm thick Al holder by milling a circular area of 1 cm diameter to a depth of 70 µm.

Powder was then pressed into the sample chambers between two steel dies with a hydraulic laboratory press. Four holders are typically required to produce one irradiated sample for neutron characterization.

The density in the above equation refers to the density within a single grain, not the bulk material (i.e., pressed powder). Although a powdered sample is obviously less dense than a single crystal, the density within a single grain is close to that of a single crystal. A smaller packing fraction, $\frac{\rho_{bulk}}{\rho_0}$, will only lead to an increase of the range; the energy loss within a single grain remains unchanged.

Instead of directly calculating it from the Bethe equation, both ion range and energy loss can be obtained by the Stopping and Range of Ions in Matter (SRIM) code [88]. Figure 7 shows as an example the electronic energy loss as a function of target depth for 2.2 GeV Au ions in $Er_2Ti_2O_7$ pyrochlores assuming differing packing fractions (Figure 7). The energy loss through the sample is identical for all packing fractions; only the range is changed. Because the packing fraction and range are inversely related, the mass that the ions penetrate is invariant of the packing fraction (Table 1). For a given powder/polycrystalline sample composition, it would be very time consuming (and inaccurate) to estimate the pressed packing fraction and prepare accordingly a customized holder in which the milled thickness is tailored to the ion's range. Since the required sample mass for a neutron scattering experiment does not depend on the packing fraction, the mass of a 1 cm diameter fully dense single crystal must be calculated such that the thickness is equivalent to the calculated range for theoretical density. This mass, which represents the maximum sample amount that can be fully irradiated, can then be evenly dispersed across the circular indentation within the holder independently of the actual packing fraction. To focus only on radiation effects that can be induced by electronic energy loss (i.e., remove potential contributions from nuclear energy loss), the "thickness" of the single crystal used to calculate the mass should be smaller than the ion range. For consistency across different irradiation experiments one should use a fixed ratio of electronic to nuclear energy loss (*i.e.,* 1000) as cut-off criterion when performing the SRIM calculations for each composition.

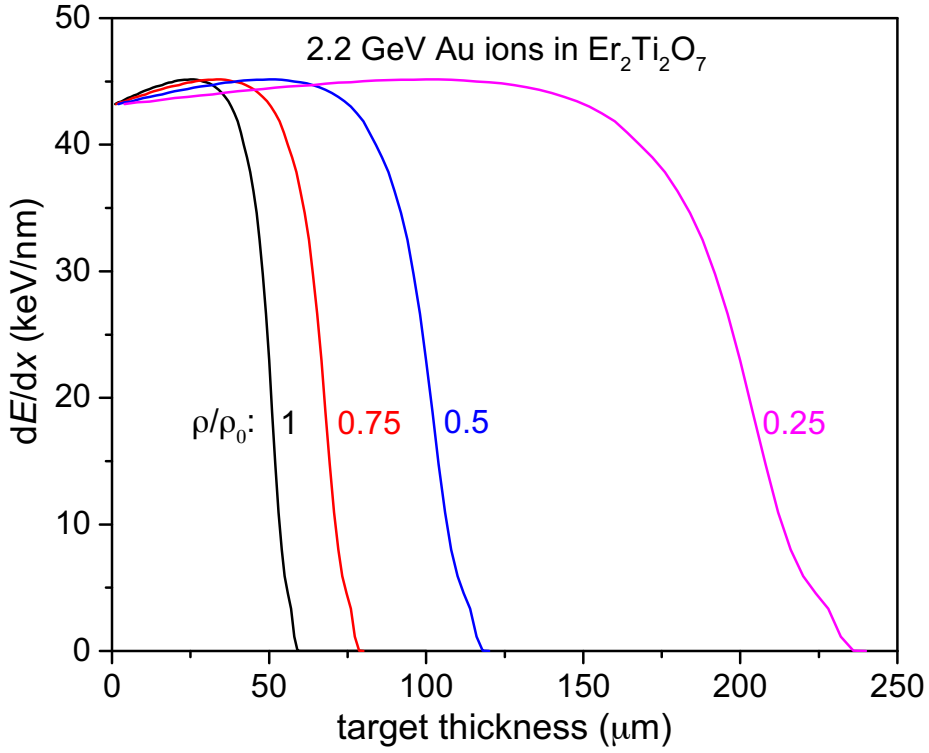

Figure 7: Electronic energy loss as a function of penetration depth for $Er_2Ti_2O_7$ pyrochlore of differing packing fractions.

Table 1: Calculated range and sample mass for 2.2 GeV Au ions in $Er_2Ti_2O_7$ pyrochlore as a function of packing fraction.

ρ_{bulk} (g/cm^3)	ρ/ρ_0	Range (μm)	Sample Volume (cm^3)	Sample Mass (mg)
7.02	1	57.10	44.85	31.48
5.265	0.75	76.13	59.79	31.48
3.51	0.5	114.20	89.69	31.48
1.755	0.25	228.40	179.38	31.48

A more practical approach is to use the drop-off in electronic energy loss which can be accurately determined from its derivative as the first local minimum (Figure 8). This ensures that energy loss variation across the sample is minimal. Regardless of which method is chosen, it is important to maintain consistency across different sample compositions for comparative studies by keeping the energy loss profile identical for all samples. Depending on the sample thickness and ion energy the electronic energy loss profile can show more or less variation. The smaller the sample thickness is compared to the ion range the more homogeneous is the energy loss profile across the sample thickness.

In general, samples for neutron scattering experiments conducted at room temperature at the NOMAD beamline are loaded into 2 mm or 3 mm (outer diameter) quartz capillaries. A larger sample amount can obviously be loaded into the 3 mm capillaries which will usually provide better statistics; however, this is not the case for all compositions due to large absorption cross-sections of specific isotopes (discussed below). Even through the use of the holders in Figure 6 and the high energy ions at GSI, sample mass is still a limiting factor for irradiation experiments and the use of 2 mm capillaries is more practical. For neutron measurements with a beam size of about 8 mm at the NOMAD beamline, it is advantageous to fill the quartz capillaries to a height greater than 1 cm to ensure that the sample fully fills the neutron beam. Powdered samples that have been loaded into quartz capillaries have typical packing fractions of 0.25 – 0.5. For $Er_2Ti_2O_7$ pyrochlore, about 55 to 110 mg of irradiated powder is required to fill a 2 mm capillary to a height of 1 cm, corresponding to 2 to 4 irradiation holders (Fig. 6). The mass required to fill a quartz capillary can be more accurately estimated before the preparation of irradiation samples by loading the same sample material (which will serve later as unirradiated reference sample) into a quartz capillary to a height of 1 cm and measuring the corresponding mass. The number of neutron holders required to reach this desired sample mass can then be calculated accordingly.

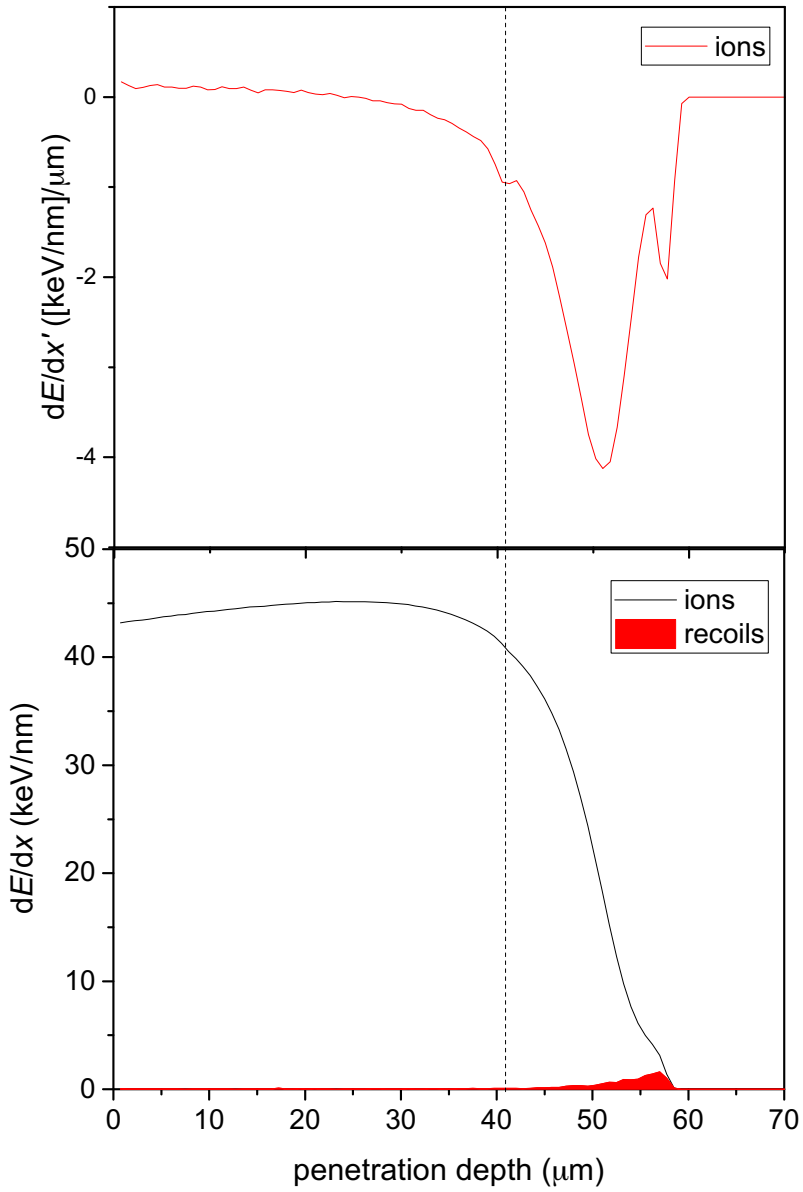

Figure 8: (top) First derivative of electronic energy loss of 2.2 GeV ions in $Er_2Ti_2O_7$. (bottom) Electronic (black line) and nuclear (filled red area) energy loss.

The dotted black line denotes the recommended sample thickness.

Once the mass per irradiation holder and number of holders needed for neutron scattering measurements is determined, the powder is evenly dispersed over the circular indentation (bottom panel of Figure 6). This step provides the highest source for experimental error and great care must be taken to ensure that the sample is uniformly distributed across the indentation. An inhomogeneous sample thickness will lead to a variation of ion penetration depths. This will lead to erroneous energy loss distributions and most importantly could lead to an unirradiated sample fraction (for sample thicknesses that exceed the ion range). Once the sample is evenly distributed, the powder is cold-pressed into the indentation using a hydraulic press and two steel dies. The applied load does not need to exceed 5-6 metric Tons as the powder must only be compacted enough to be stabilized within the sample chamber. After pressing, the samples are typically covered with a 7 μm-thick aluminum foil protect against sample loss during shipping or irradiation. It is important to note that the additional aluminum layer must be accounted for in the SRIM calculation for sample mass per holder. The individual irradiation holders (typically 4 – 9 holders per irradiation experiment) are then fixed to a 5 cm x 5 cm aluminum plate using double sided conductive tape to minimize sample heating during the ion-beam exposure.

After the irradiation experiment, the powders must be removed from the aluminum holders and ground into a fine powder for neutron characterization using the previously described quartz capillaries. Large “chunks” or “sheets” that are obtained from the holders need to be gently ground in a small mortar and pestle. To avoid contamination from the aluminum holder, it is recommended to use a ballpoint tool, which minimizes scratching during sample removal. The finely ground powder can then be easily loaded into the quartz capillaries using a funnel.

Neutron Total Scattering

The methodology presented below pertains to total scattering measurements at the NOMAD beamline of the Spallation Neutron Source at Oak

Ridge National Laboratory [89]. Although neutron total scattering measurements are the focus of this discussion, total scattering can be also performed with high energy X-rays or electrons. Many of these aspects apply for X-rays or electrons accordingly with the difference that neutrons are sensitive to low-Z elements which is essential when analyzing oxide materials. For a more detailed reference, the reader is referred to *Underneath the Bragg Peaks* by Takeshi Egami and Simon Billinge [90] and *The Nanoscale Ordered MAterials Diffractometer NOMAD at the Spallation Neutron Source SNS* by Neuefeind *et al.* [89]; much of the following description was taken from these resources.

The scattering of X-rays, neutrons and electrons by matter can be described by the scattering amplitude:

$$\boldsymbol{\Psi(Q)} = \frac{\mathbf{1}}{\langle \boldsymbol{b} \rangle} \sum_{\boldsymbol{i}} \boldsymbol{b_i e^{iQ \cdot R_i}} \tag{9}$$

where $\boldsymbol{Q}$ is the momentum transfer, defined as the difference in wavevector between the incident and diffracted beam ($\boldsymbol{k}_i - \boldsymbol{k}_f$), b_i is the form factor and $\boldsymbol{R}_i$ the radial position of the i^{th} atom. Unlike x-rays and electrons in which b is strongly dependent on $\boldsymbol{Q}$, the form factor for neutrons is constant and is referred to as the scattering length. Scattering amplitudes cannot be measured experimentally so a diffraction experiment is instead performed by collecting scattered *intensities* (which is a function of the *magnitude* of the amplitude, $|\Psi(\boldsymbol{Q})|^2$) as a function of $\boldsymbol{Q}$. For elastic scattering, $\boldsymbol{Q}$ is simply expressed as:

$$|\boldsymbol{Q}| = \frac{\boldsymbol{4\pi \sin\left(\frac{2\theta}{2}\right)}}{\boldsymbol{\lambda}} \tag{10}$$

with 2θ being the diffraction angle (incident – diffracted) and λ the neutron wavelength. The actual measurement is most commonly done by selecting a fixed wavelength (such as Cu K_α radiation in laboratory X-ray diffractometers) and collecting scattered intensity as a function of 2θ. However, it is equally valid to fix the scattering angle and collect intensity as a function of scattered wavelength. This approach is typical for pulsed spallation sources such as the SNS. Detectors

are placed at fixed angles and distances from the sample and the wavelength of each scattered neutron is measured by the elapsed time to reach each detector, the so-called time-of-flight (*TOF*) measurement. The momentum transfer $\boldsymbol{Q}$ can be obtained applying the *de Broglie* relation:

$$\left(\boldsymbol{\lambda = \frac{h}{p}}\right) \tag{11}$$

where h is Plank's constant and p is the momentum of the neutron. The momentum is simply:

$$\boldsymbol{p = m_n v = m_n \frac{l_i}{TOF}} \tag{12}$$

where m_n is the mass and v the velocity of the neutron and l_i is the associated flight path. Combining Eqs. (6) and (7) with the associated constants into (5) yields:

$$\boldsymbol{|Q| = 3176\ \text{Å}^{-1}\ \mu s/m \frac{l_i}{TOF} sin\left(\frac{2\theta}{2}\right)} \tag{13}$$

which can be used to convert the *TOF* measured at each detector to obtain $\boldsymbol{Q}$ which is the more natural scattering variable and is used directly in the conversion into a pair distribution function (discussed later). Spallation sources do not produce an even distribution of neutron wavelengths and the incident neutron spectrum needs to be characterized. This is typically done in the scattering experiment by normalizing scattered the intensity from the sample to that of vanadium. Vanadium is almost a pure incoherent scatterer (σ_{inc}= 5.08 b while σ_{coh} = 0.0184 b) and the scattering pattern obtained from vanadium therefore reflects the neutron source spectrum. The small Bragg peaks resulting from the minor coherent scattering are typically subtracted prior to normalization.

Experimental Setup/Calibration

Neutron scattering experiments at NOMAD can be split into two sections: (*i*) instrument/source calibration and (*ii*) sample characterization. To obtain

meaningful results on the sample structure, it is important to have a fundamental understanding of the purpose of each step of the measurement and how it pertains to the data collection. An accurate characterization of the background is essential for the conversion of the scattering pattern into pair distribution functions (discussed later). This includes the initial background of the instrument itself (*e.g.*, detectors, structural materials, etc.), as well as the background associated with the sample holder(s) that will be used in subsequent steps. The first measurement at NOMAD is, therefore, to collect scattering data on the instrument itself without a sample or holders beam. Data is typically collected for ~25 minutes, assuming the beam is operating at full power. Detectors at NOMAD are linear ^{3}He detectors each containing 128 pixels. Each pixel corresponds to a specific flight path (length) and scattering angle and therefore records an independent diffraction pattern. An exact knowledge of the position of each pixel is not required as it can be accurately determined through the measurement of a known standard. At NOMAD this is performed with diamond powder by using the (220) reflection to calibrate the $\boldsymbol{Q}$-dependence of each pixel. This is typically the second measurement with a typical exposure time of also ~25 minutes. The diamond powder at NOMAD is held in a vanadium sample can, which requires an additional measurement of an empty can as background for the diamond calibration (again for ~25 minutes). The final step of instrument calibration is to measure a pure vanadium sample (as opposed to the vanadium can that held the diamond powder) to characterize the neutron source spectrum. In general, this takes about 25 minutes and only needs to be performed once for short beamtimes of a day or two. In some cases, particularly after accelerator shutdowns, the source spectrum may change and it is useful to re-measure the vanadium standard again. In summary, 4 individual measurements are required to calibrate the NOMAD instrument before the actual sample is exposed to neutrons: the initial instrument without anything in the neutron beam, the diamond powder, an empty vanadium can, and a pure vanadium rod.

Data Acquisition

Because one diffraction pattern is literally subtracted from another, it is fundamentally important that all sample holder background measurements be as long as the sample measurement itself. For example, if the sample (and holder) is measured for 2 hours, subtracting an empty holder measurement that was only measured for half an hour will introduce the reduced counting statistics from the background measurement into the otherwise good statistics from the sample measurement. Much of the extra time spent measuring the sample is in essence wasted due to the short background measurement. The NOMAD beamline is very versatile in terms of sample holders; common options are 2 mm and 3 mm diameter quartz capillaries, 5 mm diameter NMR tubes and 6 mm diameter vanadium cans. The standard sample environment is an automated sample changer (Figure 9) that can hold ~20 samples depending on the sample size and the temperature can be adjusted between 95 – 500 K.

Once the samples are aligned with respect to the neutron beam (i.e., beam height, lateral position), each sample will then be moved into the beam individually by driving the shifter horizontally to a specific position. The position for each sample can be preset together with exposure time and sample temperature and all samples can be remotely measured without further adjustments. Many standard sample compositions are typically measured for ~1 hour (with additional measurement of an empty tube for the same time). It is in good practice to measure each sample and the empty capillary incrementally in separate 15-30 minute scans and sum the data after the acquisitions have finished. If the background has changed during the course of the beamtime, there is always an empty tube measurement corresponding to that background which can be subtracted.

Figure 9: Samples loaded in 3 mm quartz capillaries onto the automated sample shifter at NOMAD.

Neutron exposure (or counting) time is somewhat of an arbitrary term because the number of neutrons detected depends on the specific operating status/power of the linear accelerator. One hour of counting time at full power (1 MW) would obviously lead to better counting statistics than one hour at 50 % power. The beam may also have intermittent downtime due to accelerator issues (10+ minutes) in which no neutrons are available for scattering. For this reason, each acquisition is typically set to collect a predetermined proton charge rather than a specific exposure time. The conversion between proton charge and counting time at NOMAD is 1×10^9 pC/hour. For example, if a measurement is setup for 30 minutes but the beam is down for 15 minutes during the measurement, the total measuring time will be 45 minutes. Potential downtime of the neutron beam need to be taken into account when planning beamtimes with a large amount of samples or temperature steps as scans can sometimes take longer than anticipated.

Diffraction → Average Structure (or long-range structure)

Although dedicated to produce high resolution pair distribution functions, the NOMAD beamline can also be used to obtain diffraction patterns for Rietveld refinement of long range ordered materials. For the ease of analysis, detector pixels are grouped into 6 “banks” and the measured TOF of each pixel is adjusted to give the TOF that would be measured if all pixels within that bank were at a fixed flight path and scattering angle. The detector banks probe different *d*-spacings of a measured sample, each with differing resolutions (Table 2). Bank 5 offers the highest resolution for structural refinement at the expense of missing low-Q (high *d*-spacing) reflections. For this reason, multiple banks are often refined together which can be important for samples with large unit cells. The diffraction pattern for each bank is refined individually with a set of common constraints between them. In other words, only one refined structure is obtained from including multiple banks.

Table 2: NOMAD detector-bank resolution

Bank	$\langle 2\theta \rangle$ (degrees)	$\Delta d/d$ (Å)	approximate d-range (Å)
1	15	0.029	0.5-13
2	31	0.019	0.3-6.5
3	67	0.0137	0.3-3
4	122	0.0069	0.2-1.9
5	154	0.0036	0.2-1.5
6	7	0.039	0.5-28

Rietveld refinement of diffraction patterns is performed with programs such as Fullprof [91] or GSAS [92] to obtain information regarding the long range structure of a crystalline material (although microstructural features, such as strain and grain size, can also be assessed).

Variations of Eq. (9) which take into account periodic lattices for certain crystal symmetries are explicitly built into the refinement programs to test predicted Bragg reflections against measured scattering intensities. Once a crystal symmetry has been determined (based on the presence or absence of Bragg peaks), the atomic configuration of an ordered crystal can be very accurately determined using traditional refinement of diffraction patterns. Typical parameters that can be determined include the unit cell parameter(s), atomic position(s), thermal motion, grain size, and microstrain among others. This type of analysis fails however when a material does not have a perfectly periodic lattice or has no long range structure at all.

Pair Distribution Function (PDF) → Local Structure (short-range structure)

Many disordered materials (e.g., liquids, glasses, *etc.*) lack long range periodicity, which results in a lack of Bragg reflections in scattering experiments. Only diffuse scattering is observed that cannot be analyzed *via* Rietveld analysis. In such cases, a different strategy must be employed to infer structural properties. Eq. (9) (which gives the scattering amplitude) is simply a Fourier transform of the atomic position therefore, an inverse Fourier transform of the scattering amplitude gives the atomic position directly. As mentioned previously, it is the scattering intensity that is measured rather than the amplitude. The scattering intensity is determined by a differential scattering cross section (defined as the probability of scattering the incoming wave into a solid angle, $d\Omega$):

$$\frac{d\sigma_c(Q)}{d\Omega} = \frac{\langle b \rangle^2}{N}\left|\Psi(Q)^2\right| = \frac{1}{N}\sum_{i,j} b_i b_j e^{iQ\cdot(R_i - R_j)} \tag{14}$$

where R_i and R_j refers to the position of the i^{th} and j^{th} atoms. After normalizing with the appropriate scattering lengths of the atomic constituents of the material, an inverse Fourier transform of Eq. (14) gives a function of atom-pair separation, also known as a pair distribution function (PDF). For powder measurements in which scattering is isotropic, the pair distribution function reduces to:

$$\boldsymbol{G(r) = \int_{Q_{min}}^{Q_{max}} Q[S(Q) - 1] \sin(Qr)\, dQ} \tag{15}$$

where $S(Q)$ is the total scattering structure function which is essentially the scattering intensity that has been normalized to account for the sample composition (scattering lengths, sample density, *etc.*). In practice, one can obtain an effective $S(Q)$ without any knowledge of the sample composition or density [89, 90]. This is done by normalizing the scattering intensity from the sample to that of an incoherent scatterer (e.g., vanadium) using:

$$\boldsymbol{I_{coh} = \frac{I_{sample} - I_{background}}{I_{vanadium}}} \tag{16}$$

where $\boldsymbol{I_{coh}}$ is the normalized coherent scattering intensity from the sample, $\boldsymbol{I_{sample}}$ is the scattering intensity of the sample *and* sample holder, $\boldsymbol{I_{background}}$ is the scattering intensity of an empty sample holder, and $\boldsymbol{I_{vanadium}}$ is the incoherent scattering intensity from a vanadium rod (after small Bragg peaks have been removed). This accounts for the source spectrum (discussed earlier) and automatically corrects for detector coverage, efficiency, *etc.* The function $\boldsymbol{S(Q) - 1}$ is then obtained by normalizing $\boldsymbol{I_{coh}}$ with a polynomial fit of the baseline ($\boldsymbol{I_{poly}}$):

$$\boldsymbol{S(Q) - 1 = \frac{I_{coh} - I_{poly}}{I_{poly}}} \tag{17}$$

to ensure that $S(Q) - 1$ converges to unity at high Q.

A detailed derivation of Eq. (15) can be seen in ref. [90]. The unique advantage of Eq. (15) is that no long range periodicity is required and atom pair separation can be analyzed directly in real space. Ideally speaking, Eq. (15) should be integrated over a Q-range from 0 to ∞ for two reasons. First, diffuse scattering

at high-Q values contains information regarding local distortions in a material. Second, terminating the integration at finite Q-values will cause $G(r)$ to become convoluted with an additional function that is approximately:

$$\boldsymbol{G'(r) = \frac{1}{\pi}\int_0^\infty G(r')\left(\frac{sinQ_{max}(r-r')}{r-r'} - \frac{sinQ_{max}(r+r')}{r+r'}\right)dr'} \quad (18)$$

where Q_{max} is the termination value. This leads to artificial peaks that reduce resolution of sample peaks in $G(r)$ due to broadening. The termination function is similar to a damped sinusoid with a wavelength of approximately $\frac{2\pi}{Q_{max}}$. Experimentally, Q cannot be evaluated from 0 to ∞ and the integral must be terminated at some realistic value for Q_{max}. Increasing Q_{max} reduces the wavelength of these oscillations which become negligible at high enough values of Q_{max}. Details depend on the thermal motion of atoms in the sample but values larger than 25-30 Å are typically sufficient. It is therefore important that the radiation source is capable of even producing scattering data at such large Q-values. Eq. (10) indicates that Q has a maximum value of $\frac{4\pi}{\lambda}$ and therefore requires a high energy radiation source such as synchrotron X-rays or spallation neutron sources that is equipped to collect high-Q scattering.

While originally applied to the study of materials with no long range order at all, PDF analysis is becoming increasingly popular in studying partially disordered crystalline materials. Water ice [84] and Jahn-Teller distorted manganates [93, 94] are two famous examples of materials that only display partial long range order. While Rietveld analysis cannot characterize the resulting diffuse scattering in reciprocal space, the underlying disorder causing it can be directly analyzed in real-space using pair distribution functions.

Atomic correlation functions can be represented in many different ways, the most common of which are the pair distribution function, $g(r)$, the reduced pair distribution function, $G(r)$, and the radial distribution function, *R(r)*. The physical meaning and relation between these functions is described in detail in [90] and will

only briefly be introduced here. The pair distribution function, $g(r)$, represents the probability of finding an atom-atom correlation separated by a distance r. This is extensively used by the liquid/glass community as it overemphasizes low-r correlations. In the reduced pair distribution function, $G(r)$, entire *r*-range is weighted equally and is therefore commonly used for the analysis of partially/fully crystalline materials. $R(r)$ is known as the radial distribution function and is mainly used to calculate coordination numbers. The different PDF formalisms contain the same structural information but present it in different ways. A peak in any of the representations corresponds to an atom-atom correlation. The peak position gives the atomic separation of the atom pair while the peak area is related to the number of pairs (or coordination). The peak area in a properly normalized $R(r)$ directly corresponds to the average number of atoms within the coordination shell. Normalization involves correcting for stronger scattering of specific elements in polyatomic materials and factoring in the sample density and packing fraction. This is difficult in practice because accurate estimations of sample density and packing can be challenging. For this reason, $G(r)$ is probably the most frequently used expression by experimentalists and one can discuss changes in peak area as *relative* changes in coordination.

Small-Box Refinement

Just as diffraction patterns can be refined in reciprocal space (*i.e.,* Rietveld analysis), pair distribution functions can be modeled in real-space. The method employed throughout this dissertation is termed “small-box refinement”. PDFgui is the most widely accessible software for such analysis [95]. In the small-box approach, the structure is modeled as a small “unit-cell” with atom positions defined using fractional coordinates (Wyckoff notation). Using this formalism, crystal symmetry is preserved in the model which can be tested against experimental data. Small-box refinement of PDFs, and in particular the difference curve between the experimental data and the structural model, can provide useful

information regarding local displacements/coordination that is not present in the long range structure. It is therefore recommended that one first analyzes the average structure through Rietveld refinement of diffraction patterns and then uses the obtained structural model to characterize the local correlations in the PDFs. If the quality of fit in the small-box refinement is similar to the Rietveld refinement of the average structure, local distortions/disorder should be minimal. However, if there are significant discrepancies experimental PDF and the long-range structural model, it is likely that the local structure contains short-range correlations that are not periodic over long length scales. These short-range correlations can be determined through the difference curve between the experimental and modeled PDF. Sharp peaks in this difference curve show directly where the short range distortions in the sample are and to what length scale they pertain. A particularly useful strategy for real-space analysis is refining over a series of r-ranges (so-called "boxcar" refinement) which can elucidate the extent of the local distortions. For example, if a fit range of 3 – 13 Å significantly improves the fit compared with a fit range of 1.5 – 11.5 Å, it is likely that short range correlations are confined to nearest neighbors. If the refinement does not improve until higher r-ranges (*i.e.* 7.5 – 17.5 Å) it is likely that the material contains correlated disorder over longer lengthscales.

Magnetic Neutron Diffraction

A basic introduction will be given here to help understand the principles of neutron diffraction to study magnetic ordering. The magnetic moment for an atom is a function of its total angular momentum, $\boldsymbol{J}$, which is the sum of the orbital angular momentum, $\boldsymbol{L}$, and the spin angular momentum, $\boldsymbol{S}$. Atoms/ions with unpaired electrons therefore have intrinsic angular momentum and thus magnetic moment. At high temperatures magnetic materials are usually paramagnetic in which magnetic moments are randomly arranged (disordered). In accordance with the 3rd

law of thermodynamics, cooling to lower temperatures usually causes these randomly oriented moments to become ordered and line up in specific directions.

Because neutrons are spin-1/2 particles they also have an intrinsic magnetic moment. This magnetic moment interacts with the magnetic moments of the atomic constituents of sample. Neutron scattering can therefore be divided into two parts: nuclear scattering (discussed previously) and magnetic scattering. From a practical approach, magnetic scattering is almost directly analogous to nuclear scattering. Disordered (paramagnetic) moments will result only in very broad, diffuse scattering that is often indistinguishable from the background. Periodically ordered magnetic moments (analogous to atoms ordered on a lattice), however, will cause constructive interference and thus Bragg reflections. Locally ordered moments (such as spin-ice) will result in diffuse peaks similar to what is observed nuclear scattering for glasses and other amorphous materials. Just as the scattering length determines the scattering amplitude for nuclear scattering, the magnetic moment determines the amplitude for magnetic scattering. One key difference is that, much like X-ray scattering, the form factor for magnetic scattering is Q-dependent.

Experimental Setup

Magnetic unit cells (and d-spacings) are often larger than structural unit cells which confines magnetic Bragg reflections to the low-Q regions in a diffraction pattern. For this reason, longer wavelength neutrons are typically required to obtain suitable resolution for meaningful analysis. Many diffractometers at Oak Ridge National Laboratory are capable of magnetic characterization. One of the most suited is HB-2a at the High Flux Isotope Reactor because of its versatile sample environment and available neutron wavelengths. For magnetic studies, a wavelength of 2.41 Å is typically selected using a Ge monochromator to probe large d-spacings. Studies of geometrically frustrated rare-earth magnets usually requires temperatures below 2 K, in which case a cryostat with a He^3 insert is used

to reach temperatures down to 0.3 K. Samples are typically held in vanadium cans with a radius ranging from 3mm to 4.5 mm although flat plate holders can be utilized as well. For most measurements, it is recommended to have at least a gram of sample although smaller amounts can be measured if they have large magnetic moments (e.g., Ho and Dy) or at the expense of counting time. In general, at least two measurements are required: one below the magnetic transition and one above. The magnetic transition temperature is ideally determined prior to the neutron measurements using magnetic susceptibility measurements. If sufficient beamtime is available at the neutron source, intermediate temperatures are desired in order to track the intensity of magnetic peaks *vs*. temperature to observe potential saturation of magnetic ordering.

Representational Analysis

The presence of crystal symmetry restricts the number of allowed magnetic states that can exist. The SARA*h* program is a powerful tool that combines the space group of the nonmagnetic phase and experimentally determined magnetic propagation vector, $\boldsymbol{k}$, to determine a set of basis vectors, ψ^{v}, that are symmetrically allowed in the magnetically ordered state [96]. Basis vectors for like atoms can then be linearly combined to give a spin magnitude and direction. SARA*h* drastically reduces the number of allowed states which can then be individually tested against the experimental data to deduce the magnetic structure. This is most easily done through FullProf. SARA*h* creates an output file that contains the allowed basis vectors already formatted as a magnetic phase in FullProf. The coefficients of each basis vector can then be manually adjusted to obtain a reasonable reproduction of the data which can then be refined for more accuracy.

Optimizing Neutron Scattering

Both strongly scattering and strongly absorbing elements can make neutron measurements challenging due to multiple scattering and attenuation respectively.

To minimize multiple scattering for strongly scattering materials, it is a general rule of thumb that the sample thickness be kept below $\frac{1}{\mu}$, where μ is the attenuation coefficient defined as $n_s\sigma$. Unfortunately, samples that include isotopes with excessively large neutron absorption cross sections (such as natural Gd) cannot be measured with neutron diffraction. Many highly absorbing elements, however, that also have large scattering lengths (*e.g.,* Dy) can still be characterized if the thickness is optimized. The fraction of neutrons transmitted through a sample, $\frac{I}{I_0}$, can be expressed as:

$$\frac{I_T}{I_0} = e^{-\sigma_a n_s t} \tag{19}$$

where σ_a is the neutron absorption cross-section, n_s the atomic density, and t the sample thickness. Likewise, the fraction of neutrons that are scattered by the sample, $\frac{IS}{I_0}$, is:

$$\frac{I_s}{I_0} = 1 - e^{-\sigma_s n_s t} \tag{20}$$

where σ_s is the scattering cross section. The fraction of neutrons that are scattered *and* transmitted is then simply:

$$\frac{I_{ST}}{I_0} = e^{-\sigma_a n_s t}(1 - e^{-\sigma_s n_s t}) = e^{-\sigma_a n_s t} - e^{-(\sigma_a+\sigma_s) n_s t}. \tag{21}$$

For highly absorbing samples, the sample thickness, t_{opt}, can be optimized according the chemical composition to obtain the maximum fraction of scattered neutrons that are also transmitted (not absorbed) by taking the differential and setting it equal to 0 to obtain:

$$t_{opt} = \frac{\ln(\sigma_a+\sigma_s) - \ln(\sigma_a)}{n_s\sigma_s}. \tag{22}$$

The sample thickness can vary as a function of scattering angle (particularly for flat plate holders). For thicker samples this may need to be accounted for but in general Eq. (22) provides a close approximation of the optimum size. For

polyatomic samples, it is most practical to calculate a weighted average cross section and atomic density for the sample. Many cross sections that are readily available are given for thermal neutrons (λ = 1.8 Å) so it is important to make sure that these are “corrected” to the specific to the wavelength used in the experiment. For constant wavelength experiments, such as those performed at reactor sources (such as the Hb-2a beamline at HFIR), this is easily performed as cross sections are generally scaled linearly with wavelength at low energies. This is more complicated at spallation sources and usually involves the use of computer programs.

CHAPTER I

STRUCTURAL RESPONSE OF TITANATE PYROCHLORES TO SWIFT HEAVY ION IRRADIATION

A version of this chapter has previously been published by Jacob Shamblin, Cameron L. Tracy, Rodney C. Ewing, Fuxiang Zhang, Weixing Li, Christina Trautmann, Maik Lang in the journal *Acta Materialia*:

Shamblin, J., et al. (2016). "Structural response of titanate pyrochlores to swift heavy ion irradiation." Acta Materialia **117**: 207-215.

R.C.E. and M.L. conceived the experiment, F.Z. synthesized the samples, C.T. performed the irradiations, C.L.T., F.Z., and M.L. collected the data, J.S. analyzed the data and wrote the manuscript.

Abstract

The structure, size, and morphology of ion tracks resulting from irradiation of five different pyrochlore compositions ($A_2Ti_2O_7$, A=Yb, Er, Y, Gd, Sm) with 2.2 GeV ^{197}Au ions were investigated by means of synchrotron X-ray diffraction (XRD) and high-resolution transmission electron microscopy (HRTEM). Radiation-induced amorphization occurred in all five materials analyzed following an exponential rate as a function of ion fluence. XRD patterns showed a general trend of increasing susceptibility of amorphization with r_A/r_B with the exception of $Y_2Ti_2O_7$ and $Sm_2Ti_2O_7$. This indicates that the track size does not necessarily increase with r_A/r_B, in contrast with results from previous swift heavy ion studies on $Gd_2Zr_{2-x}Ti_xO_7$ pyrochlore materials. For $Y_2Ti_2O_7$, this effect is attributed to the significantly lower density of this material relative to the lanthanide-bearing pyrochlores, thus lowering the electronic energy loss (dE/dx) of the high-energy ions in this composition. An energy loss normalization procedure was performed which reveals an initial increase of amorphous track size with r_A/r_B that saturates above $Gd_2Ti_2O_7$. This is in agreement with previous light ion irradiation experiments and first principle calculations of the disordering energy of titanate pyrochlores indicating that the

same trends in disordering energy apply to radiation damage induced in both the nuclear and electronic energy loss regimes. HRTEM images indicate that single ion tracks in $Yb_2Ti_2O_7$ and $Er_2Ti_2O_7$, which have small A-site cations and low r_A/r_B, exhibit a core-shell structure with a small amorphous core surrounded by a larger disordered shell. In contrast, single tracks in $Gd_2Ti_2O_7$ and $Sm_2Ti_2O_7$, have a larger amorphous core with minimal disordered shells.

Introduction

Swift heavy ion tracks in pyrochlores are complex and often consist of several distinct, concentric damage zones (*i.e.,* amorphous track core, with disordered fluorite and defect-rich pyrochlore shells) [48, 49, 53, 97]. The pyrochlore cation ionic radii ratio (r_A/r_B) directly influences the stability of the pyrochlore phase relative to metastable defect-fluorite and amorphous phases, and in turn susceptibility of these materials to irradiation-induced loss of the ordered structure of pyrochlore. More radiation resistant compositions (smaller r_A/r_B) tend to disorder under irradiation to a defect-fluorite structure, but still maintain their crystallinity, while more susceptible compositions (larger r_A/r_B) tend to amorphize [25, 32, 97, 98]. For compositions with intermediate radiation tolerance, the relative cross-sectional areas of the amorphous track core and disordered track shell vary with the cation ionic radius ratio. From a structural point of view, variation in r_A/r_B strongly affects the ability of these materials to incorporate defects into their structure, which is governed by the defect formation energy [25]. If the antisite formation energy is small (A- and B-site cations of similar size, minimizing the structural distortion associated with their site exchange), the cations can readily exchange sites. Along with the displacement of oxygen to 8*a* constitutional vacancies, this yields a disordered, defect-fluorite structure. When the antisite formation energy is high (*i.e.* the A-site cation is significantly larger than the B-site cation), a disordered phase incorporating these defects becomes

energetically unfavorable relative to an amorphous phase and the long-range, atomic-scale periodicity of the structure is lost.

This r_A/r_B dependence of pyrochlore radiation tolerance has been confirmed experimentally for irradiations with both low-energy ions (which deposit energy to a material via elastic nuclear collisions) [32, 33, 98] and high-energy ions (which deposit energy *via* electronic energy loss) [48, 50, 53, 68, 99]. Pyrochlore compounds with relatively large B-site cations (smaller r_A/r_B), such as zirconium, tend to disorder in response to irradiation while those with smaller B-site cations (larger r_A/r_B), such as titanium, instead become amorphous [16, 32, 48, 49, 53, 97]. For swift heavy ions, in particular, the relevance of this point defect-based description to phase behavior within the ion-solid interaction regions is unclear, considering the dense ionization and extreme energy densities typical of the transient energy deposition and "heating" processes. Recent complementary experimental and molecular dynamics (MD) simulations have shown that the complex track structure may be the result of the rapid quenching of a previously molten phase [52, 100, 101]. Formation of the high-temperature defect-fluorite polymorph, that is thermodynamically accessible for low r_A/r_B compounds, is kinetically favored during the quenching process, compared with the more highly-ordered pyrochlore phase. Formation of the disordered phase is energetically unfavorable for compounds with a large r_A/r_B, resulting in amorphization. The diffusion of thermal energy in the radial track direction during quenching and the stabilizing effect of the liquid-solid interface at the track edge on the epitaxial formation of the defect-fluorite phase leads to the unique core-shell morphology of ion tracks in pyrochlore materials.

The size and damage morphology of ion tracks in insulators depends on the energy loss (dE/dx) [48, 97], ion velocity [59], and the chemical composition of the target [32, 49, 57]. For pyrochlores in particular, the effect of chemical composition has typically been studied by replacing the B-site cation to alter the r_A/r_B [48, 49, 51, 53, 97, 101]. The $Gd_2Zr_{2-x}Ti_xO_7$ solid solution series ($1.46 \leq r_A/r_B \leq 1.74$) has

been extensively studied and the size of the amorphous track core has been shown to decrease as smaller Ti is replaced by larger Zr at the B-site [48, 49, 53, 97]. The smaller amorphous cores in Zr-rich compositions are surrounded by larger defect-fluorite shells. While the effects of B-site cation substitution are well studied, the effect of changes to the A-site composition has not been adequately addressed. In this systematic study, we investigate the response of the $A_2Ti_2O_7$ (A = Yb, Er, Y, Gd, Sm) series to 2.2 GeV ^{197}Au ion irradiation with particular emphasis on amorphization resistance and track morphology.

Experimental Methodology

Polycrystalline samples of $A_2Ti_2O_7$ (A = Yb, Er, Y, Gd, and Sm) were investigated to cover a range of r_A/r_B, providing a steady, incremental change in A-site cation ionic radii due to the lanthanide contraction. Yttrium was included to assess the importance, if any, of lanthanide 4*f* orbitals to the radiation response. The pyrochlore samples were synthesized *via* the solid-state reaction method from the binary oxides (A_2O_3 and TiO_2). Powders were mixed using a mortar and pestle in an acetone slurry and pressed into pellets with a hydraulic press which were fired at 1200 ºC for 20 hours. The pellets were then reground, pressed, and fired at 1400 ºC for an additional 20 hours. The final pellets were ground into fine powders (grain size ~ 1 μm) and uniaxially pressed into 40-μm thin platelets with a hydraulic press (surfaces were approximately 3 mm in diameter). The samples were then sintered in a furnace for 24 hours at 800 °C to stabilize the platelets and remove any adsorbed water. All starting samples were characterized prior to irradiation by X-ray diffraction. Analysis showed that all compositions contained only the pyrochlore phase with no observable impurities. The irradiation experiments were completed at room temperature at the X0 beamline of the UNILAC linear accelerator at the GSI Helmholtz Center in Darmstadt, Germany using 2.2 GeV ^{197}Au ions. Irradiation was completed for nine ion fluences ranging from 5×10^{10} to 3×10^{13} ions/cm^2. The projected range for the ^{197}Au ions was

determined using the Stopping Power and Range in Matter code (SRIM) and was about 20 μm larger than the 40 μm thickness for all samples (Figure 10) [88]. The energy loss (d*E*/d*x*) due to nuclear collisions is several orders of magnitude less than the electronic energy loss across the entire sample and was therefore neglected. The mean electronic d*E*/d*x* for all compositions and the variation over the 40-μm thick samples were determined with the SRIM code assuming theoretical density and are summarized in Table 3 and displayed in Figure 10. The plot shows that ions passed through with nearly constant energy loss. The actual density can be assumed to be lower but this doesn't affect the energy loss within the grain and only extends the range [102].

The B2 beam line at the Cornell High Energy Synchrotron Source (CHESS) at Cornell University was utilized for angle-dispersive powder XRD measurements. The beam energy was 25 keV (λ = 0.496 Å) with a spot size of 0.5 mm. All samples were measured in transmission mode and the Debye diffraction rings were recorded using a MAR CCD detector. The two-dimensional MAR images were processed into one-dimensional X-ray diffraction patterns using the FIT2D software [103]. The XRD pattern analysis was completed using the software DatLab [104] focusing on the determination of the fluence-dependent crystalline and amorphous phase fractions. Relative amorphous sample fractions were determined by deconvoluting XRD signal into both crystalline (consisting of ordered pyrochlore and disordered, defect-fluorite) and amorphous contributions following a methodology that is described in detail elsewhere [51].

High-resolution transmission electron microscopy images (HRTEM) were taken in a FEI Tecnai G2 F20 X operated at 200 keV at Stanford University to study the morphology of ion tracks in $Sm_2Ti_2O_7$, $Y_2Ti_2O_7$, $Er_2Ti_2O_7$, and $Yb_2Ti_2O_7$. HRTEM images were recorded under top-view conditions with the electron beam parallel to both the ion tracks and a major zone axis of the sample. The fluence for TEM samples was limited to $3x10^{11}$ ions/cm^2 to prevent track overlap.

Table 3: Chemical composition, ratio of cation ionic radii (r_A/r_B), unit cell parameter (*a*), calculated density (ρ_{calc}), electronic energy loss (d*E*/d*x*), extracted amorphous track diameters (XRD d_a), and track diameters normalized by (d*E*/d*x*)^2 for (Normalized XRD d_a) for titanate pyrochlores studied.

Composition	r_A/r_B	a = b = c (Å)	ρ_{calc} (g/cm^3)	(*d*E/*d*x) (keV/nm)	XRD d_a (nm)	Normalized XRD d_a (10^{-3} nm^3/keV^2)
$Yb_2Ti_2O_7$	1.63	10.23130(6)	6.87	42.5 ± 0.7	5.66 ± 0.46	3.13 ± 0.27
$Er_2Ti_2O_7$	1.66	10.28530(6)	6.61	41.8 ± 0.6	5.70 ± 0.45	3.26 ± 0.26
$Y_2Ti_2O_7$	1.68	10.3004(2)	4.69	35.7 ± 0.9	4.62 ± 0.40	3.62 ± 0.34
$Gd_2Ti_2O_7$	1.74	10.3861(1)	6.18	40.2 ± 0.6	6.23 ± 0.47	3.85 ± 0.30
$Sm_2Ti_2O_7$	1.78	10.4482(1)	5.92	39.1 ± 0.5	5.90 ± 0.51	3.86 ± 0.34

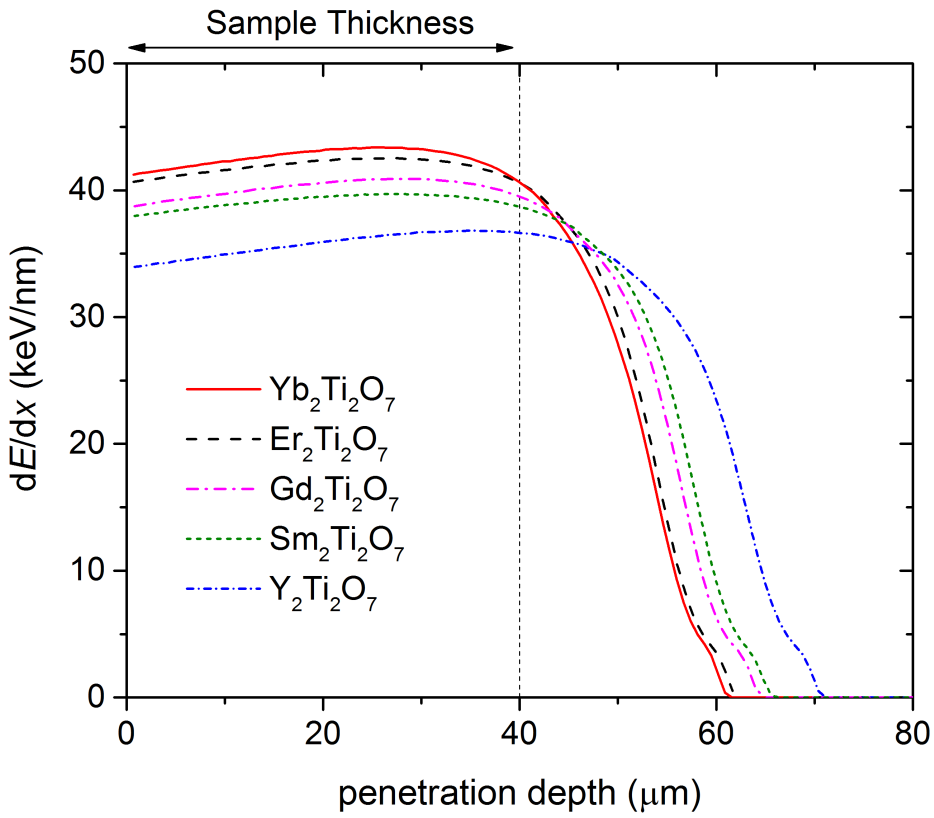

Figure 10: Electronic energy loss (d*E*/d*x*) of 2.2 GeV ^{197}Au ions as a function of ion penetration depth in various titanate pyrochlores.

Note that the d*E*/d*x* in $Y_2Ti_2O_7$ is noticeably reduced due to its relatively low density (Table 3). The vertical dashed line represents the thickness of the samples used in this study, showing that all ions passed completely through these samples with relatively constant electronic energy loss.

The samples were thinned down for TEM studies by polishing and subsequent ion milling from the surface opposite to the ion irradiation. Tracks in all studied materials are very stable when subjected to electron beams at low magnifications and even at HRTEM mode. Therefore, sample modification due to the electron beam can be neglected.

Results

Synchrotron X-Ray Diffraction

Radiation-induced amorphization is evident in the XRD patterns by the reduced intensity of the crystalline diffraction maxima and a simultaneous increase of diffuse scattering bands with increasing ion fluence. These scattering bands, arising from the amorphous phase, are centered at $2\theta \approx 9.5°$, $2\theta \approx 15°$, and $2\theta \approx 19°$ (see corresponding patterns in Figure 11. The third scattering band was omitted for clarity). The onset of amorphization in the XRD patterns is first evident at a fluence of 1×10^{12} ions/cm^2 for A = Sm, Gd, Er, and Yb and 2×10^{12} ions/cm^2 for A = Y. It is difficult to qualitatively determine a trend across the lanthanide titanate series as the variation in radiation response with composition is minor. However, the ratio of amorphous to crystalline scattering intensity is, at any given fluence, greater for A = Sm, Gd than for Er, Yb. This is most evident at an ion fluence of 5×10^{12} ions/cm^2, for which $Sm_2Ti_2O_7$, and $Gd_2Ti_2O_7$ show a more pronounced diffuse contribution to the (222) peak relative to $Er_2Ti_2O_7$ and $Yb_2Ti_2O_7$ (Figure 11). Unlike the larger lanthanide A-site cations, $Er_2Ti_2O_7$ and $Yb_2Ti_2O_7$ also show some residual crystallinity at an ion fluence of 8×10^{12} ions/cm^2, as indicated by a sharp shoulder within the broad amorphous peak. These results show that amorphization proceeds more rapidly with increasing fluence when larger cations (Gd and Sm) occupy the pyrochlore A-site instead of smaller cations (Yb and Er). $Y_2Ti_2O_7$, which has an A-site cation ionic radius between Sm and Yb, was by far the most radiation tolerant composition of the series.

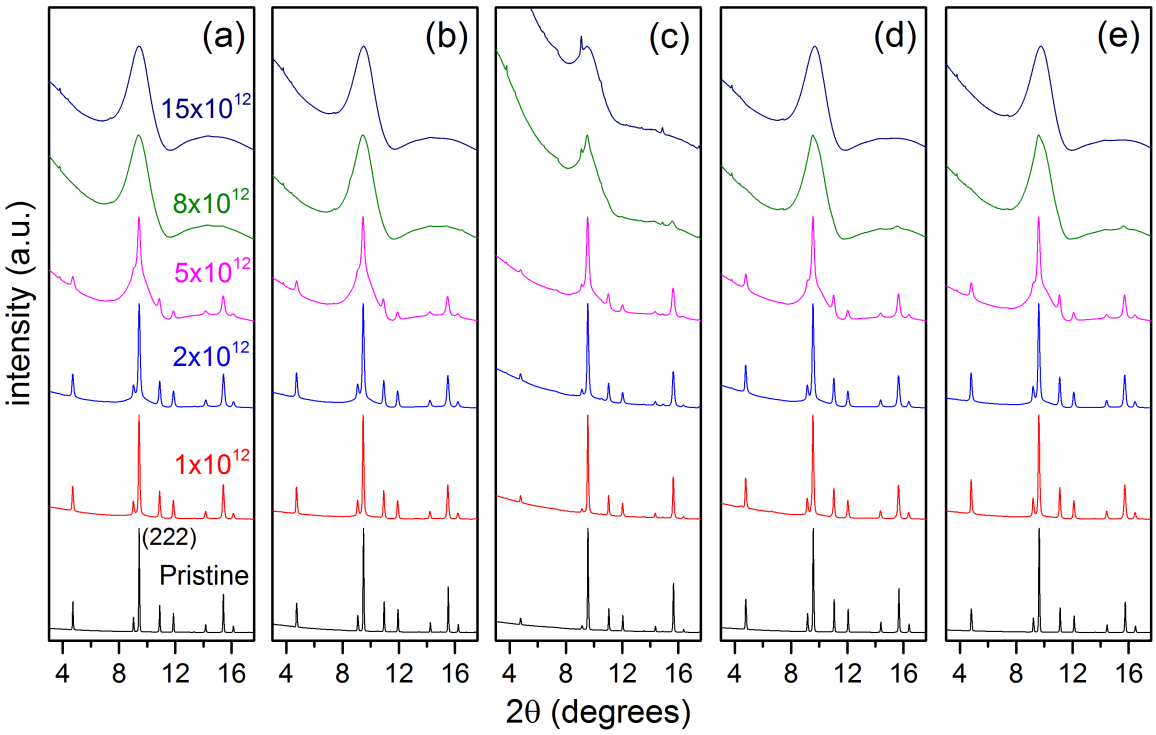

Figure 11: Synchrotron XRD patterns for (a) $Sm_2Ti_2O_7$, (b) $Gd_2Ti_2O_7$, (c) $Y_2Ti_2O_7$, (d) $Er_2Ti_2O_7$ and (e) $Yb_2Ti_2O_7$ before and after irradiation with 2.2 GeV Au ions to various ion fluences (all units are ions/cm^2).

All patterns were normalized to the same maximum intensity. The upturn in intensity at low 2θ in the high fluence samples is due the unscattered beam near the beamstop. This is much more prominent in high fluence patterns and all patterns from $Y_2Ti_2O_7$ due to the weaker scattering from the amorphous phase and yttrium relative to the lanthanides, respectively.

This is likely due to its significantly lower electron density, and thus smaller dE/dx, relative to the other compositions studied (see Table 3).

Concomitant with amorphization, the widths of the diffraction maxima also increase significantly with ion fluence (Figure 12). Peak broadening can be caused by either irradiation-induced grain fragmentation (size broadening) or by the production of defects in the crystalline fraction that distort the local structure (strain broadening) [105]. There is no clear relation between peak broadening and dE/dx or r_A/r_B, however, it is most prominent in $Sm_2Ti_2O_7$ (largest r_A/r_B) and least prominent in $Y_2Ti_2O_7$ (smallest dE/dx). There is also considerable unit cell expansion as indicated by a shift in the diffraction peaks to lower 2θ with increasing ion fluence (the (222) peak is shown in Figure 13). Interestingly, the first-order amorphous peak (centered at $2\theta \approx 9.5°$) becomes evident at a 2θ value that corresponds to the position of the (222) maximum in the pristine samples of $Sm_2Ti_2O_7$ and $Gd_2Ti_2O_7$ but at a higher 2θ in $Er_2Ti_2O_7$ and $Yb_2Ti_2O_7$ (Figure 13). The position of the amorphous bands directly relates to the mean interatomic spacing within the aperiodic array. An increase in scattering angle indicates that atoms are more tightly packed. This suggests that the relative density change associated with the crystalline-to-amorphous transition in $Er_2Ti_2O_7$ and $Yb_2Ti_2O_7$ could differ significantly from that in $Sm_2Ti_2O_7$ and $Gd_2Ti_2O_7$.

In order to obtain a quantitative understanding of the amorphization process, the XRD patterns were deconvoluted into amorphous and crystalline contributions. The amorphous phase fraction of all compositions initially increases linearly with ion fluence, then begins to saturate at higher fluences (illustrated for $Gd_2Ti_2O_7$ in Figure 14).

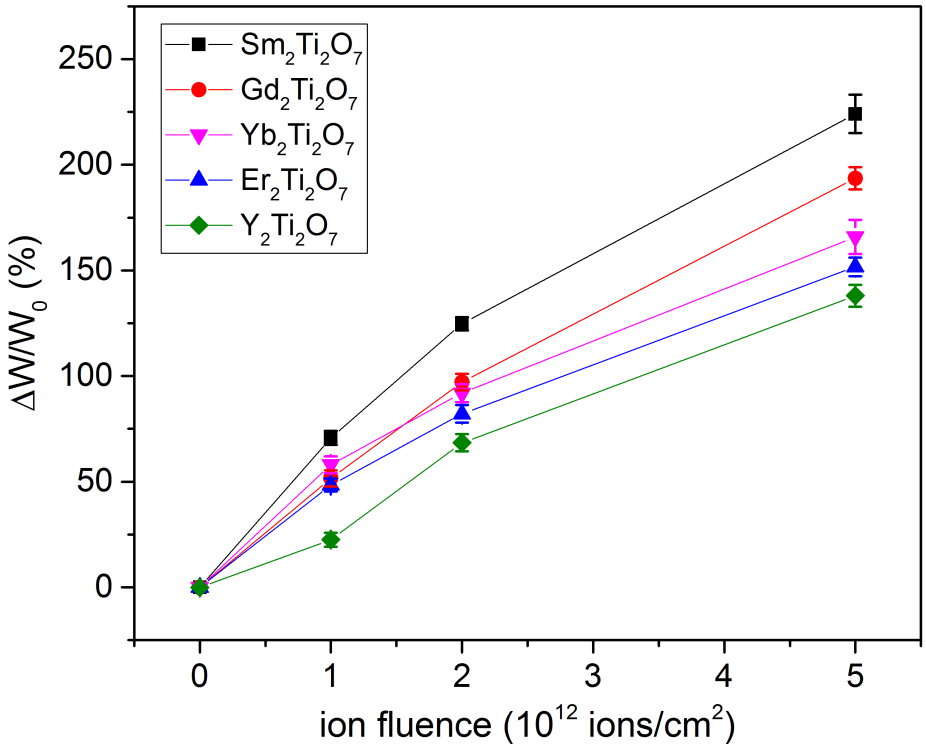

Figure 12: The relative change in width of the (222) Bragg peak increases as a function of ion fluence for all compositions studied.

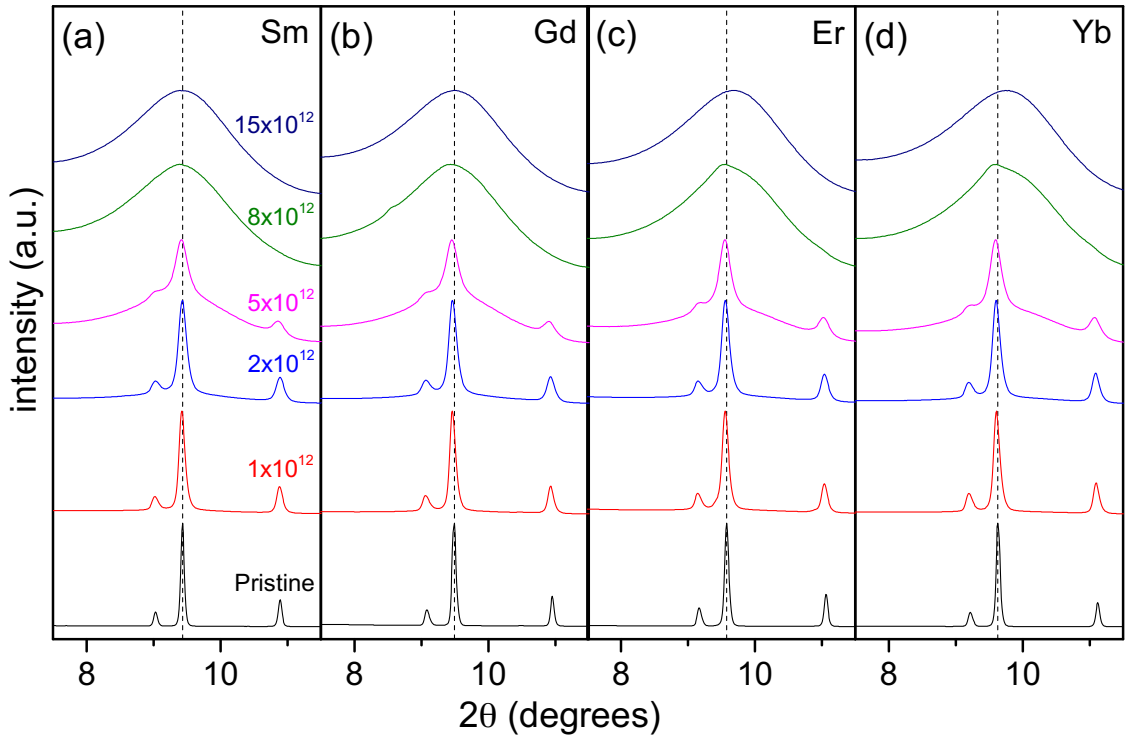

Figure 13: XRD patterns illustrating the development of the first-order amorphous scattering band for (a) $Sm_2Ti_2O_7$, (b) $Gd_2Ti_2O_7$, (c) $Er_2Ti_2O_7$, and (d) $Yb_2Ti_2O_7$.

The ion fluence has units of ions/cm^2. The vertical dashed lines denote the centroid of the (222) Bragg peak in the pristine samples. The amorphous phase develops at the same scattering angle as the pristine the (222) peak for A = Sm and Gd but at higher 2θ for A = Er and Yb.

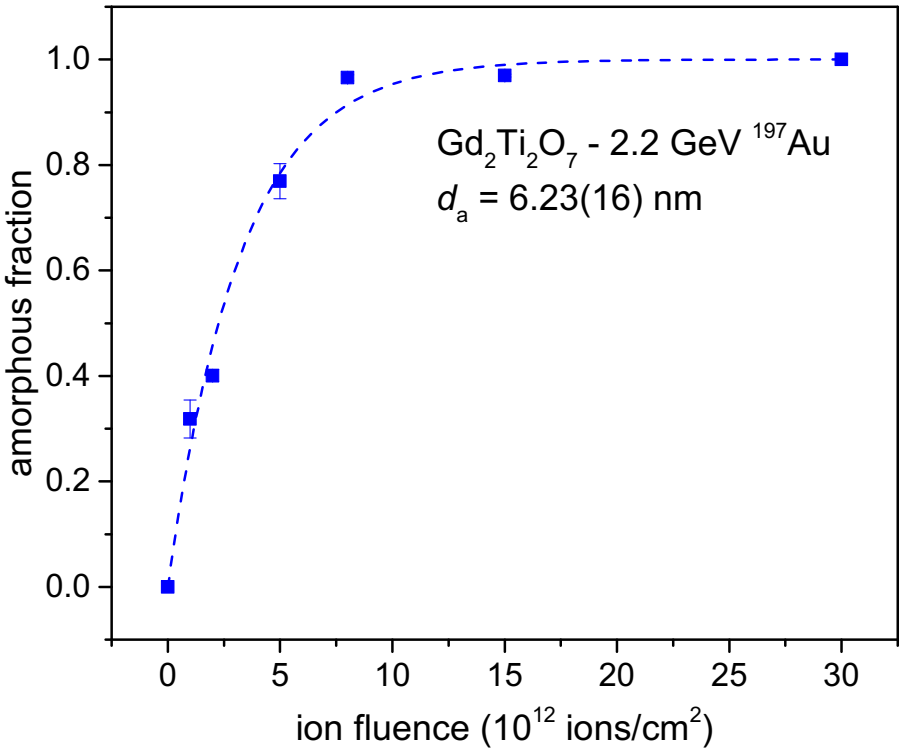

Figure 14: Amorphous phase fractions for $Gd_2Ti_2O_7$ as a function of ion fluence, extracted from peak deconvolution of XRD patterns.

The dashed line represents a fit of Eq. (23) to the data points. Assuming cylindrical symmetry, the amorphous track diameter extracted from this fitting is 6.2 $\pm$ 0.16 nm. Error bars are calculated from multiple deconvolutions at each given fluence and are smaller than the symbols at some points.

This model represents a damage production mechanism wherein each ion creates an amorphous track as it traverses the target material. With increasing fluence, tracks begin to overlap, eventually leading to complete amorphization of the pyrochlore sample. Alternative models have been proposed for swift heavy ion effects in pyrochlores to account for the overlap of complex track structures with core-shell morphologies [99]. However, the overall trend of the results presented here is in good agreement with a single impact model. Track diameters were determined using cross-sectional areas extracted from fitting Eq. (23) to the data assuming cylindrical ion track geometry:

$$\boldsymbol{\sigma = \pi \left(\frac{d}{2}\right)^2} \tag{23}$$

with *d* being the effective amorphous track diameter. Uncertainties were calculated by propagating the errors reported through the fitting procedure for multiple deconvolutions. The fitting results for all pyrochlore compositions are summarized in Table 3 and displayed in Figure 15.

The amorphous track diameter varies with the size of the A-site cation with an average diameter that linearly increases as a function of the ionic radius ratio r_A/r_B for A = Yb, Er, and Sm. Two compositions, $Y_2Ti_2O_7$ and $Gd_2Ti_2O_7$, however, fall significantly outside of this trend with appreciably smaller tracks in $Y_2Ti_2O_7$ and larger tracks in $Gd_2Ti_2O_7$. The deviation of $Y_2Ti_2O_7$ can be explained by its large difference in density, relative to the other compounds investigated, and the corresponding effect on the electronic d*E*/d*x* of the 2.2 GeV Au ions (Table 3). The calculated density is much lower for $Y_2Ti_2O_7$, which leads to a reduced d*E*/d*x* across the entire sample thickness as electronic stopping power is directly proportional to target electron density (Figure 10). This makes compositional analysis quite difficult as even small density variations from one composition to another can cause a relatively large change in amorphous track diameter.

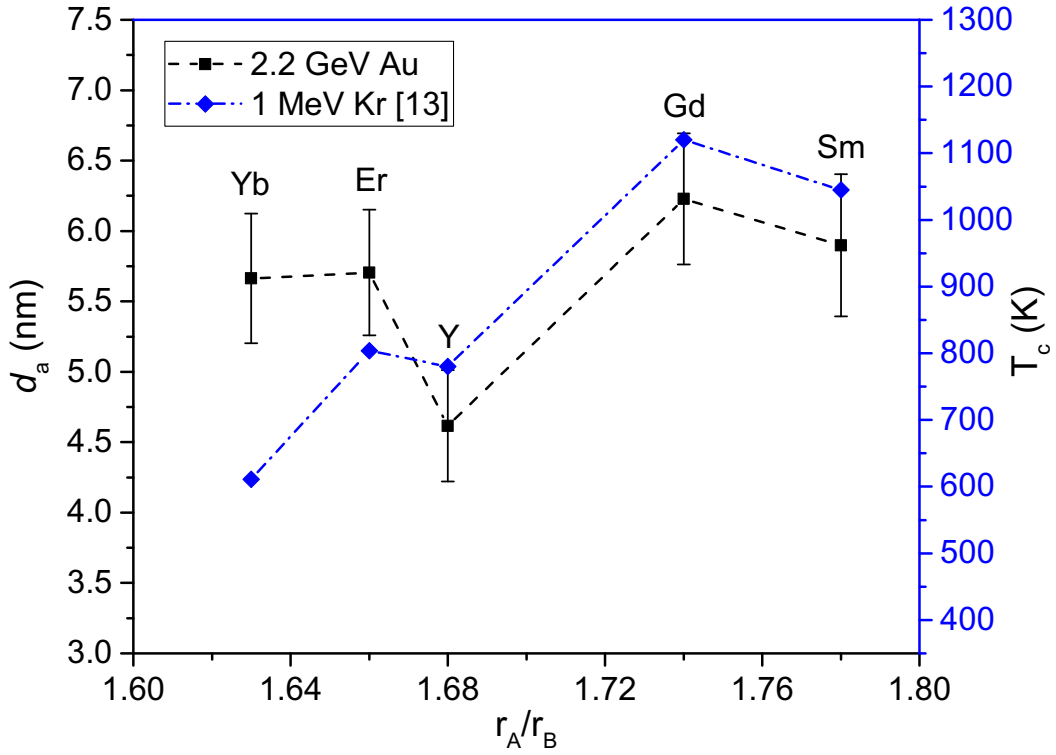

Figure 15: Amorphous track diameters measured from the peak-fitting procedure for each pyrochlore composition as a function of the cation ionic radii ratio (r_A/r_B) in the present study using 2.2 GeV Au ions (black squares, left axis) and critical amorphization temperatures for the same compounds determined by Lian *et. al.* using 1 MeV Kr ions (blue diamonds, right axis) [32].

Both studies show similar dependence of radiation tolerance on r_A/r_B despite differing energy loss mechanisms (purely electronic *vs.* mixed electronic/nuclear). $Gd_2Ti_2O_7$ was the most susceptible to amorphization of any composition in either study.

The effect of d*E*/d*x* on track size is generally a material-dependent, complex relationship [106, 107], but it has been previously shown for $Gd_2Ti_2O_7$ that the diameter of amorphous tracks monotonically increases with the electronic energy loss with approximately $d_a \propto (dE/dx)^2$ dependence (Figure 16) [48]. Assuming this relation holds for other titanate pyrochlores, it is reasonable to divide the amorphous track diameter extracted through XRD analysis by $(dE/dx)^2$ to effectively normalize the amorphous diameter by the energy loss (Figure 17). This normalization excludes the effects of d*E*/d*x* on track diameter allowing for direct comparison of the response of two compounds to the deposition of a specific amount of energy. The normalized amorphous track diameter increases monotonically within the r_A/r_B range studied but saturates at high r_A/r_B.

High-resolution transmission electron microscopy

High-resolution transmission electron microscopy (HRTEM) images confirm the existence of an amorphous phase within single ion tracks for all compositions studied, consistent with the single-impact model for amorphization. However, the ion track morphology differs significantly among the different compositions (Figure 18). Cross-sectional imaging shows that tracks in $Yb_2Ti_2O_7$ and $Er_2Ti_2O_7$ consist of an amorphous core, indicated by the aperiodic contrast in the center region of the track, surrounded by a crystalline shell with a structure different from the pyrochlore matrix (the dark ring observed in $Yb_2Ti_2O_7$ is likely caused by strain contrast). Previous experimental and computational investigations have shown that the track shell consists primarily of the disordered, defect-fluorite structure [52, 53, 108]. This is evident by the epitaxial relation between the defect-fluorite shell with the pyrochlore matrix. $Gd_2Ti_2O_7$ and $Sm_2Ti_2O_7$ display larger amorphous tracks with only a minimal disordered shell observed in $Gd_2Ti_2O_7$. In $Y_2Ti_2O_7$ (not shown) tracks are inhomogeneous consisting of amorphous and disordered regions distributed throughout the ion track cross section.

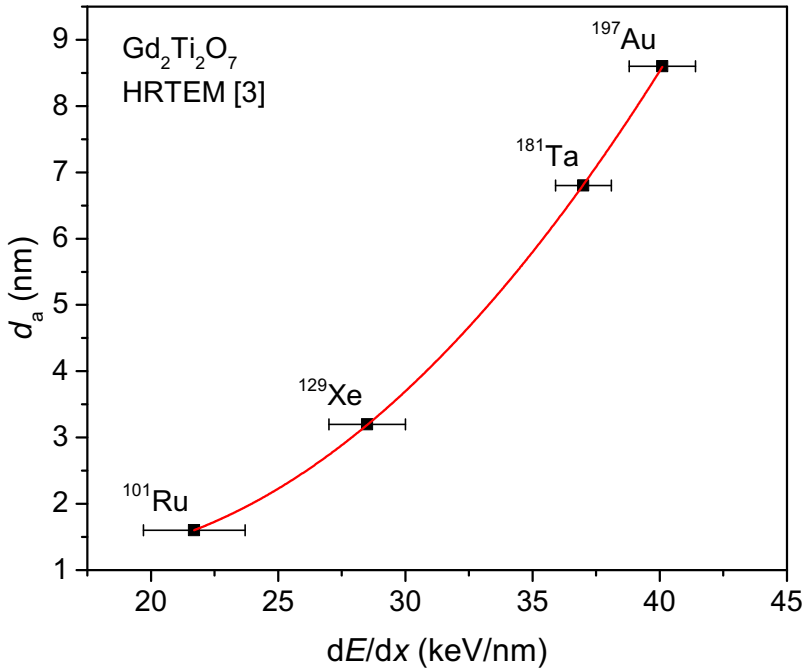

Figure 16: Amorphous track core diameters for $Gd_2Ti_2O_7$ irradiated with various projectile ions (11.1 MeV/u) measured by HRTEM.

The diameters show approximately $(dE/dx)^2$ dependence. The solid line is a guide to the eye. Figure reproduced from [48].

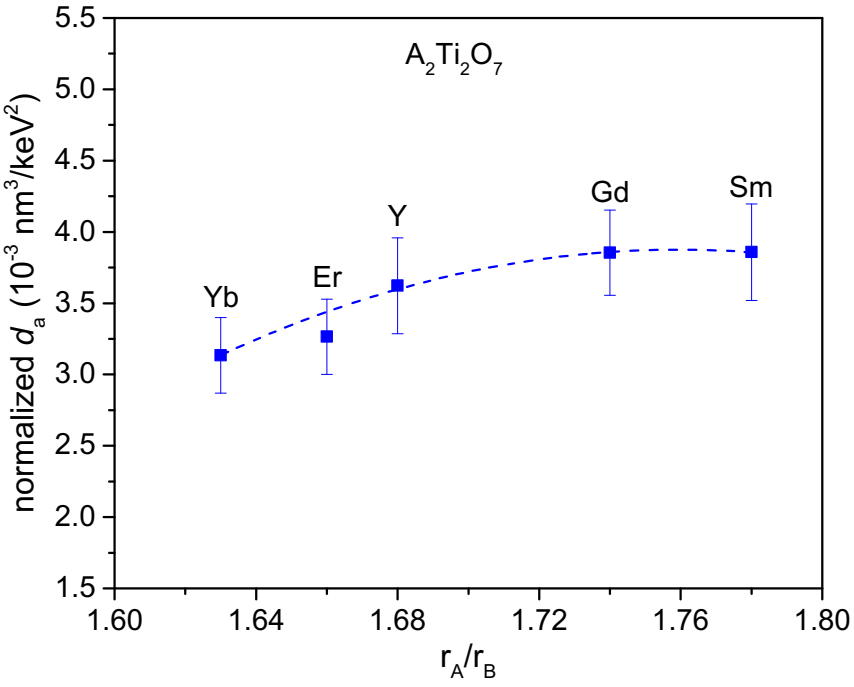

Figure 17: Amorphous track diameters normalized by $(dE/dx)^2$.

The nonlinear dependence on r_A/r_B is in agreement with disordering energy calculations in [42]. The dashed line is a guide to the eye. Error bars were calculated by propagating the variance in dE/dx through the sample with the errors from the peak fitting procedure.

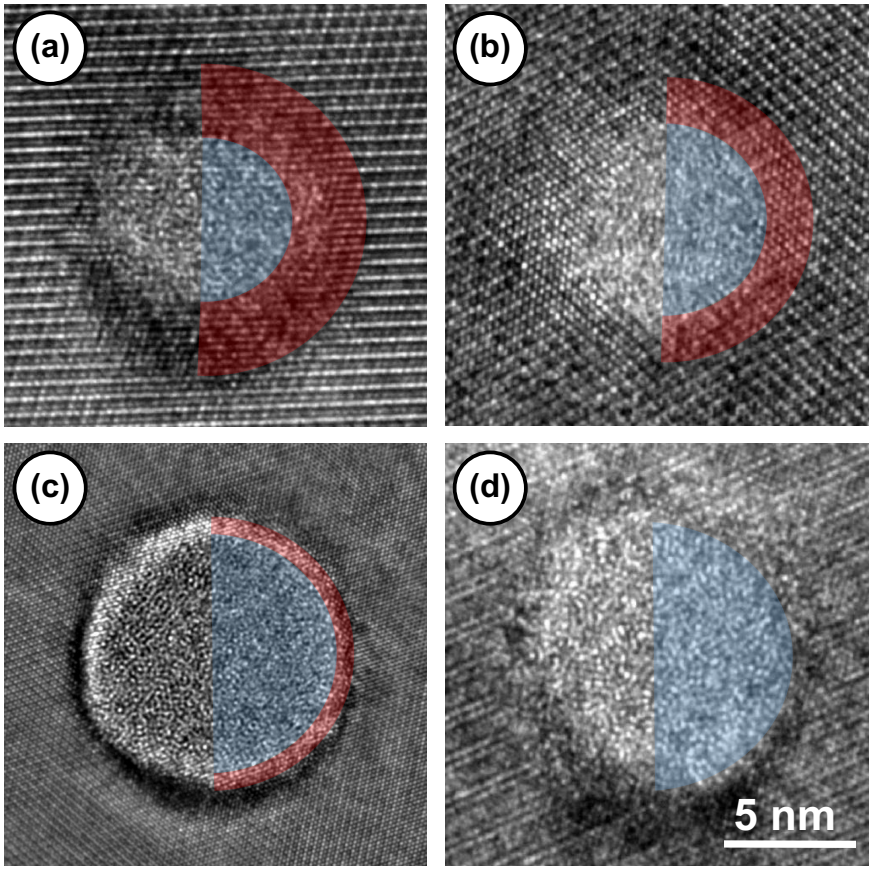

Figure 18: HRTEM images of single 2.2 GeV ion tracks in (a) $Yb_2Ti_2O_7$, (b) $Er_2Ti_2O_7$, (c) $Gd_2Ti_2O_7$*, and (d) $Sm_2Ti_2O_7$.

Ion tracks in $Yb_2Ti_2O_7$ and $Er_2Ti_2O_7$ consist of a small amorphous core surrounded by a large disordered shells while in $Gd_2Ti_2O_7$ the amorphous core is larger and the disordered shell smaller. Ion tracks in $Sm_2Ti_2O_7$ are completely amorphous. *$Gd_2Ti_2O_7$ was taken from [48]. The scale bar in (d) applies to all boxes.

Discussion

Susceptibility to Radiation-Induced Amorphization

Both XRD and HRTEM analysis show a consistent trend of an increasing amorphous volume produced within an ion track in the lanthanide pyrochlores as a function of r_A/r_B with the exception of $Sm_2Ti_2O_7$. XRD analysis reveals that $Gd_2Ti_2O_7$ has the largest amorphous track diameter (before d*E*/d*x* normalization) of any composition studied. The amorphous track diameters extracted through XRD analysis are smaller than those measured with HRTEM for all compositions studied. This is not surprising as differences in the structure factor for the amorphous and crystalline phase are neglected. An alternative method for analyzing the amorphous fraction using XRD, described in detail in [49], involves consideration of only the relative change in *crystalline* peak area before and after irradiation of the same sample. This approach however, assumes that *all* reduction in Bragg peak area can be attributed to amorphization, which is not fully accurate. Heating a sample will also result in reduced diffraction peak area in the absence of amorphization due to the influence of the Debye-Waller factor [109, 110]. In this case, atomic vibrations reduce the periodicity of even a perfect crystal which lowers the area of Bragg peaks. In addition, local deviations from the average structure (point defects, local distortions, *etc.*) can also lead to reduced Bragg peak area without amorphization [111, 112]. In general, many of the electrons excited during ion-solid interactions travel far beyond the central track region before relaxation, such that a defect-rich halo can be expected within otherwise undamaged pyrochlore matrix [46, 53]. These defects also reduce the area of Bragg peaks in the XRD data but are not directly associated with the ion track diameter. As a result, neither approach (described in [49] or peak deconvolution presented here) gives an absolute diameter value from XRD data that is directly comparable to HRTEM images, but the relative trend among the different compositions should be quite reliable. In fact, even HRTEM images may not fully

reflect the actual track size as MD simulations have shown that amorphous ion tracks can be heterogeneous along the ion trajectory [66]. Other contributions to TEM contrast, such as that from strain, can also be misinterpreted as amorphous material. Many tracks must be measured in order to get statistically meaningful information on the amorphous diameter, which is very difficult to obtain with HRTEM images. For this reason, HRTEM was used to characterize the damage morphology while XRD was used to study the *relative* changes in amorphous track diameter with composition.

Radiation-induced amorphization in the $A_2Ti_2O_7$ series has been previously studied with 1-MeV Kr^+ ions as a function of fluence and irradiation temperature [32]. Kr ions at this specific energy deposit their kinetic energy by electronic as well as nuclear energy loss. For our study, the most relevant information from this irradiation is the critical amorphization temperature, T_c, which is defined as the temperature above which a sample can no longer be amorphized under continuous irradiation due to dynamic defect annealing. Compositions with a higher T_c are considered to be more prone to radiation-induced amorphization. Although critical amorphization temperatures for low-energy ion irradiations and amorphous track diameters from swift heavy ion irradiations are not directly comparable, a similar r_A/r_B dependence was revealed for both parameters and energy-loss regimes (Figure 15). $Sm_2Ti_2O_7$ and $Y_2Ti_2O_7$ both gave rise to discontinuities in the trend of increasing amorphization susceptibility with r_A/r_B, with the unexpectedly high $Y_2Ti_2O_7$ resistance being much more pronounced. $Gd_2Ti_2O_7$ was the most susceptible to amorphization using both methods of analysis. The consistent behavior of both light and heavy ion irradiations with r_A/r_B can be explained by the disordering energetics of pyrochlore from first-principles calculations on the disordering energy for a range of pyrochlore compositions [42]. The disordering energy, $\Delta E_{disorder}$, was defined as the energy difference between the fully-ordered pyrochlore and fully-disordered defect-fluorite structure. The formation of the defect-fluorite structure is unfavorable for compositions with a high $\Delta E_{disorder}$, which

instead amorphize under irradiation. The disordering energy for titanate pyrochlores was shown to have a nonlinear dependence on A-site cation radius. $\Delta E_{disorder}$ initially increases with increasing r_A but shows a maximum at $Gd_2Ti_2O_7$ before decreasing for larger A-site cations. This is in agreement with the critical amorphization temperature trend observed in [32] and our XRD analysis, particularly when the amorphous track diameter is normalized by d*E*/d*x* (Figure 17). Although $Gd_2Ti_2O_7$ does not exhibit the largest normalized track diameter among the compounds investigated, this value is within error of that of $Sm_2Ti_2O_7$, and we do observe a saturation of the normalized diameter with larger r_A. This suggests that the same disordering-energy effect plays a key role in radiation resistance of pyrochlore compounds regardless of the mechanism of energy loss (*i.e.* electronic *vs.* nuclear).

The nonlinear trend observed in titanate pyrochlores is in contrast to previous experimental results from experiments in which the B-site cation was varied. Swift heavy ion studies on $Gd_2Zr_{2-x}Ti_xO_7$ pyrochlores have shown that these compounds become increasingly susceptible to amorphization as the titanium content at the B-site (*x*) is increased [48, 51, 53]. Bright-field TEM (BFTEM) measurements revealed that the *total* diameter of ion tracks (core + shell) resulting from irradiation with 1.47 GeV ^{129}Xe ions increases linearly as a function of r_A/r_B [53]. However, it was originally suggested that the *amorphous* diameter extracted through XRD analysis (applying the same peak deconvolution) showed a non-linear dependence with r_A/r_B similar to that shown in the present study. This non-linearity was mainly attributed to $Gd_2Zr_2O_7$ which has a singularity behavior with no measurable amorphization, and this composition was therefore discarded in later studies for the description of amorphous track diameters [48]. A linear dependence was postulated for the amorphous track core as a function of r_A/r_B, especially considering the fact that BFTEM images of *total* track diameter (*i.e.*, including the fluorite shell) showed a linear behavior. However, especially after normalization with $(dE/dx)^2$, the amorphous track diameter in the $Gd_2Zr_{2-x}Ti_xO_7$ still

appears to be curved with increasing r_A/r_B even when neglecting $Gd_2Zr_2O_7$ (see Figure 19). This trend when varying the B-site cation is thus in agreement with the data in the present study of changing the A-site cation. This shows that r_A/r_B is a major parameter determining the radiation resistance in pyrochlores, independently of how this parameter is changed.

A similar swift heavy ion study on orthorhombic A_2TiO_5 oxides (A = La, Nd, Sm, Gd) irradiated with 1.47 GeV Xe ions also exhibited a linear dependence of total track diameter on r_A/r_B as measured by BFTEM [31]. Although the uncertainty is relatively high, XRD analysis suggests that the amorphous core diameter initially increases with increasing r_A/r_B, but also saturates at high r_A/r_B, analogous to the behavior of titanate pyrochlores in this study. This is interesting because both systems show a linear increase in *total* track diameter (measured by BFTEM in [31] and [48]) but a curved dependence in *amorphous* track diameter despite having differing crystal structures. This perhaps demonstrates the generality of the importance of r_A/r_B on the radiation resistance and susceptibility to amorphization on complex ternary oxides.

Ion Track Morphology

The core-shell morphology is often assumed to form due to localized "melting" and rapid recrystallization/quenching following swift heavy ion penetration. MD thermal spike simulations have previously reproduced the core-shell morphology observed in $Gd_2Ti_2O_7$ [52]. The amorphous core is produced by the rapid quenching of a "molten" state while the shell forms due to epitaxial recrystallization at the molten/solid interface explaining why the disordered shell and surrounding pyrochlore matrix have matching crystallographic orientations. The energy density and cooling rate strongly influence the track morphology, as rapid cooling will lead to a predominantly amorphous track while slower cooling will enhance the formation of the disordered phase. This has been shown for tracks in

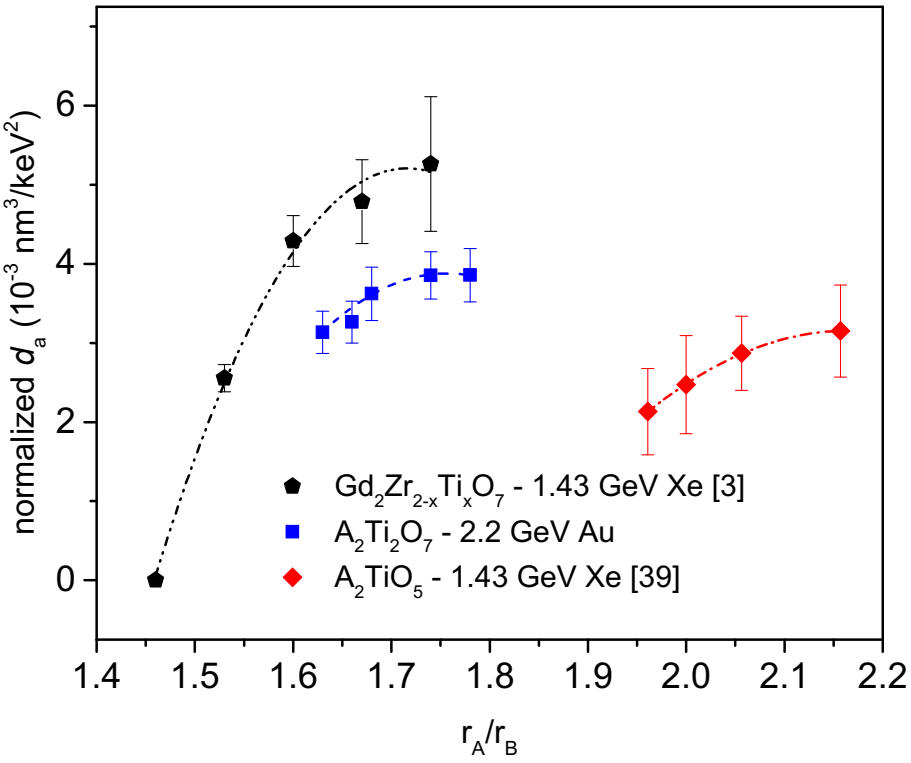

Figure 19: Comparison between amorphous track diameters (normalized by (d*E*/d*x*)^2) extracted through XRD analysis in isometric pyrochlore ($A_2Ti_2O_7$ (A = Yb, Er, Y, Gd, Sm)) in the present study and $Gd_2Zr_{2-x}Ti_xO_7$ in [48]) and orthorhombic A_2TiO_5 in [31].

Normalization was performed to account for dE/dx variations due to the different densities across the sample series, however, all studies also display a nonlinear dependence on r_A/r_B before normalization. Larger uncertainties in [48] and [31] are largely due to increased variance in d*E*/d*x* across the sample.

$Gd_2Ti_2O_7$, which exhibit a core-shell morphology that changes as a function of energy loss [48].

Tracks in $Yb_2Ti_2O_7$ and $Er_2Ti_2O_7$ induced by 2.2 GeV Au ions (Figure 18) display core-shell morphologies similar to those observed in the $Gd_2Zr_{2-x}Ti_xO_7$ solid solution series [48, 49, 53]. The same general trend is observed in the present study, as the amorphous core becomes larger and the disordered shell less pronounced with increasing r_A/r_B. Interestingly, $Sm_2Ti_2O_7$ shows no evidence of a disordered shell even though the energy-loss (Figure 10), density (Table 3), and the calculated disordering energy in [42] are less than that of $Gd_2Ti_2O_7$. This could indicate that the recrystallization rate is affected more strongly by r_A/r_B than energy deposition.

The strong core-shell morphology for A = Yb and Er and the predominantly amorphous tracks with little to no fluorite shell for A = Gd and Sm seem to have noticeable effects on the position of the 1st order amorphous band in the XRD patterns. The first amorphous peak develops at higher 2θ relative to the (222) Bragg peak in pristine $Yb_2Ti_2O_7$ and $Er_2Ti_2O_7$, but the two appear at nearly the same scattering angle for $Gd_2Ti_2O_7$ and $Sm_2Ti_2O_7$ (Figure 13). This suggests that the amorphous core is denser in tracks that are surrounded by a defect-fluorite shell. This could be caused by an under dense fluorite shell, relative to the initial pyrochlore phase, as volumetric expansion upon disordering would cause the track shell to exert a compressive force on the track core. An under dense shell has been confirmed experimentally for Gd_2TiZrO_7 irradiated with 120-MeV U ions, which displays a core-shell morphology by HRTEM [99]. More recently, high angle annular dark field imaging and molecular dynamics simulations have also shown that cation-cation spacing is increased in the defect fluorite shell relative to the bulk pyrochlore [65]. However, at high fluences in which the $Yb_2Ti_2O_7$ and $Er_2Ti_2O_7$ are completely amorphous, the 1st order amorphous band still appears at higher scattering angles relative to the pristine (222) peak. Therefore, it is also thought

that more efficient packing for compositions with similarly sized cations ($Yb_2Ti_2O_7$ and $Er_2Ti_2O_7$) must also contribute to a denser amorphous phase.

Similar to track sizes (Figure 19), the morphology of tracks in orthorhombic A_2TiO_5 compounds shows a consistent behavior with the titanate pyrochlore in this study. Consistent with the results of this study, cation ratios with a smaller r_A/r_B (Sm_2TiO_5) in [31] resulted in an amorphous core surrounded by a disordered, defect-fluorite shell while the composition with the largest r_A/r_B (La_2TiO_5) showed larger, completely amorphous tracks. This indicates that the recrystallization kinetics within ion tracks is strongly dependent on the chemical composition of the complex oxides, in particular, the cation ionic radius ratio r_A/r_B.

Conclusions

Polycrystalline samples of the $A_2Ti_2O_7$ composition with A=Yb, Er, Y, Gd, Sm were irradiated with 2.2 GeV ^{197}Au ions. This A-site substitution provides an A- to B-site cation ionic radius ratio ranging from 1.63 to 1.78. $Y_2Ti_2O_7$ showed much more amorphization resistance than the rare-earth containing samples due to the smaller electronic energy loss associated with its lower density. XRD analysis revealed that $Gd_2Ti_2O_7$ is the most readily amorphized composition among the titanate pyrochlores. Normalization of amorphous track diameters by the electronic energy loss shows an initial increase of amorphous track size with r_A/r_B that saturates for ionic radius ratios above $Gd_2Ti_2O_7$. This agrees with previous experiments using low-energy ions [32] and with first-principles calculations on disordering energy [42] suggesting that the same disordering energy operates in both the nuclear and electronic energy loss regime. HRTEM demonstrates that ion tracks in $Sm_2Ti_2O_7$ and $Er_2Ti_2O_7$ (smaller r_A/r_B) display a core-shell morphology (amorphous core surrounded by a defect-fluorite shell) while $Gd_2Ti_2O_7$ and $Sm_2Ti_2O_7$ (larger r_A/r_B) have a larger amorphous cores surrounded by minimal shells. r_A/r_B is clearly a dominating factor in predicting track

size and morphology which even extends to other compositionally related complex oxides. This is independent of whether the A- or B-site cation is altered.

CHAPTER II

PROBING DISORDER IN ISOMETRIC PYROCHLORE AND RELATED COMPLEX OXIDES

A version of this chapter was originally published by Jacob Shamblin, Mikhail Feygenson, Joerg Neuefeind, Cameron L. Tracy, Fuxiang Zhang, Dirk Bosbach, Haidong Zhou, Rodney C. Ewing, and Maik Lang in the journal *Nature Materials*:

Shamblin, J., *et al.* (2016). "Probing disorder in isometric pyrochlore and related complex oxides." Nature Materials **15**(5): 507-511.

This letter has been revised to consolidate the main text and supplementary materials that appeared separately in publication and to eliminate overlap with the previous chapters. J.S., C.L.T., R.C.E. and M.L. conceived and designed the experiments. M.L. and C.L.T. designed and coordinated the irradiation procedure. J.S., F.Z., S.F., D.B. and H.Z. synthesized the samples. J.S., M.F., C.L.T., J.N. and M.L. collected and interpreted the neutron scattering data. J.S., C.L.T., R.C.E. and M.L. prepared the manuscript.

Abstract

As shown in Chapter I, compounds with the isometric pyrochlore structure [1], $A_2B_2O_7$, can adopt a disordered, isometric fluorite-type structure, $(A,B)_4O_7$, under extreme conditions [16, 23, 25-27]. The energetics of this process are thought to govern the radiation response of fluorite-related materials. Despite the importance of the disordering process there exists only a limited understanding of the role of local ordering on the energy landscape and a compositions ability to incorporate the disordered phase. We have used neutron total scattering to show that disordered fluorite (induced intrinsically by composition/stoichiometry or at far-from-equilibrium conditions produced by high-energy radiation) consists of a local orthorhombic structural unit that is repeated by a pseudo-translational symmetry,

such that orthorhombic and isometric arrays coexist at different length-scales. We also show that inversion in isometric spinel occurs by a similar process. This insight provides a new basis for understanding order-to-disorder transformations important for applications such as plutonium immobilization[16], fast ion conduction[20], thermal barrier coatings[10, 113].

Experimental Methodology

Two ordered pyrochlore compositions ($Ho_2Ti_2O_7$, $Er_2Sn_2O_7$) and isometric spinel ($MgAl_2O_4$) were synthesized *via* conventional solid-state methods. Ordered $Nd_2Zr_2O_7$ was prepared by a wet chemical synthesis technique. Aqueous solutions of $ZrOCl_2 \cdot 8H_2O$ and $Nd(NO_3)_3 \cdot 6H_2O$ were prepared and mixed in stoichiometric ratios. Hydroxides were coprecipitated in 25% concentrated liquid ammonia (NH_4OH). This process is described in detail by Finkeldei *et. al.* [114]. Disordering was achieved in the pyrochlore compounds by varying the chemical composition during solid-state synthesis ($Ho_2Zr_2O_7$, $NiAl_2O_4$), altering the stoichiometry during wet chemical synthesis ($Nd_{0.94}Zr_{2.53}O_{6.47}$), and irradiation with 2.2 GeV ^{197}Au ions ($Er_2Sn_2O_7$), respectively.

The as-prepared $Er_2Sn_2O_7$ powder was pressed into four custom-made aluminum sample holders (indented circular area of 1 cm diameter and 75 μm depth) and irradiated to an ion fluence of 8×10^{12} ions/cm^2 with 2.2 GeV Au ions at the X0 beamline of the GSI Helmholtz Centre for Heavy Ion Research in Darmstadt, Germany. The sample mass per holder was calculated in a manner described on page 23. After irradiation, the ~100 mg powder was removed from the Al holders and inserted into quartz capillaries with an outer diameter of 2 mm and wall thickness of 0.01 mm.

Structural characterization was performed at the Nanoscale-Ordered Materials Diffractometer (NOMAD) at the Spallation Neutron Source at Oak Ridge National Laboratory. Approximately 100 mg of each sample was measured in 2 mm diameter quartz capillary cans for 90 minutes at room temperature. NOMAD

detectors were calibrated using scattering from diamond powder and standard Si powder was measured to obtain the instrument parameter file for the Rietveld refinements. The highest Q-resolution backscattering bank was used for the Rietveld refinements of the diffraction data. In order to obtain the structural factor S(Q), the scattering intensity was normalized to the scattering from a solid vanadium rod and background was subtracted using an identical, empty 2mm quartz capillary can measured for the same time as the powder samples. The PDF was calculated by the Fourier transform of $S(Q)$ with Q_{min} = 0.1 Å^{-1} and Q_{max} = 31.4 Å^{-1} (Eq. (15)). The PDFs were characterized with small-box refinement (discussed below).

Rietveld refinements of diffraction data were completed using FullProf [91]. All PDF refinements were carried out using the PDFgui software[95]. A total of five refinement parameters were used when refining the pair distribution function (PDF) using the isometric, disordered fluorite model (F*m*-3*m*). These included the unit cell parameter (a = b = c), the scale factor, the correlated motion parameter (PDF refinements), and one atomic displacement parameter (ADP) (u11 = u22 = u33) for each crystallographic site. Because both cations share crystallographically equivalent sites, a single ADP was used for both the A- and B-site cations while a second ADP was used for the oxygen anion sites. In this model, A- and B-site cations equally share full occupancy of 4*a* sites (0,0,0) while oxygen anions occupy 7/8$^{\text{th}}$ of the 8*c* sites (0.25, 0.25, 0.25). Due to the isometric structure and fixed Wyckoff sites, no more than 5 parameters can be refined.

The number of PDF refinement parameters was increased to 12 for the pyrochlore structure ($Ho_2Ti_2O_7$, *Fd*-3*m*): unit cell parameter (a = b = c), scale factor, correlated motion parameter (PDF refinements), x-position for 48*f* sites, and 8 ADPs. The eight ADPs include two each for 16*c* and 16*d* sites (u11 = u22 = u33 & u12 = u13 = u23), three for 48*f* sites (u11 ≠ u22 = u33 & u23), and one for 8*b* sites (u11 = u22 = u33).

Refinement of the PDF using the orthorhombic, weberite-type model (C*cmm*) required a total of 28 restraints. These included 3 unit cell parameters (a ≠ b ≠ c), scale factor, correlated motion parameter (PDF refinements), 8 atomic position parameters, and 15 ADPs. The 8 position parameters are comprised of the *x*- and *y*-position for 8*g* sites, the *x*-, *y*-, and *z*-positions for 16*h* sites, and the *x*-position for all three 4*c* sites. For simplicity, each Wyckoff site was given its own set of three ADPs (u11 ≠ u22 ≠ u33). In other words, all 4*a* sites had their own u11, u22, and u33; all 4*b* sites then had a different u11, u22, u33 etc. The three 4*c* sites were given the same set of ADPs. All refinements resulted in no highly correlated constraints.

A total of 23 refinement parameters were used for PDF refinement of the tetragonal spinel ($P4_122$) phase in $NiAl_2O_4$. These included two unit cell parameters (a = b ≠ c), the scale factor, the correlated motion parameter (PDF refinements), the "inversion" parameter, nine position parameters, and nine ADPs. The inversion parameter, i, was defined as the fraction of 4*a* sites occupied by nickel (or the fraction of 4*c* sites occupied by Al) and was used to calculate the site occupancies (4*b* sites were fully occupied by Al). The position parameters included x = y for 4*c* sites, y for 4*a* and 4*b* sites, and x, y, & z for both 8*d* (oxygen) sites. Each cation site had its own ADP ($u_{11} = u_{22} = u_{33}$) while each 8*d* site had three ADPs ($u_{11} \neq u_{22} \neq u_{33}$). The above procedure was also used for $MgAl_2O_4$.

Only 8 refinement parameters could be used for refining the isometric spinel phase for $NiAl_2O_4$ (*Fd*-3*m*) including the unit cell parameter (a = b = c), the scale factor, the correlated motion parameter (PDF refinements), the inversion parameter, 32*e* (oxygen) position parameter (x = y = z), and three ADPs. Each Wyckoff site (8*a*, 16*d*, 32*e*) was given its own ADP ($u_{11} = u_{22} = u_{33}$). The inversion parameter, i, denoted the fraction of 8*a* sites occupied by Al (the fraction occupied by Ni was therefore 1 – i). The fraction of 16*d* sites occupied by Ni and Al was i/2 and 1 – i/2 respectively. The above procedure was also used for $MgAl_2O_4$.

Results/Discussion

Pyrochlores with heavy A-site cations, such as Ho, offer a unique opportunity to study the order/disorder transformation as disorder can be induced through cation substitution on the B-site. Neutron diffraction is ideal to characterize the average structure as it is sensitive to the oxygen sublattice while the pair distribution function (PDF) from neutron total scattering probes the local structure. Structural refinement of fully ordered $Ho_2Ti_2O_7$ shows that the local (assessed through PDF, Figure 20a) and average (Figure 21) structure are both in excellent agreement with the isometric pyrochlore structure (*Fd*-3*m*, Figure 20d). A-site cations (16*d*) are coordinated with six 48*f* oxygen atoms and two 8*b* oxygen atoms. B-site cations (16*c*) are coordinated with six 48*f* oxygen atoms and two ordered 8*a* vacancies. $Ho_2Ti_2O_7$ can be intrinsically disordered to the fluorite-type average structure by substituting the B-site with larger Zr atoms to form $Ho_2Zr_2O_7$, which has an r_A/r_B below the stability field of the pyrochlore structure[1]. Evidence of a modulated structure is apparent in neutron diffraction as broad diffuse peaks orders of magnitude lower in intensity than Bragg peaks[83]. These diffuse peaks, which were absent in $Ho_2Ti_2O_7$, must be discarded as background during the Rietveld refinements[38]. The disordered fluorite model fits well to the diffraction data of $Ho_2Zr_2O_7$ when diffuse contributions are subtracted with the background (Figure 22). However, this treatment of the background provides no quantitative information regarding the origin of the diffuse scattering; hence, PDF analysis is necessary to study the local crystal structure. Disorder is readily apparent in the PDF as many distinct peaks in the $Ho_2Ti_2O_7$ data merge into single, broader peaks for $Ho_2Zr_2O_7$ (Figure 20b). The local structure was initially refined with the average fluorite-type structural model (*Fm*-3*m*, Figure 20e) in which A- and B-site cations randomly occupy 4*a* sites and anions occupy $7/8^{th}$ of 8*c* sites. The fit results are summarized in Table 4.

Figure 20: Neutron PDFs and structural models for ordered ($Ho_2Ti_2O_7$) and disordered ($Ho_2Zr_2O_7$) pyrochlore.

a) Small-box refinement of the neutron PDF, G(r), as a function of distance, r, using the ordered $Ho_2Ti_2O_7$ pyrochlore structure shown in d). Open circles represent experimental data, the solid red line represents the fit obtained through refinement, and the solid green line represents the difference between the experimental data and the refinement. The average and local structures agree well. It should be noted that Ho and Ti have contrasting neutron scattering lengths (7.17 and −3.438 fm respectively) resulting in positive peaks for Ho–O correlations and negative peaks for Ti–O correlations. b) Small-box refinement of the neutron PDF for $Ho_2Zr_2O_7$ with the disordered fluorite structure shown in e). Although the disordered fluorite model characterizes the average structure in $Ho_2Zr_2O_7$ well, the PDF shows a poor fit locally, particularly below 10 Å, as noted by the difference curve. c) Small-box refinement of the neutron PDF for $Ho_2Zr_2O_7$ with the orthorhombic weberite-type structure shown in f). The local structure is captured very well. The refinement ranges of a)–c) was 1–15 Å. d)–f), Structural relations between the pyrochlore (d), disordered fluorite (e) and weberite-type (f) arrangements. Both the pyrochlore and weberite-type structures are supercells of disordered fluorite with unit cell parameters of $a_{PC} = a_{WB} = 2a_{DF}$ and $b_{WB} \approx c_{WB} \approx a_{DF}\sqrt{2}$ (the subscripts refer to pyrochlore, weberite-type and disordered fluorite respectively). Red spheres represent oxygen sites that are fully occupied in the pyrochlore and weberite-type structures but 7/8ths occupied in disordered fluorite. Black and cyan spheres represent A- (CN = 8) and B-site (CN = 6) cations, respectively. Blue spheres designate cation site mixing (CN = 7).

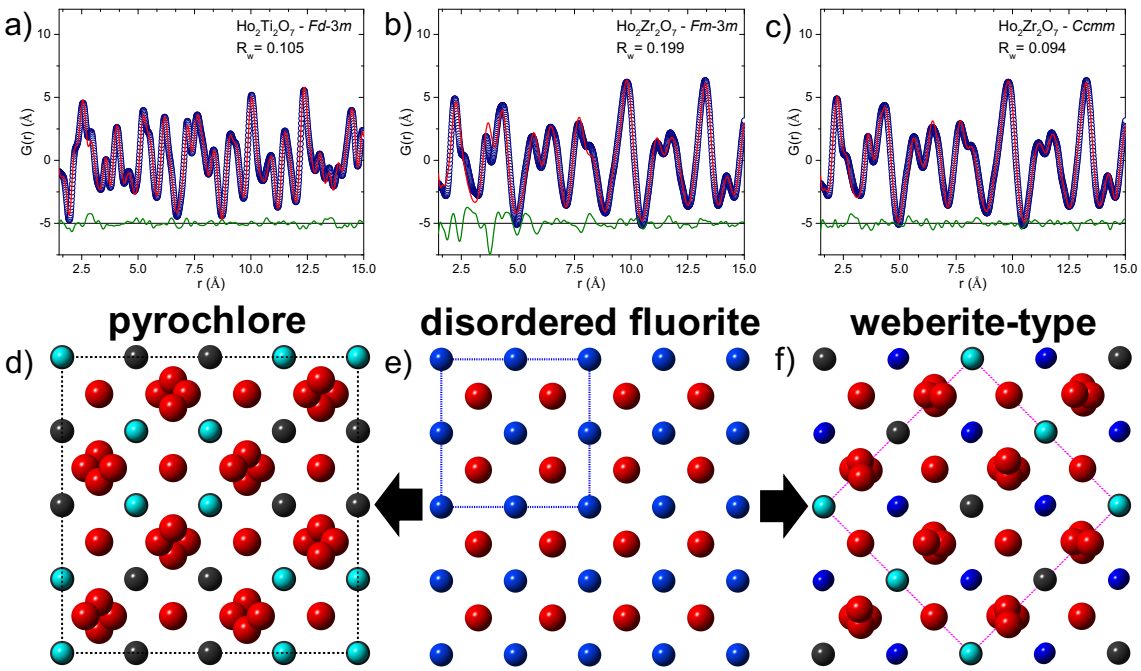

Figure 20. Continued

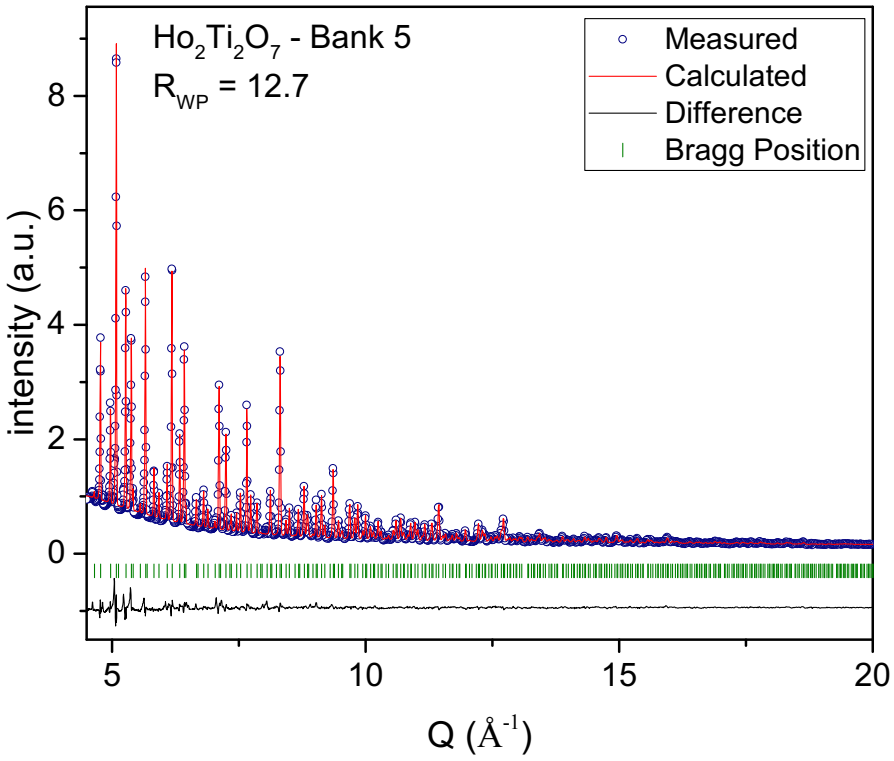

Figure 21: Neutron diffraction pattern of $Ho_2Ti_2O_7$.

The measured diffraction pattern (open circles) can be accurately reproduced by the calculated pattern (solid red line) of the pyrochlore structure (Fd-3m). Green vertical ticks denote Bragg peak locations while the solid black line represents the difference between the measured and calculated patterns.

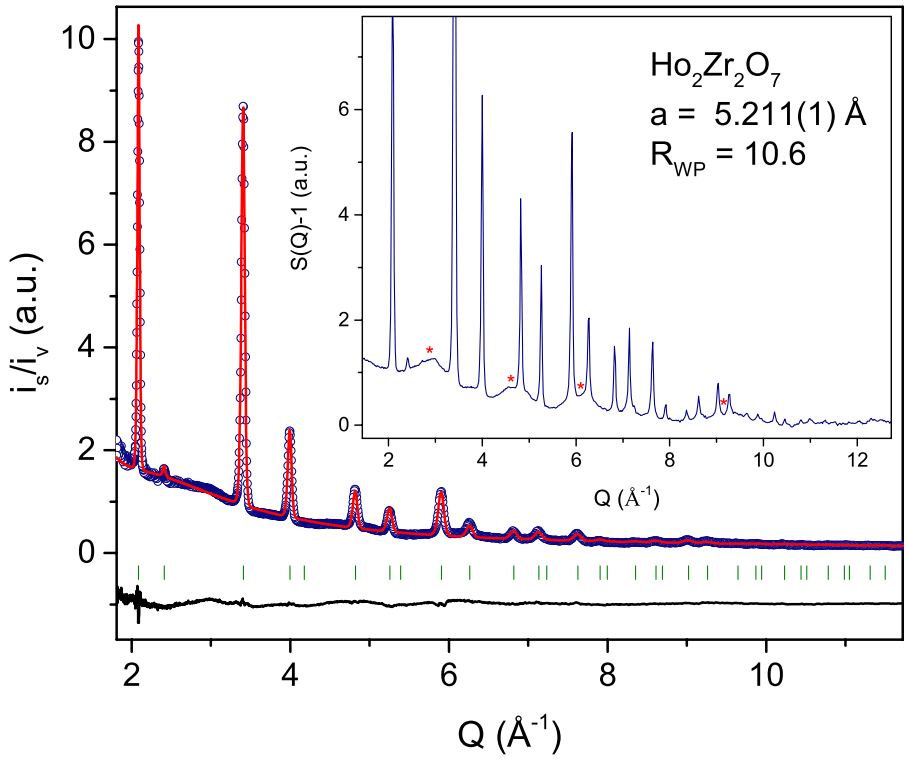

Figure 22: **Neutron powder diffraction pattern (open circles) of $Ho_2Zr_2O_7$ refined with the isometric disordered fluorite structure (solid red line).**

The black line represents the difference between the experimental and calculated pattern. Vertical ticks denote refined Bragg peak positions. The differing local structure results in diffuse peaks shown in the total scattering structure function (inset, designated with red asterisks) that must be refined with the background or ignored if a disordered fluorite structure is assumed.

Table 4: Summary of Rietveld and PDF small box refinements for pyrochlores disordered through B-site substitution ($Ho_2Ti_2O_7$ → $Ho_2Zr_2O_7$), partial A-site substitution ($Nd_2Zr_2O_7$ → $Nd_{0.94}Zr_{2.53}O_{6.47}$), and irradiation with 2.2 GeV ^{197}Au ions ($Er_2Sn_2O_7$).

Neutron Diffraction (Disordered Fluorite Structure Model)

Composition	Disordering Method	***a* (Å)**	R_{WP}
$Ho_2Zr_2O_7$	Intrinsic (Chemical Composition)	5.211(1)	10.6
$Nd_{0.94}Zr_{2.53}O_{6.47}$	Intrinsic (Non-Stoichiometry)	5.2216(3)	11.1
$Er_2Sn_2O_7$	Extrinsic (Irradiation)	5.2048(9)	11.3

Neutron PDF (Disordered Fluorite Structure Model)

Composition	Disordering Method	*r*-range:	**1.5 - 15 Å**	**15 - 30 Å**	**1.5 - 25 Å**
$Ho_2Zr_2O_7$	Intrinsic (Chemical Composition)	***a* (Å)**	5.217(1)	5.2129(6)	5.2151(6)
		R_W	0.199	0.121	0.168
$Nd_{0.94}Zr_{2.53}O_{6.47}$	Intrinsic (Non-Stoichiometry)	***a* (Å)**	5.227(1)	5.2239(5)	5.2247(5)
		R_W	0.161	0.088	0.132
$Er_2Sn_2O_7$	Extrinsic (Irradiation)	***a* (Å)**	5.202(3)	5.199(1)	5.200(1)
		R_W	0.241	0.137	0.210

Table 4. Continued

Composition	Disordering Method	*r*-range:	**1.5 - 15 Å**	**15 - 30 Å**	**1.5 - 25 Å**
$Ho_2Zr_2O_7$	Intrinsic	***a* (Å)**	10.56(2)	10.47(1)	10.51(1)
	(Chemical				
	Composition)	***b* (Å)**	7.38(1)	7.408(6)	7.366(9)
		***c* (Å)**	7.31(1)	7.321(8)	7.336(9)
		R_W	0.094	0.108	0.125
$Nd_{0.94}Zr_{2.53}O_{6.47}$	Intrinsic	***a* (Å)**	10.53(2)	10.48(2)	10.49(2)
	(Non-Stoichiometry)	***b* (Å)**	7.36(2)	7.39(1)	7.39(1)
		***c* (Å)**	7.37(1)	7.37(1)	7.358(9)
		R_W	0.076	0.061	0.090
$Er_2Sn_2O_7$	Extrinsic	***a* (Å)**	10.52(5)	10.50(4)	10.44(3)
	(Irradiation)	***b* (Å)**	7.37(3)	7.38(1)	7.40(2)
		***c* (Å)**	7.26(3)	7.29(1)	7.30(1)
		R_W		0.067	0.115

As shown by the substantial deviations from the zero baseline of the difference curve, there are significant mismatches in peak positions/intensities, specifically below 10 Å (about two unit cells), despite a satisfactory fit over longer length-scales (Table 4). There is also a shoulder at r = 2.6 Å that is not captured in the simulated PDF. The ordered pyrochlore structure was also fit to the experimental data and similarly fails to reproduce the PDF in largely the same areas as the disordered fluorite model (Figure 23). As shown in Figure 20c, the quality of the fit using the orthorhombic weberite-type model (*Ccmm*, Figure 20f) is significantly improved as compared with the fluorite-type model. The goodness-of-fit parameter (R_w) is reduced from 0.199 to 0.094 and the entire r-range is modeled accurately. Such a local structure has been proposed for fluorite-type Yb_3TaO_7 [115], which has a stoichiometry prone to long-range weberite-type ordering [116]. The present PDF data show that this specific local order is exhibited by a broader class of disordered fluorite-derivative oxides, for compositions which weberite-like ordering has not been previously observed over any length-scale.

The weberite-type arrangement maintains a fluorite-derivative superstructure similar to pyrochlore (see arrows in Figure 20); however, the symmetry is reduced. Cations occupy 4a, 4b, and 8g sites, which are in octahedral (6-fold), distorted cubic (8-fold), and distorted mono-capped octahedral (7-fold) coordination, respectively (Figure 24). Anions occupy 16h and three 4c sites. There remains an ordered vacancy, as in the pyrochlore structure, but it is now located at a fourth 4c site (Figure 25). Ho and Zr have similar neutron scattering lengths making it difficult to distinguish which cation resides on which site. However, many bond lengths become unphysical when Zr is located on 4*b* sites. The weberite-type structure is formed from distortions of alternating layers in the pyrochlore structure as both cations become 7-coordinated within these layers (Figure 24). Zr and Ho therefore likely occupy octahedral (4*a*) and distorted cubic (4*b*) sites, respectively (analogous to the pyrochlore orientation), and share occupancy of the mono-capped octahedral layers (Figure 25).

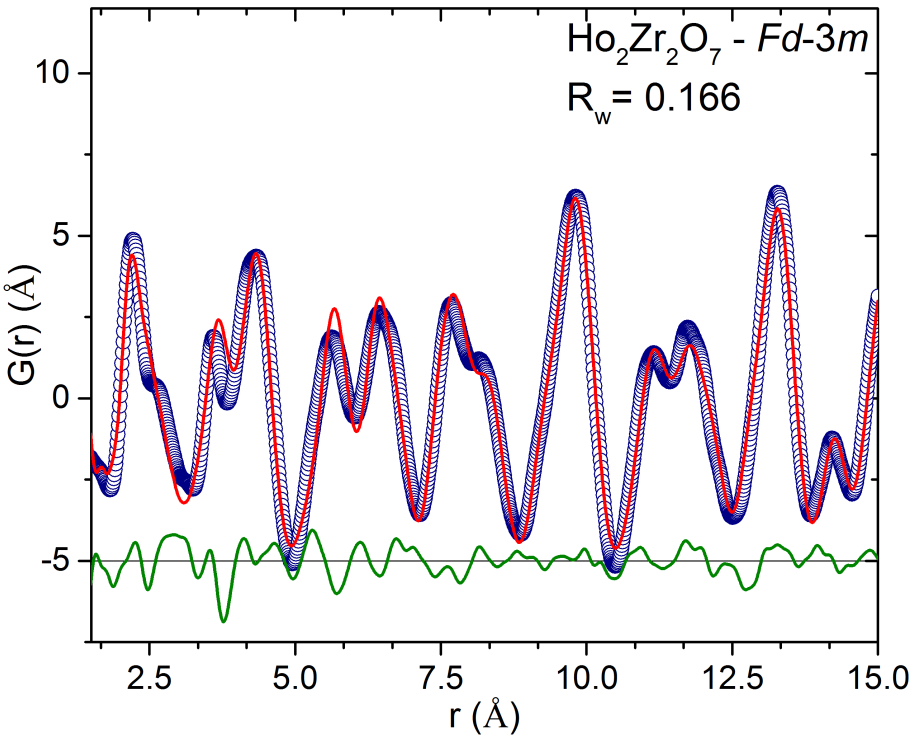

Figure 23: Experimental PDF (open circles) of $Ho_2Zr_2O_7$ fit with the ordered pyrochlore model (solid red line) from 1.5 – 15 Å.

The green line represents the difference between the measured and calculated PDFs. The RW value is improved from that of the disordered fluorite model but still fails to accurately reproduce the experimental data. The data was also refined with a disordered pyrochlore model in which A- and B-site cations were allowed to exchange sites and 48f oxygens were allowed to partially occupy 8a vacancies while retaining Fd-3m symmetry. This slightly improved the fit (RW = 0.161), however atomic displacement parameters (ADPs) became negative and highly correlated.

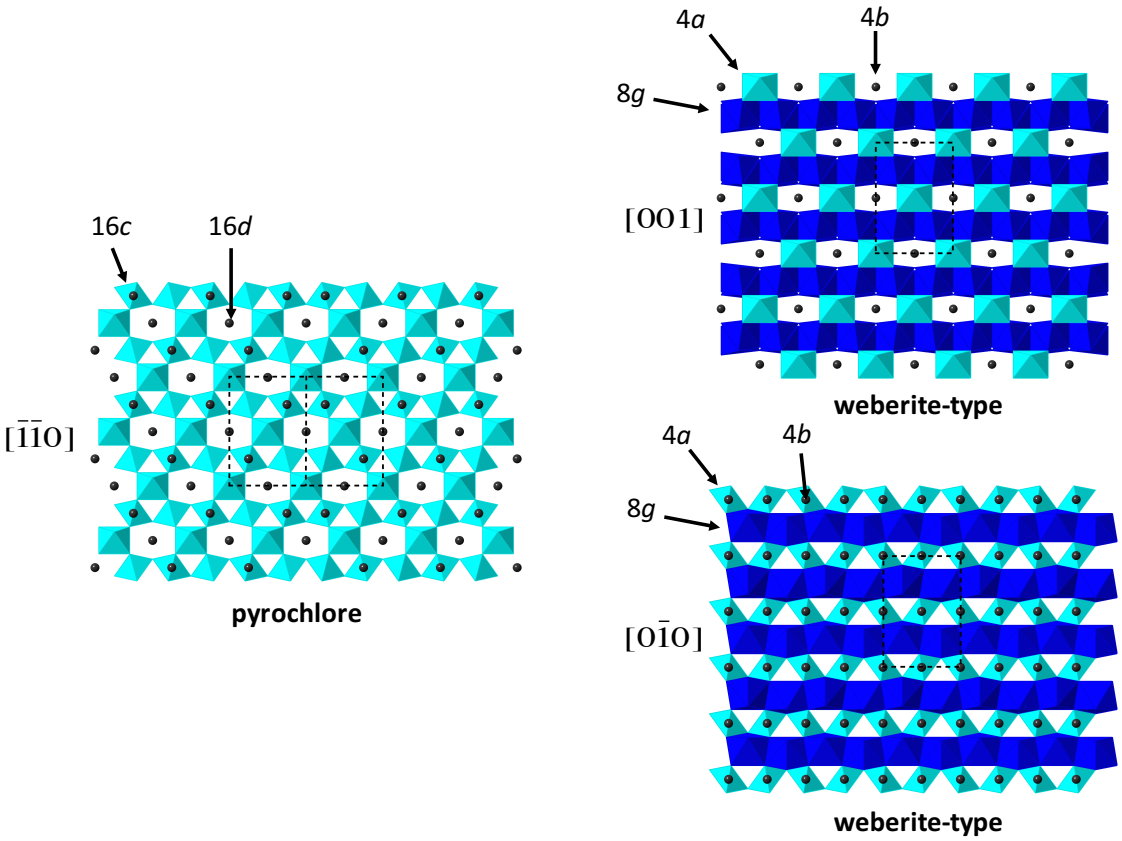

Figure 24: Relation between the pyrochlore and weberite-type structures.

All shown polyhedra in the pyrochlore structure are octahedra (16c) while black atoms are in distorted cubic coordination (16d). Cation sites in alternating layers in the pyrochlore structure disorder into a single crystallographic site (8g) in the weberite-type structure which is 7-coordinated with oxygen anions. Local 4a and 4b polyhedra in the weberite-type are analogous to the original pyrochlore structure (16c and 16d respectively). The dotted blank lines delineate the unit cells.

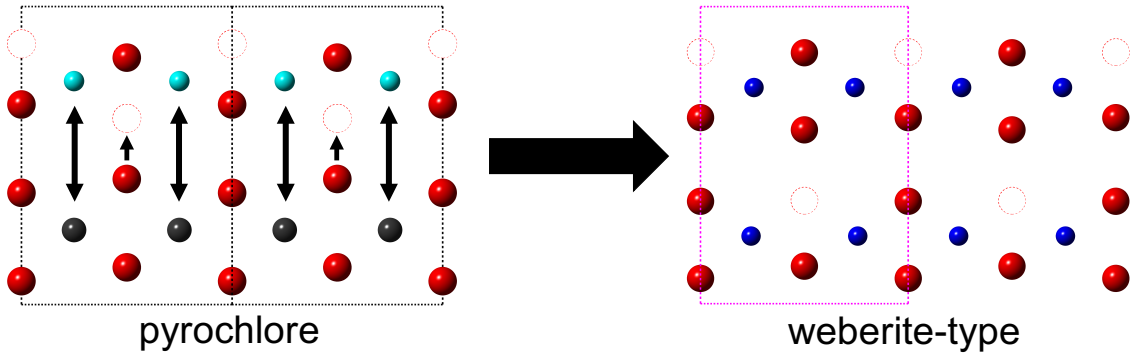

Figure 25: Oxygen vacancy ordering in the pyrochlore and weberite-type structure-types.

The pyrochlore unit cell consists of layers, containing both cations and anions, stacked along ⟨110⟩, such that they coincide with the [440] planes. Layers containing 16c, 16d, and 48f sites alternate with those containing 16c, 16d, 48f, and 8b sites along with vacant 8a sites. One of the latter layers is shown (left), viewed in [110]. Oxygen atoms and vacancies are shown as red and hollow spheres respectively. Black and cyan spheres in the pyrochlore structure represent A- (16d) and B-site (16c) cations respectively. Oxygen vacancies are localized around the B-site cations (6-coordinated) in the pyrochlore structure. Upon disordering, 48f oxygens occupy alternating rows of 8a vacancies in this plane accompanied by cation site exchange (shown as blue spheres in the weberite-type structure which correspond to the blue polyhedra in Figure 24). Collective atomic displacements that accompany the disorder transformation are indicated by the black arrows. The weberite-type plane (right) is viewed in the $[00\bar{1}]$ direction. The unit cells of both structure-types are shown for clarity (dashed lines). The outermost rows of oxygens/vacancies are not contained within the pyrochlore unit cell.

Total site multiplicity is reduced from 96 to 48 (compared with 12 in fluorite) such that the weberite-type structure can be considered a disordered derivative of the pyrochlore structure. This is in agreement with RMC[36] and X-ray absorption [38] experiments showing that while disorder is accompanied by an increase in B-site CN and a decrease in A-site CN, the two are not equivalent as would be the case with disordered fluorite local ordering, having a CN of 7. Redox effects in disordered titanate pyrochlores could further alter local coordination as previous X-ray absorption experiments suggest that the titanium CN reduces (at least partially) from 6 to 5 [37, 117].

While $Ho_2Ti_2O_7$ can be described as pyrochlore in terms of both local and average structure, disordered $Ho_2Zr_2O_7$ shows distinct regimes over different length scales: the average structure is consistent with isometric disordered fluorite while the local structure is weberite-type. This indicates that the average structure must be assembled by aperiodic, three-dimensional modulation of local structural units, inevitably forming a regime where the weberite-type structure no longer applies. While the PDF can be accurately modeled with as weberite-type from 1.5 – 15 Å, the intensity and position of the peaks below 5 Å are no longer reproducible if the fit range is expanded to 1.5 – 25 Å (see asterisks in Figure 26). The difference curve more closely resembles that of the disordered fluorite model (Figure 26) suggesting that the weberite-type structure is only valid for one to two unit cell repeats. Thus, the present data clearly show that disordering of pyrochlore oxides is complex, involving two distinct mechanisms on different length-scales: (1) the ordered local pyrochlore structure transforms into orthorhombic weberite-type units, and (2) aperiodic modulation of these local units yields an average isometric disordered fluorite structure.

Ordered pyrochlores were also disordered by irradiation with high-energy heavy ions ($Er_2Sn_2O_7$) and modification of the $A_2B_2O_7$ stoichiometry ($Nd_{0.94}Zr_{2.53}O_{6.47}$), such that the A-site is partially occupied by B-site cations (Figure 27).

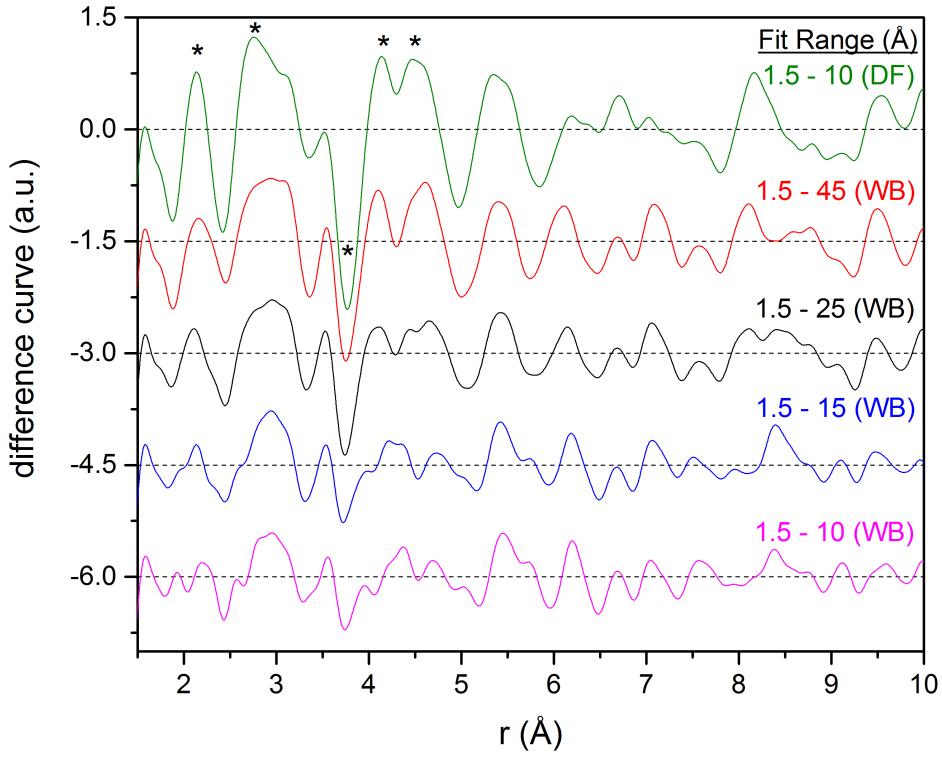

Figure 26: Difference curves (measured PDF – calculated PDF) for $Ho_2Zr_2O_7$ refined with the weberite-type structure (denoted as WB) at various fit ranges compared with that of the disordered fluorite structure (denoted as DF), refined from 1.5 – 10 Å.

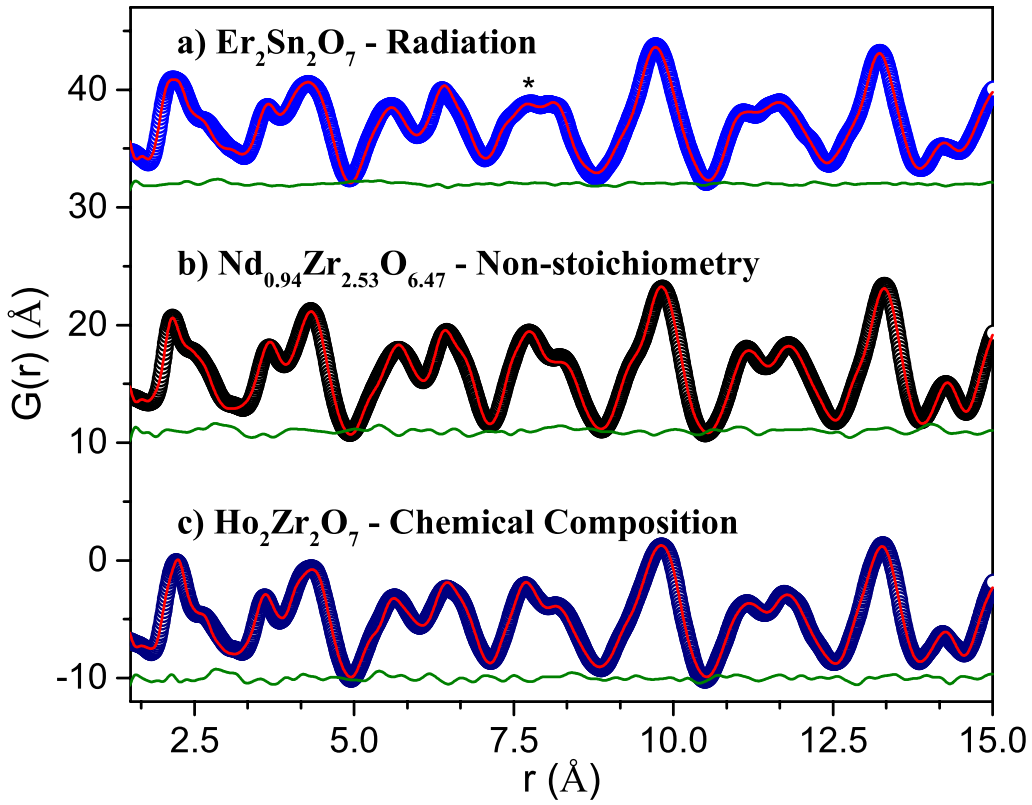

Figure 27: Refined PDFs for pyrochlores disordered by (a) irradiation with 2.2 GeV Au ions ($Er_2Sn_2O_7$), (b) non-stoichiometry ($Nd_{0.94}Zr_{2.53}O_{6.47}$), and (c) chemical composition ($Ho_2Zr_2O_7$).

Independently of the starting composition and means of disordering, the local structure can be in each case accurately refined with the weberite-type phase (Table 4); the fluorite phase is only consistent with the average, disordered structure. Thus, the same disordering mechanism operates independently of the source of the disorder (intrinsic or extrinsic).

The discovery of the local weberite-type structure in fully disordered pyrochlore is essential to the description of atomic-scale phase transformations of such materials under extreme conditions. Atomistic simulations almost exclusively adopt a fully disordered fluorite model or focus on single defect energies to predict physical properties such as radiation stability and disordering temperature [24, 25, 42]. In general, this approach has reproduced similar trends as experiment, however, the heterogeneous disorder presented here undoubtedly affects the energy landscape and needs to be accounted for to fully understand the order-to-disorder transition. For example, cation antisite and anion Frenkel pairs are energetically very expensive in $Er_2Sn_2O_7$ [24]. However, previous experiments have shown that this compound forms the fluorite phase under particle radiation [33], which would be unexpected if local ordering did not play a key role in the order-to-disorder transition.

This transition also affects high-pressure behavior of many pyrochlore compositions. At room temperature and a critical pressure of ~20 GPa, isometric pyrochlore transitions to an orthorhombic, cotunnite-like phase [26, 27] which transforms to the disordered fluorite structure upon quenching. While this phase-transformation has been studied in detail, the structural relation among the different phases and the associated pathways are not well understood. This new insight into heterogeneous disorder provides the atomic-scale relationship between the three structures and a potential transformation mechanism. The cotunnite-like (*Pnam*) structure is a non-isomorphic subgroup of the orthorhombic (*Ccmm*) local coordination that has been here shown to exist in disordered fluorite compounds. Analogous to chemical composition, non-stoichiometry, and radiation,

pressure likely disorders the local pyrochlore structure into orthorhombic units. The applied pressure, however, hinders structural modulations, resulting in long-range orthorhombic periodicity. Once pressure is released, the long-range structure relaxes into disordered fluorite on average.

Total scattering data on isometric spinel shows that this complex disordering mechanism extends beyond the fluorite system. Many compounds of AB_2O_4 stoichiometry form an isometric spinel structure that, like pyrochlore, can be disordered by changing composition [118], irradiation [119], and temperature/pressure [120, 121]. The local (assessed with PDF, Figure 28a) and average (assessed with diffraction, Figure 29) structure of $MgAl_2O_4$ agree well with isometric spinel (Figure 28d) although minor distortions appear to be present at 2.8 Å. Unlike $MgAl_2O_4$, $NiAl_2O_4$ forms an inverse spinel structure in which tetrahedrally coordinated A-site cations exchange with nearly half of octahedrally coordinated B-site cations (indicated as $B(AB)O_4$). The octahedral sublattice can therefore be viewed as fully disordered, on average, as A- and B-site cations are "randomly" distributed across octahedral sites (Figure 30). The PDF, however, shows that this description is not valid locally as evidenced by the deviations between the measured data and the refinement at low-*r* (Figure 28b). The tetragonal spinel phase with three ordered cation sites and a different unit cell orientation (Figure 28e) agrees well with the PDF (Figure 28c), indicating the cations are locally ordered within a tetragonal "unit cell" (Figure 31). This also improves the fit of the peak at 2.8 Å for $MgAl_2O_4$ (Figure 32). This is consistent with Raman spectroscopy measurements on inverse $NiFe_2O_4$ [122] and agrees with first principles calculations demonstrating that short-range effects must be included to accurately predict cation inversion tendencies [123]. This relationship is analogous to that of weberite-type/pyrochlore. Just as the pyrochlore is a 2×2×2 superstructure of fluorite, spinel can be viewed as a 2×2×2 superstructure of NaCl [118]. Upon disordering, the local "unit cell" is reduced to an approximately $2\times\sqrt{2}\times\sqrt{2}$ supercell of its base structure (i.e., fluorite or NaCl).

Figure 28: Neutron PDFs and structural models for normal ($MgAl_2O_4$) and inverse ($NiAl_2O_4$) spinel.

(a) Small-box refinement of $MgAl_2O_4$ spinel using the isometric (*Fd*-3*m* space group) average structure (d). The refined inversion fraction is 0.36(4) which denotes the fraction of Mg atoms that share mixed occupancy of octahedral B-sites (indicated by blue spheres) with Al. The shown polyhedra are A-site tetrahedra. The isometric structure fits reasonably well, however, there is evidence of minor local distortions as noted by the refined width and height of the peak at 2.8 Å. This is likely due to partial ordering of the Mg/Al atoms occupying octahedral B-sites as the tetragonal distortion discussed in (c) models this peak accurately (Figure 32).

(b) Refined PDF of $NiAl_2O_4$ spinel using the isometric (*Fd*-3*m* space group) average structure (d). The refined inversion fraction is 0.82(2). The position and left shoulder of the first peak are not captured through refinement and several other intensities are poorly modeled.

(c) Refined PDF of $NiAl_2O_4$ spinel using a tetragonal distortion (e) with three distinct cation sites ($P4_122$ space group) resulting in an "inversion" fraction of 0.86(2) denoting the fraction of Ni that occupy 4*a* octahedral sites (shown as grey spheres). The 4*b* octahedral sites (blue spheres) are fully occupied by Al atoms. The remaining Ni atoms share occupancy of 4*c* tetrahedral sites with Al (shown as cyan polyhedra). Tetrahedra are slightly distorted and shifted from their ideal isometric lattice sites, otherwise the A-site sublattice is unchanged from that of the isometric spinel. The shoulder and position of the first peak are now modeled accurately and refined peak intensities now line up favorably with the measured data. All PDFs were refined from 1 – 10 Å.

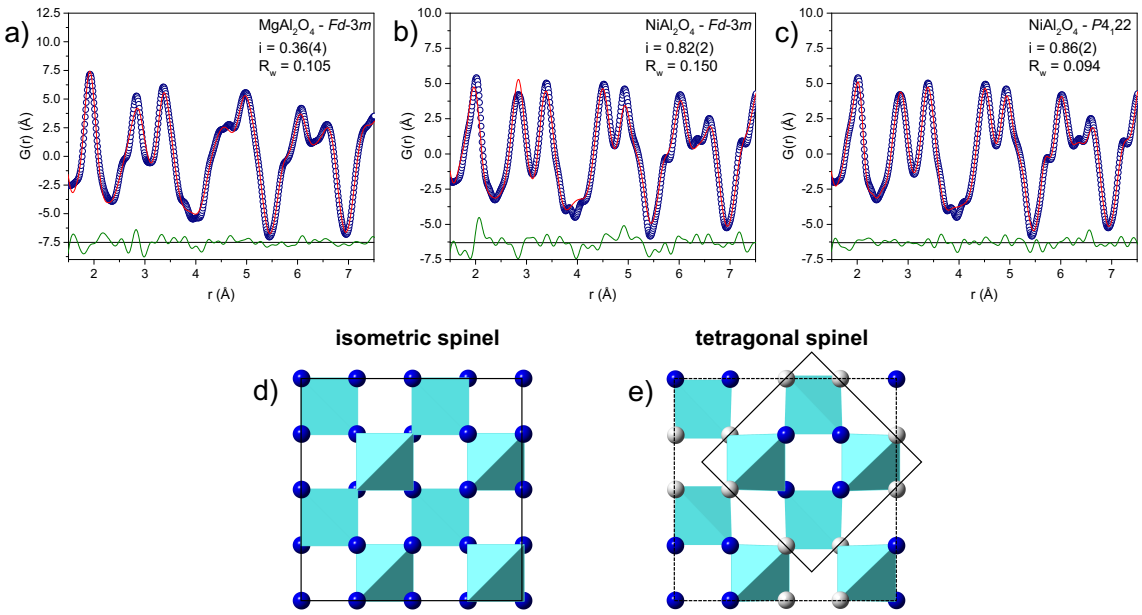

Figure 28. Continued.

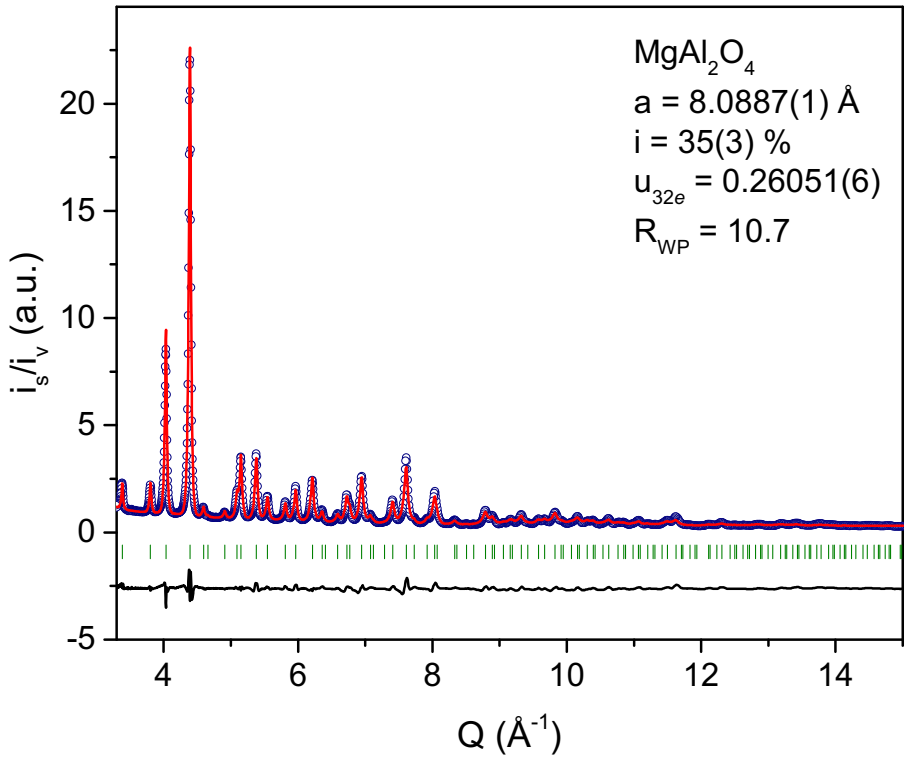

Figure 29: Neutron diffraction pattern of $MgAl_2O_4$ (open circles).

Rietveld refinement using the isometric spinel structure (solid red line, Fd-3m space group) agrees well with the experimental data. The inversion fraction (i) was refined to be 0.35(3) which denotes the fraction of Mg that occupy octahedral sites. The difference between the measured data and the refinement is shown as a solid black line. The green ticks denote refined Bragg positions.

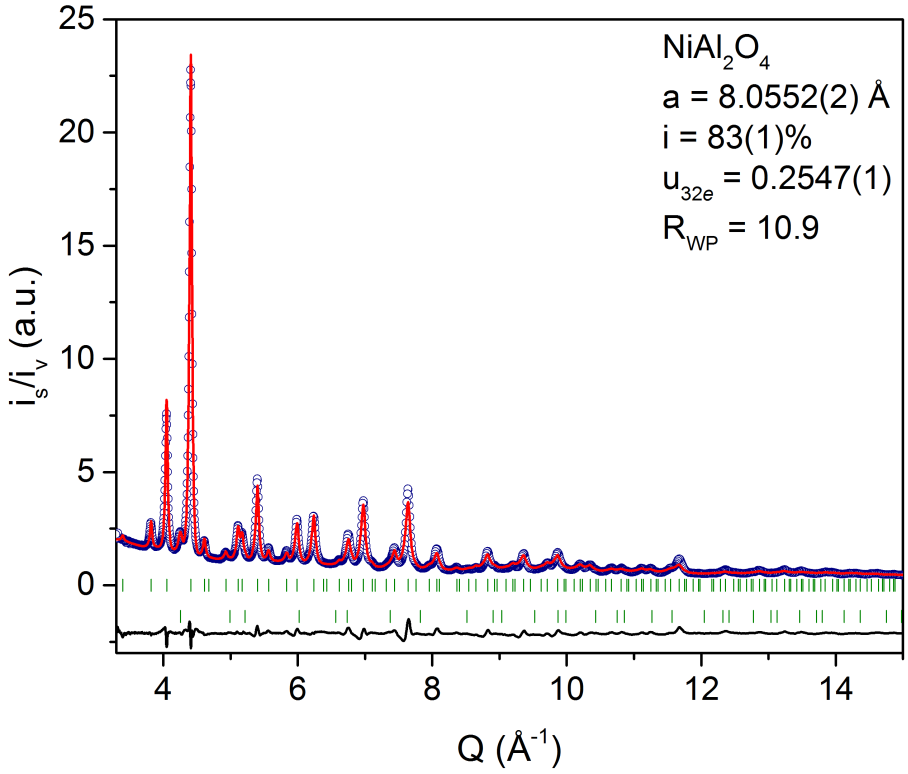

Figure 30: Neutron diffraction pattern of $NiAl_2O_4$ (open circles).

Rietveld refinement of NiAl2O4 using the isometric spinel structure (solid red line, Fd-3m space group). The inversion fraction (i) was refined to be 0.83(1) which denotes the fraction of Ni that occupy octahedral sites. The difference between the measured data and the refinement is shown as a solid black line. Refined Bragg peak positions from the spinel structure are designated by the top row of green tick marks. An additional peak that cannot be indexed with the isometric spinel structure is observed at 4.25 Å-1 which is likely due to unreacted NiO (Bragg positions shown in bottom row of ticks). This was refined to be only 0.24(3)% of the volume fraction contributing to the diffraction pattern and has a negligible effect on the pair distribution function.

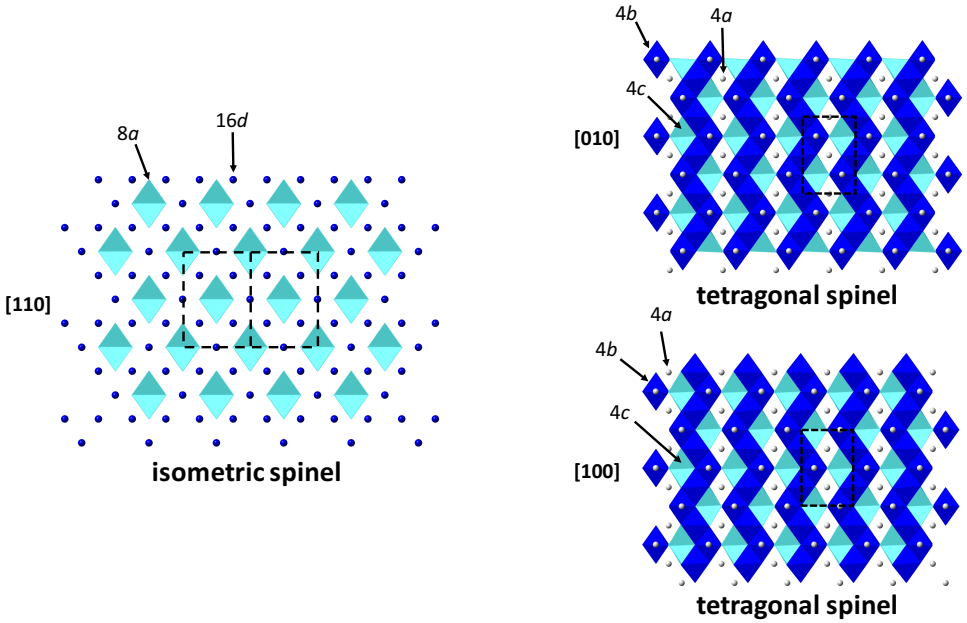

Figure 31: Relationship between the isometric (*Fd*-3*m*) (left) and tetragonal ($P4_122$) spinel (right) structure-types.

The dashed black lines delineate the respective unit cells. The tetrahedral (8a) sublattice in isometric spinel is preserved but is slightly distorted in the tetragonal orientation (4c). The octahedral (16d) sublattice in isometric spinel is ordered with two separate cation sites (4a and 4b) of differing sizes in the tetragonal distortion. 4a and 4b octahedral sites form helical chains in the [001] direction.

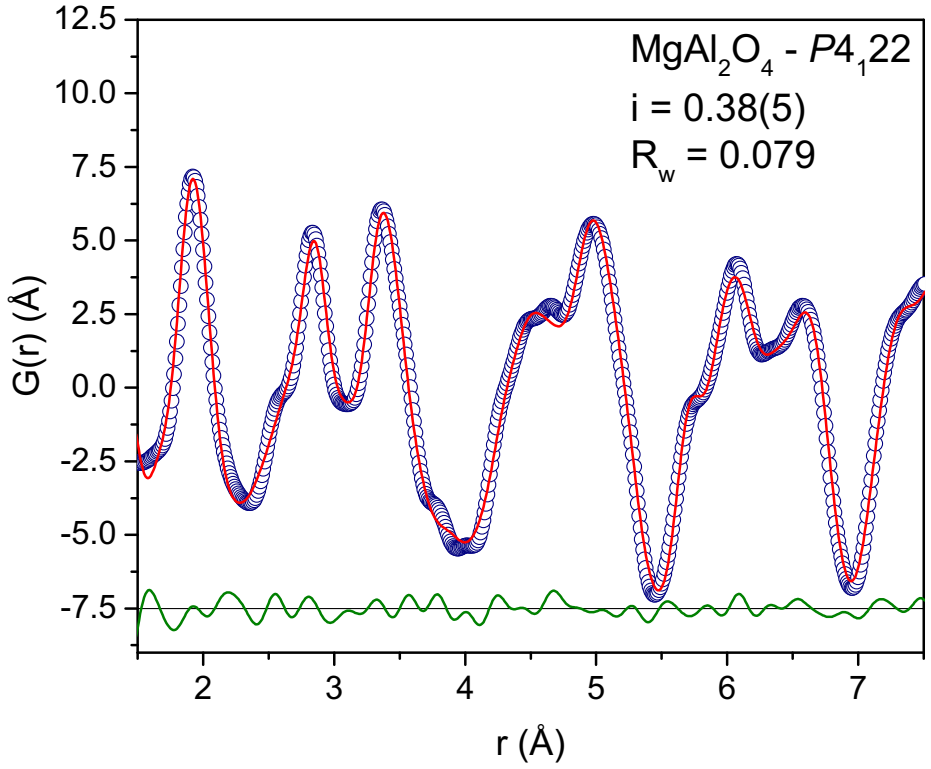

Figure 32: Experimental PDF of $MgAl_2O_4$ (open circles) refined using a tetragonal distortion with three distinct cation sites (solid red line, $P4_122$ space group).

The "inversion" fraction was refined to be 0.38(5) which denotes the fraction of Mg that occupy 4a octahedral sites. The intensity and width of the peak at 2.8 Å are both modeled accurately in contrast to refinement with the isometric spinel structure (Fd-3m space group).

In summary, PDF analysis from neutron total scattering has provided new insight into disorder in isometric complex oxides. In particular, the isometric, fluorite structure in disordered $A_2B_2O_7$ does not exist at the atomic level. These complex oxides consist of local orthorhombic structural units that are pseudo-randomly arranged to form the well-known average disordered fluorite structure. This modulated structure is consistent whether disorder is introduced extrinsically (irradiated $Er_2Sn_2O_7$) or intrinsically ($Ho_2Zr_2O_7$ and $Nd_{0.94}Zr_{2.53}O_{6.47}$). Similar behavior is observed for spinel inversion, as modulations of a local tetragonal configuration form a disordered isometric structure on average. Understanding the nature of this heterogeneous disorder presents a new basis for the study of structural and physical properties in a broad class of complex oxides. Just as short range effects have been shown to be computationally necessary in spinel [123], atomistic simulations which neglect local ordering in disordered pyrochlores represents an incomplete approach to fully understand the disordering process. We have shown, for the first time, that this local order in both pyrochlore and spinel systems does not arise from the ordered, isometric structure but rather from a smaller unit cell of lower symmetry. This can be used to improve predictions for important properties such as disordering temperature, ionic conductivity, and radiation stability.

CHAPTER III

LOCAL ORTHORHOMBIC ORDER IN DISORDERED AND AMORPHOUS PYROCHLORES INDUCED BY HIGH-ENERGY ION RADIATION

Abstract

Chapter II revealed important insights into local ordering in disordered fluorite-type complex oxides. It was shown that orthorhombic, weberite-type ordering exists on short length scales (< 15 Å) for materials that were disordered by radiation, composition, and altering the $A_2B_2O_7$ stoichiometry. It is still unclear, however, if there is local ordering in *amorphous* pyrochlores and, if so, how it compares with *disordered* (fluorite) pyrochlores. Here we present neutron total scattering measurements on $Er_2Sn_2O_7$ and $Dy_2Sn_2O_7$ irradiated with relativistic heavy ions to very high fluences ($8x10^{12}$ ions/cm^2). Neutron diffraction measurements show a pyrochlore to disordered fluorite transformation for $Er_2Sn_2O_7$ while $Dy_2Sn_2O_7$ shows a transition to an amorphous state. Despite contrasting behavior over long length scales, pair distribution function (PDF) analysis reveals that both $Er_2Sn_2O_7$ and $Dy_2Sn_2O_7$ show evidence of orthorhombic, weberite-type ordering when analyzed at less than 5 Å. This congruence between a disordered ($Er_2Sn_2O_7$) and an amorphous ($Dy_2Sn_2O_7$) sample reveals that radiation induced phase transformations are more complicated than previously thought and likely involve mesoscopic modulations of locally ordered structural units. For disordered fluorite structures, pseudo-periodic modulations were found which maintained crystallinity over the entire length scale, while in amorphous materials modulations must be aperiodic to explain the observed loss in long-range crystallinity.

Experimental Methodology

Swift Heavy Ion Irradiation

Irradiations were performed at the X0 beamline of the GSI Helmholtz Center for Heavy Ion Research in Darmstadt, Germany using 2.2 GeV ^{197}Au ions. Polycrystalline $Er_2Sn_2O_7$ and $Dy_2Sn_2O_7$ powders were evenly dispersed and pressed into milled cylindrical indentations (diameter = 1 cm, thickness = 70 μm) in customized aluminum sample holders (Figure 6). The mass per holder was

calculated to be 24.673 mg and 24.353 mg for $Er_2Sn_2O_7$ and $Dy_2Sn_2O_7$ respectively using the methodology outline on page 23. The mean energy loss across the sample was 47.3(10) keV/nm and 46.5(12) keV/nm (Figure 33). A total of four sample holders were used for each ion fluence to obtain sufficient irradiated sample mass for high quality neutron measurements (~ 100 mg). $Er_2Sn_2O_7$ was irradiated to four ion fluences (7×10^{11}, 2×10^{12}, 5×10^{12}, and 8×10^{12} ions/cm^2) while $Dy_2Sn_2O_7$ was only irradiated to the maximum fluence of 8×10^{12} ions/cm^2. An additional sample of each composition was used as unirradiated reference sample for the neutron measurements. Following irradiation, pellets were removed from the sample holders and ground into powders which were loaded into 2mm quartz capillaries for neutron scattering measurements as outlined in detail on page 23.

Transmission Electron Microscopy (TEM) Measurements

In order to study the damage produced by single ions penetrating the sample, the fluence was limited to 3×10^{11} ions/cm to prevent track overlap. The electron beam in was oriented along the axial direction of the ion trajectory to obtain cross-sectional views of the ion tracks. The microscope operated in bright field mode was used to determine a representative track size since many tracks can be viewed at once without altering settings (Figure 34a). Because the track cross sections are not perfectly cylindrical the mean diameter for each track was calculated by averaging the diameter measured in seven different directions. The mean track diameter for all tracks was then calculated by averaging the mean diameter of seven individual tracks. The error was obtained by taking the standard deviation of the 49 individual measurements.

Neutron Total Scattering Measurements

Neutron total scattering measurements were performed at the Nanoscale Ordered Materials Diffractometer (NOMAD) beamline at the Spallation Neutron Source located at Oak Ridge National Laboratory [89]. All measurements were taken at room temperature.

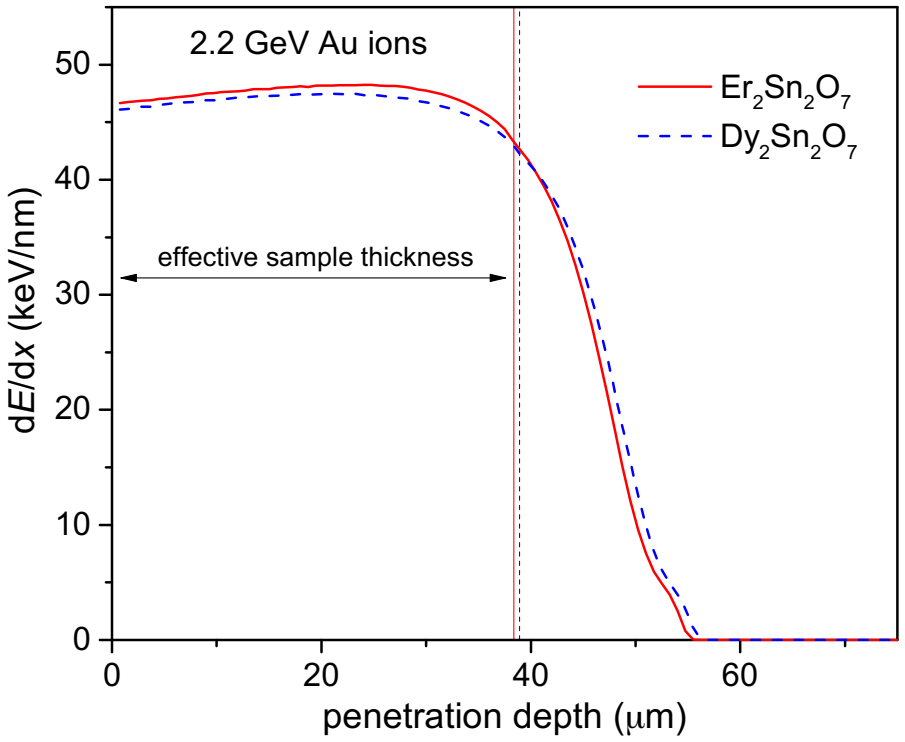

Figure 33: Effective sample thickness for $Er_2Sn_2O_7$ and $Dy_2Sn_2O_7$ irradiated with 2.2 GeV Au ions.

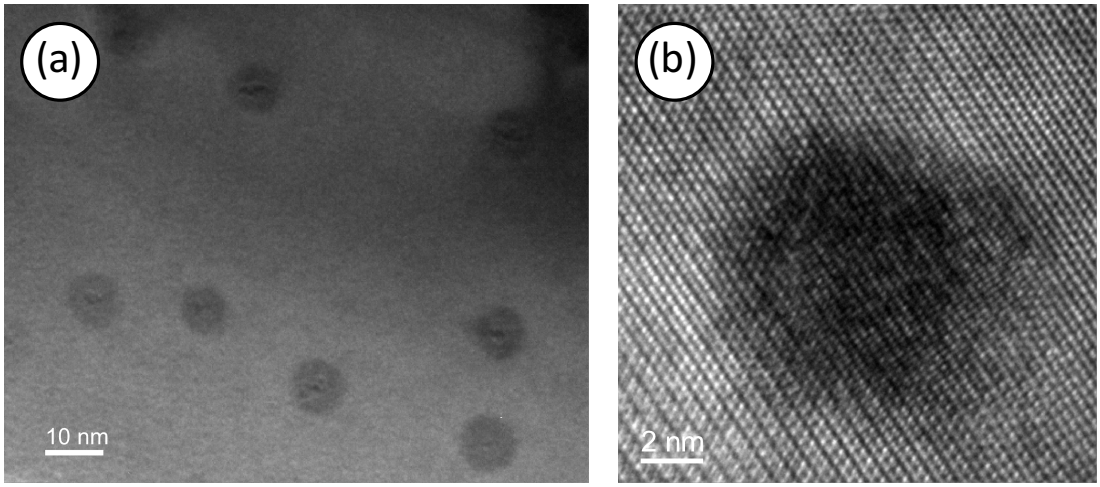

Figure 34: Bright field (a) and high resolution (b) transmission electron microscopy images of 2.2 GeV Au ion tracks in $Er_2Sn_2O_7$.

The mean track diameter extracted from bright field measurements is 8.5(8) nm.

$Er_2Sn_2O_7$ and $Dy_2Sn_2O_7$ samples were measured for 100 and 140 minutes respectively with $Dy_2Sn_2O_7$ being measured longer to account for the large neutron absorption resonances in Dy atoms.

The total scattering structure function, $S(Q) - 1$, was obtained using Eq. (16) and (17) and the reduced pair distribution function, $G(r)$, was calculated using Eq. (15). The $S(Q) - 1$ function was multiplied by a Lorch function [124] to dampen noise at high Q values, particularly in irradiated samples. A value of 0.1 $Å^{-1}$ and 31.4 $Å^{-1}$ was used for Q_{min} and Q_{max} respectively for Fourier transformation.

Results

Transmission Electron Microscopy

Bright-field TEM images revealed well-resolved ion tracks for $Er_2Sn_2O_7$ (Figure 34a). Contrast between tracks and the surrounding pyrochlore matrix indicates structural modification caused by each impinging ion. The mean track diameter was calculated to be 8.5(8) nm. The microscope operated in high resolution mode reveals little, if any, evidence of amorphization within a single ion track (Figure 34b). Ordered structures can still be resolved within the ion track. The dark contrast suggests that the transformed region is heavily strained making it difficult to determine a transformation to a fluorite-type structure.

Average Structure - Neutron Total Scattering (8×10^{12} ions/cm^2)

Disorder induced by radiation is readily apparent in the $Er_2Sn_2O_7$ sample by noting the reduced intensity and disappearance of superstructure reflections in S(Q) – 1 for the sample irradiated to 8×10^{12} ions/cm^2 as compared with the pristine sample (Figure 35a). There is no evidence of a large diffuse peak suggesting that there has mainly been a transformation to a disordered but still crystalline phase rather than radiation induced amorphization which agrees with HRTEM images. There are, however, small diffuse peaks associated with structural modulations of local Weberite-type ordering described in Chapter II.

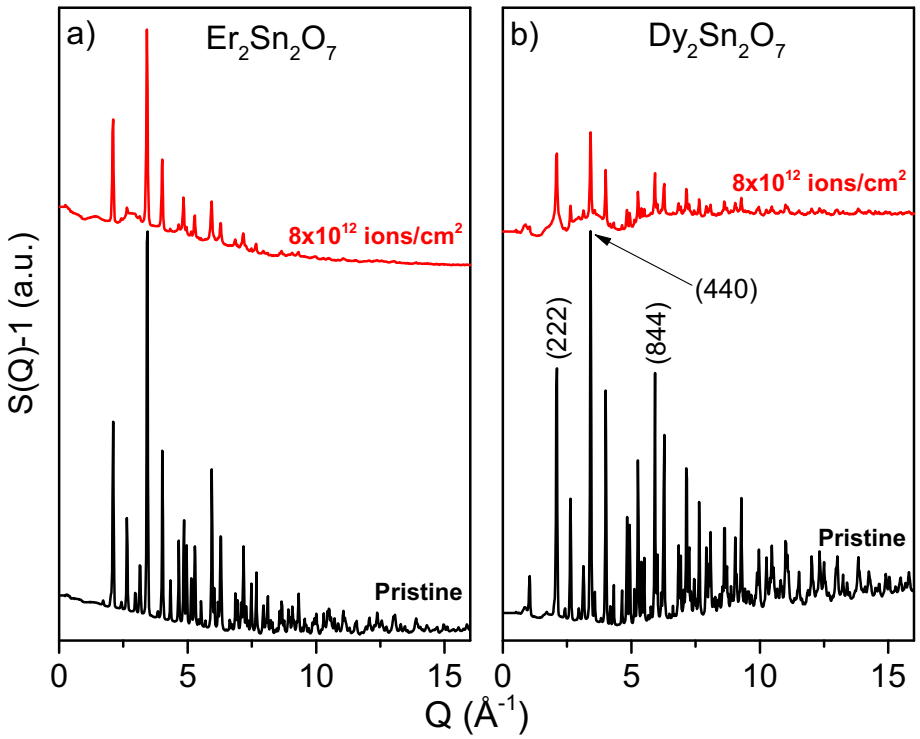

Figure 35: Total scattering structure function [S(Q)-1] for $Er_2Sn_2O_7$ (a) and $Dy_2Sn_2O_7$ (b) before and after ion irradiation.

$Dy_2Sn_2O_7$, however, shows a drastically different radiation response in S(Q) – 1 data (Figure 35b). Where the $Er_2Sn_2O_7$ largely remained crystalline, $Dy_2Sn_2O_7$ shows evidence of radiation induced amorphization as three broad diffuse bands develop under the (222), (440), and (844) structural peaks when irradiated to $8x10^{12}$ ions/cm^2 which is consistent with amorphization in pyrochlore characterized by synchrotron X-ray diffraction [68]. These diffuse peaks are not observed in the irradiated $Er_2Sn_2O_7$ samples or other fully disordered, defect-fluorite samples in [125]. Superstructure reflections are still observable for the most part, also suggesting that a predominantly amorphous rather than defect fluorite transition occurred.

Average Structure - Diffraction

Rietveld refinements were performed using the highest resolution bank at the NOMAD beamline (bank 5) which is positioned at an average scattering angle of 154 degrees. Refinement using the pyrochlore structure of unirradiated $Er_2Sn_2O_7$ and $Dy_2Sn_2O_7$ produces very reasonable fits (R_{WP} = 10.02 and 7.08 respectively) and shows no evidence of preexisting disorder or impurities. Radiation-induced disordering to the defect-fluorite structure is evidenced through two-phase refinement for $Er_2Sn_2O_7$ and the relative phase fraction increases from 7×10^{11} to 8×10^{12} ions/cm^2 initially linear and saturates at higher fluences (Figure 36). This behavior is indicative of a single-impact mechanism [126] in the form of Eq. (23) but replacing f_a (amorphous fraction) with f_{DF} (disordered fluorite fraction). This occurs when each ion creates a single cylindrical ion track. Each impinging ion creates disorder within a single track and at low ion fluences these disordered fluorite regions accumulate proportionally with increasing ion impacts. At medium to higher fluences however, tracks begin to overlap which leads to a saturation effect as no new damage (that can be detected by diffraction) is created in the overlapping regions. An effective track diameter was determined by fitting Eq. (23) to the data and assuming cylindrical ion track geometry in the form of Eq. (24).

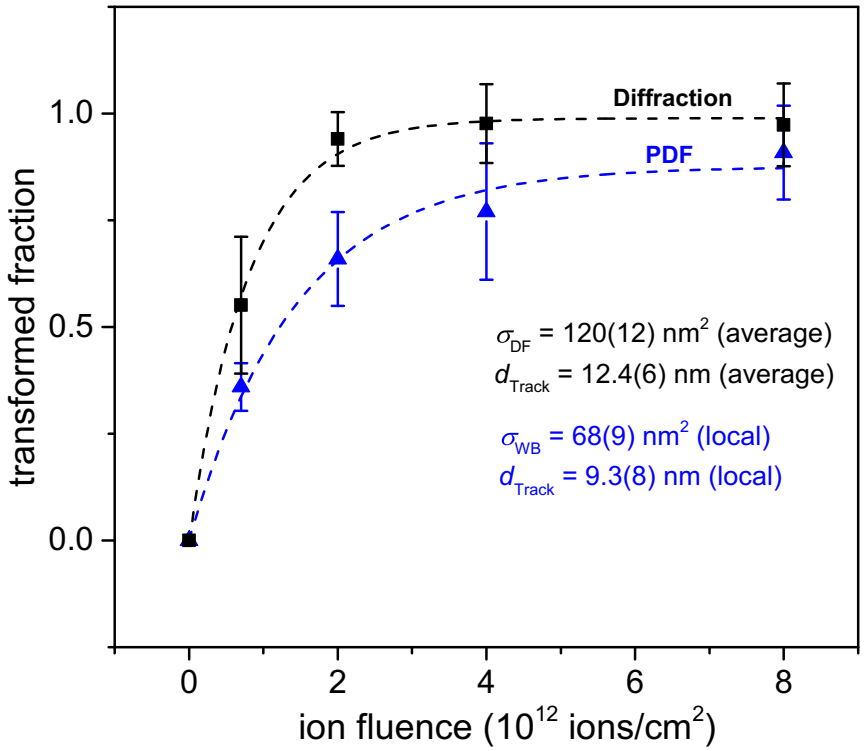

Figure 36: Pyrochlore to disordered fluorite transformation in irradiated $Er_2Sn_2O_7$ as a function of ion fluence.

Black squares were determined *via* Rietveld refinement of neutron diffraction data while blue triangles were determined *via* small-box refinement of neutron PDF data. Dashed lines are fits based on a single-impact mechanism yielding the cross-sections σ_{DF} and σ_{WB}.

The disordered fluorite cross section was calculated to be 120(12) nm^2 leading to an effective track diameter of 12.4(6) nm. $Dy_2Sn_2O_7$ was not irradiated to multiple fluences and Rietveld refinement of a pyrochlore-to-fluorite transformation would be difficult due to the build-up of the amorphous phase.

Local Structure – PDF (Disorder vs. Amorphization: Pristine vs. 8×10^{12} ions/cm^2)

The local structure probed by neutron PDF in the fully ordered $Er_2Sn_2O_7$ (Figure 37a) and $Dy_2Sn_2O_7$ (Figure 37b) pyrochlores agree very well with the average pyrochlore structure used in Rietveld refinement. This agreement reveals that there are no local distortions in the as-synthesized samples.

Neutron PDFs for $Er_2Sn_2O_7$ (Figure 38a) and $Dy_2Sn_2O_7$ (Figure 38b) samples irradiated to the maximum fluence of 8×10^{12} ions/cm^2 show different responses at intermediate *r*-ranges (r > 7.5 Å) relative to the original pyrochlore structure. Intermediate peaks in irradiated $Er_2Sn_2O_7$ broaden significantly and convolute into single peaks (note asterisks in Figure 38a). This is indicative of a transition to a disordered but largely still crystalline phase. Intermediate peaks in irradiated $Dy_2Sn_2O_7$, however, show minimal broadening but instead peak areas are significantly reduced relative to low-*r* peaks. This directly indicates that all atom-atom coordination is being lost at these *r*-ranges which is consistent with the amorphous transition observed in the neutron diffraction data Figure 35b. The remaining peaks are likely from unirradiated regions in the original pyrochlore structure. This is evident by refining the pyrochlore phase as a function of fit-range (Figure 39). The pyrochlore model is very poor when refining from 1.5 – 11.5 Å (R_{WP} = 0.362). The R_{WP} value linearly decreases with increasing fit-range out to 9 – 19 Å and saturates at higher *r*. The minimum R_{WP} for the irradiated sample was 0.125 and corresponds to a fit range of 16.5 – 26.5 Å. This compares very favorably to the unirradiated sample refined with the same fit range (R_{WP} = 0.111).

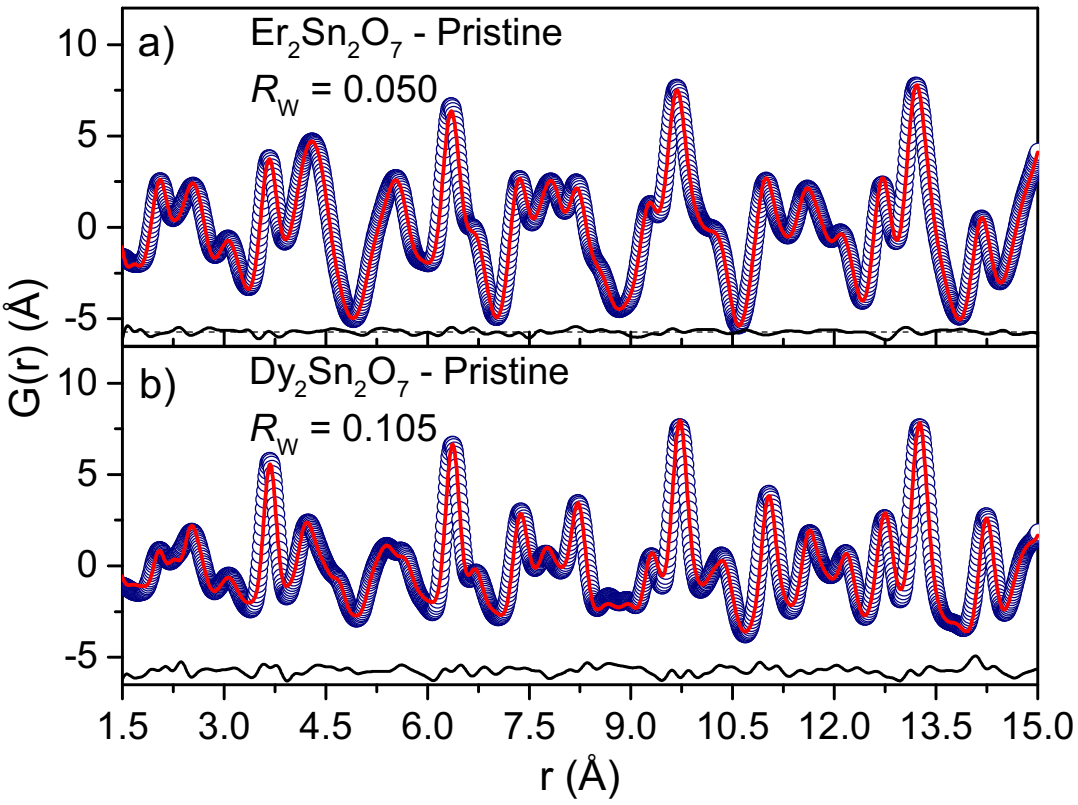

Figure 37: Neutron PDFs (open blue circles) refined with the pyrochlore structure (red lines) for pristine $Er_2Sn_2O_7$ (a) and $Dy_2Sn_2O_7$ (b).

The pyrochlore model agrees with the experimental data well for both compositions.

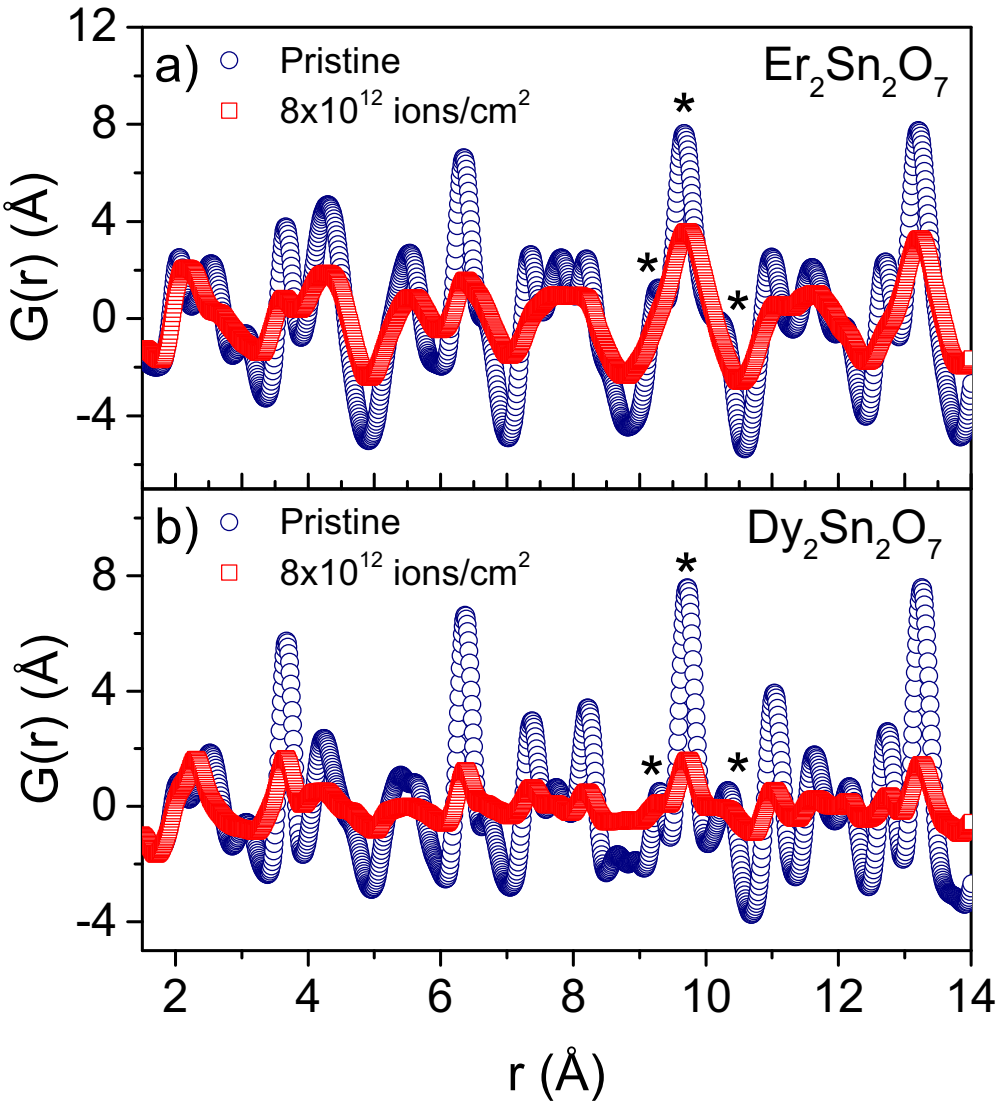

Figure 38: Neutron PDFs for pristine (open blue circles) and irradiated (open red squares) $Er_2Sn_2O_7$ (a) and $Dy_2Sn_2O_7$ (b) with 2.2 GeV Au ions to a fluence of 8×10^{12} ions/cm^2.

Disorder is readily apparent in ion irradiated $Er_2Sn_2O_7$ by broadening and merging of remaining pyrochlore peaks (see asterisks) Peaks in ion irradiated $Dy_2Sn_2O_7$ are significantly reduced in area and do not show pronounced merging, suggesting partial amorphization in this pyrochlore composition instead of disordering

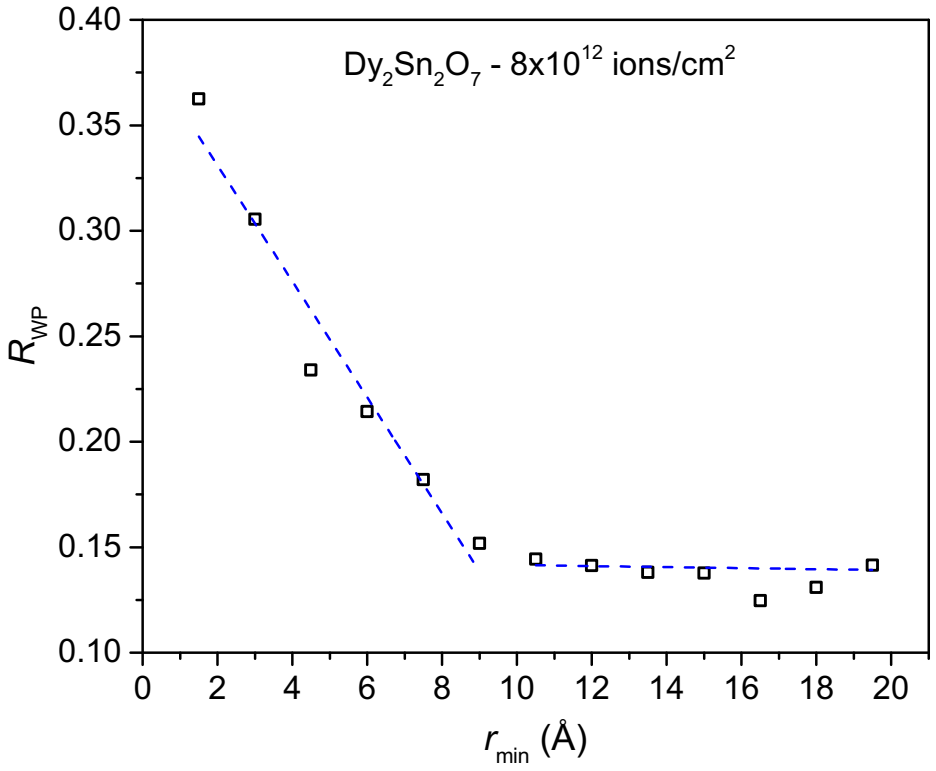

Figure 39: Goodness-of-fit parameter (R_{WP}) for neutron PDFs of $Dy_2Sn_2O_7$ irradiated to 8×10^{12} ions/cm^2 refined with the pyrochlore structure at multiple fit ranges.

The *x*-axis (r_{min}) represents the minimum *r*-value used for refinement. All fit ranges were 10 Å (i.e. 1.5 – 11.5 Å). The R_{WP} value saturates at fit-ranges beyond 9 – 19 Å.

This indicates that these correlations indeed arise from unirradiated pyrochlore regions and radiation induced changes have no atomic coordination in this saturated regime. The amorphous phase in $Dy_2Sn_2O_7$ is therefore weakly correlated out to about 9 Å.

While the average structural response (determined by S(Q) – 1) and intermediate *r*-range (r > 7.5 Å in the neutron PDFs) display different radiation responses, $Er_2Sn_2O_7$ and $Dy_2Sn_2O_7$ show similar modifications at lower *r*-ranges (r < 3 Å, Figure 40a and Figure 40b respectively). It is immediately apparent in $Er_2Sn_2O_7$ irradiated to 8×10^{12} ions/cm^2 that the local structure is significantly modified from the original pyrochlore ordering (Figure 40a). Vertical dashed lines represent the refined atom-atom correlation positions from the pristine $Er_2Sn_2O_7$ sample. All atoms have positive neutron scattering lengths so it is coincidental that the Er – O2 (O2 refers to 8*b* oxygens) peak appears to be a trough in the PDF. Er is coordinated with only two O2 atoms and this peak is highly convoluted with the Sn – O1 and Er – O1 peaks (O1 refers to 48*f* oxygens). After irradiation, the Sn – O1 peak decreases slightly while the Er-O1 peak decreases significantly suggesting the Er – O1 bonds are more susceptibility to modification than the Sn – O1 bonds. A new peak develops near the Er – O2 peak in the pristine pyrochlore. Since Er – O1 decreases much more significantly than Sn – O1, this could be viewed as the Er – O1 peak shifting to the left. Despite this shift in bond length, the O1 – O1 peak remains close to its original location in the pristine pyrochlore. This indicates a change of symmetry as a structural distortion would be necessary to change the Er – O1 bond length without changing O1 – O1. This was described in Chapter II to be a transformation to a weberite-type structure [127].

Despite amorphizing over longer length scales, $Dy_2Sn_2O_7$ shows a strikingly similar radiation response at low-*r*. The Sn – O1 and Dy – O1 peaks both decrease in similar fashion compared to the Sn – O1 and Er – O1 peaks in Er_2SnO_7 while a new peak forms between them. As in $Er_2Sn_2O_7$, this can be viewed as the Dy – O1 peak shifting to the left.

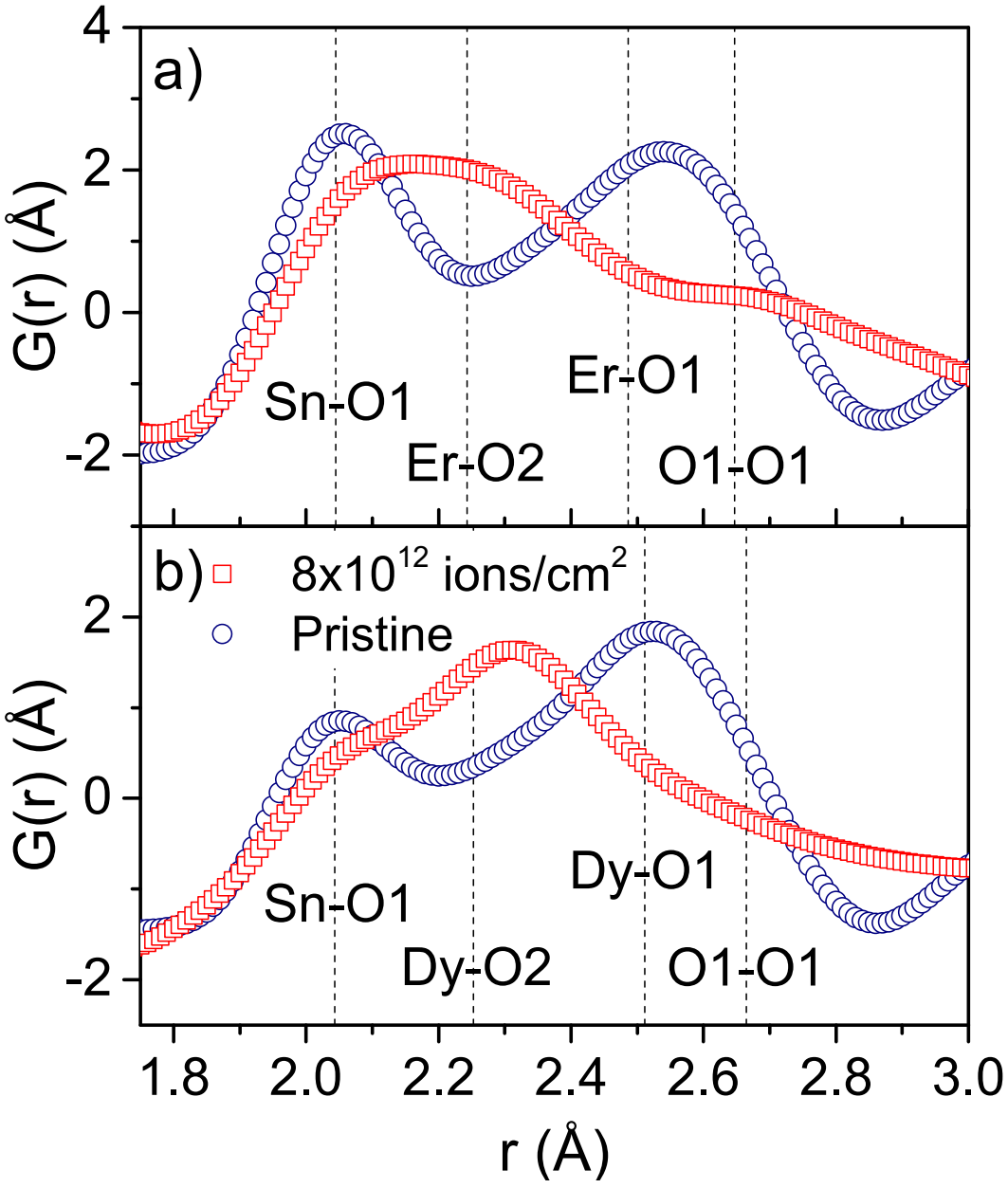

Figure 40: Neutron PDFs from 1.75 to 3 Å for pristine (open blue circles) and ion irradiated (open res squares) $Er_2Sn_2O_7$ (a) and $Dy_2Sn_2O_7$ (b).

Dashed vertical lines denote refined atom pair positions in the pristine pyrochlore samples. O1 and O2 refer to 48*f* and 8*b* oxygens respectively.

The scattering lengths for Dy and Sn (16.9 – 0.276*i* fm and 6.225 fm respectively) are much more contrasting than Er and Sn (7.79 fm and 6.225 fm respectively) which creates more resolution in the PDF. For example, it is apparent that the new peak forming after irradiation is actually at higher *r* relative to the Dy – O2 peak in the pristine pyrochlore structure. It is difficult to tell if this is true for the new peak in $Er_2Sn_2O_7$ as it's highly convoluted with Sn – O1. Nonetheless, both a sample that disordered to a fluorite average structure ($Er_2Sn_2O_7$) and one that amorphized ($Dy_2Sn_2O_7$) show analogous behavior when analyzed over very short length scales and are consistent with a weberite-type transformation.

Disordered Phase Development in $Er_2Sn_2O_7$ (Small-box refinement)

The development of local disorder in $Er_2Sn_2O_7$ as a function of ion fluence was analyzed through small-box refinement of the neutron PDFs from 1.5 – 15 Å. The sample irradiated to the highest ion fluence (8×10^{12} ions/cm^2) was analyzed first in order to determine the general transformation behavior. Four different structural models were fit to the data: i) a complete transformation to defect fluorite, ii) a complete transformation to weberite-type, iii) a mixed phase of defect fluorite and pyrochlore and iv) a mixed phase of weberite-type and pyrochlore (Figure 41a-d respectively). The mixed phase models were included to account for incomplete ion track coverage at 8×10^{12} ions/cm^2. Focusing first on the two single-phase models, the weberite-type transformation far outperforms the defect fluorite transformation (R_{WP} = 0.092 and 0.241 respectively). The mixed phase models both indicate that the sample is primary disordered at 8×10^{12} ions/cm^2 with a refined transformation fraction (f_{DF} and f_{WB}) of 0.82(5) and 0.91(10) for the defect fluorite (Figure 41c) and weberite-type (Figure 41d) models respectively. The pyrochlore and weberite-type model is superior to the the pyrochlore and defect fluorite model. The refined weberite-type fraction is within error of a complete transformation. Due to the poor fits, the defect fluorite model was no longer used to study the order/disorder transformation as a function of ion fluence.

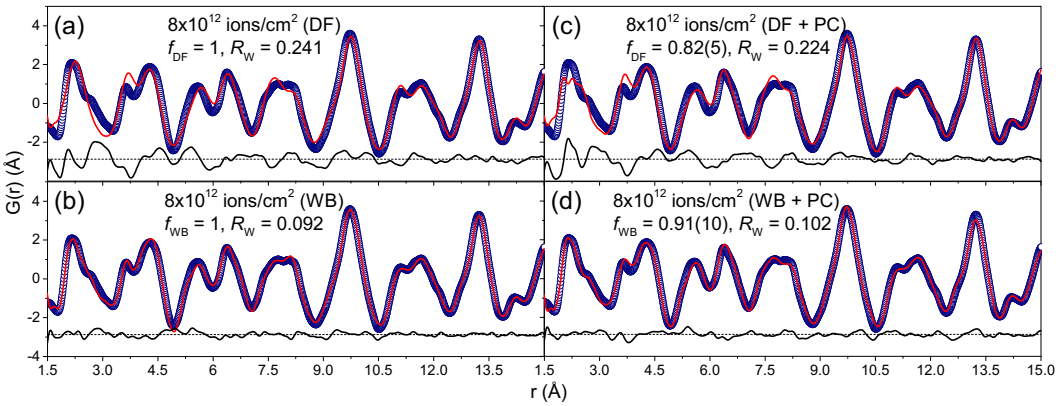

Figure 41: Neutron PDFs (open circles) for ion irradiated $Er_2Sn_2O_7$ refined with the disordered fluorite model (a), the weberite-type model (b), a mixed phase disordered fluorite and pyrochlore model (c) and a mixed phase weberite-type and pyrochlore model (d) (solid red lines).

The fits from models incorporating weberite-type ordering outperform those incorporating disordered fluorite. f_{DF} and f_{WB} refer to the refined fraction of disordered fluorite and weberite-type contributing to the refined pattern respectively.

The transformed fraction initially increases at 7×10^{11} ions/cm^2 but saturates at higher fluences again indicative of a single impact mechanism (Figure 36). Eq. (23) and (24) were fit to the data resulting in a track diameter of 9.3(8) nm which is within error of the mean track diameter measured through BFTEM (8.5(8) nm). This indicates that the local transformation to the weberite-type configuration proceeds at the same rate as the average defect fluorite structure.

Discussion

The effective disordered track diameter in $Er_2Sn_2O_7$ extracted through refinement of diffraction measurements (12.4(6) nm) is about 30% larger than when analyzed through PDF refinement (9.3(8) nm) and BFTEM (8.5(8) nm). This discrepancy, specifically between diffraction and TEM, is consistent with a study by Sattonnay *et al.* on disordering and amorphization in $Gd_2Zr_2O_7$, Gd_2ZrTiO_7, $Gd_2Ti_2O_7$, and $Nd_2Zr_2O_7$ in which both amorphous and total (amorphous core + disordered shell) track diameters assessed through X-ray diffraction were larger than when measured with TEM [99]. This is likely caused by a defect-rich halo beyond the direct vicinity of the observable ion track that reduces the ordering observed through diffraction peaks.

Radiation resistance in stannate pyrochlores is more complex than zirconate and titanates, which is consistent with findings by Lian et al. showing that stannate pyrochlores display a wider range of radiation tolerances [33]. Given their similar cation ionic radii ratios, $Er_2Sn_2O_7$ is unusually resistant while $Dy_2Sn_2O_7$ is easily amorphized with low-energy ion irradiation. Although unfavorable due to the high disordering energy, we've shown here that $Dy_2Sn_2O_7$ distorts to the same disordered weberite-type phase that has been shown locally for fluorite-type $A_2B_2O_7$ compounds with an r_A/r_B below the critical threshold of the pyrochlore [125]. However, the excess energy expended in creating these local defects seemingly destabilizes the long-range crystal structure. Both the calculated disordered

energy assuming a defect fluorite structure for $Er_2Sn_2O_7$ [42] as well as the formation energy of cation antisite and anion Frenkel pairs [24] are also very large and in fact much larger than $Er_2Ti_2O_7$ which has been shown to amorphize with both low-energy ions [32] and high-energy ions (shown in Chapter I) [128]. On the basis of previous understanding of the favorability of forming single defects and/or incorporating a fully disordered fluorite structure, $Er_2Sn_2O_7$ should readily amorphize in response to ion irradiation.

The only difference between amorphous $Dy_2Sn_2O_7$ and disordered $Er_2Sn_2O_7$ is whether or not the local weberite-type arrangement modulates into the fluorite type arrangement beyond ~ 10 Å which is consistent with Raman spectroscopy measurements on irradiated stannate pyrochlores [129]. The authors found that Raman spectra of both disordered and amorphous pyrochlores matched remarkably well with A_3BO_7 weberite-type complex oxides and only differ in the intensity of a single mode at ~450 cm^{-1} which is related to medium-range fluorite-like ordering. The presence of analogous local order in a disordered sample *vs.* an amorphous sample which both have high disordering energies suggests that the dominating factor determining radiation tolerance is not a materials ability to incorporate local disorder but rather its ability to incorporate pseudo-periodic mesoscopic modulations of this local disorder to maintain long-range crystallinity.

The local order in amorphous $Dy_2Sn_2O_7$ presented here is distinctly different from a recent computational study by Xiao *et. al.* on amorphization in *titanate* pyrochlores [67]. In that study, the local structural evolution was investigated as a function of electronic excitation concentration as would be produced with ionizing radiation, laser heating, etc. The local structure was represented using the radial distribution function (RDF), R(r) ($R(r) = r[G(r) + 4\pi r\rho_0]$, where G(*r*) is the reduced pair distribution function used throughout this dissertation). The authors found that above a threshold of ~ 1.5% electronic excitations, $Sm_2Ti_2O_7$, $Gd_2Ti_2O_7$, and $Y_2Ti_2O_7$ transform to an amorphous phase within several picoseconds.

Simulations showed the formation of O_2-like molecules with a correlation length of ~ 1.4 Å. The authors explained the amorphization at the cation sublattice as being driven by this O_2 formation on the oxygen sublattice. This is reflected in the modelled RDF by a new peak forming at 1.4 Å and a severe decrease in intensity in higher-*r* peaks. Based on the current neutron PDF analysis, the existence of predicted O_2-like molecules in irradiated $Dy_2Sn_2O_7$ cannot be fully excluded due to artifacts at low-*r* from background in S(Q) – 1 of the strongly absorbing Dy atoms (Figure 35b). However, the behavior of the Sn-O and Dy-O peaks after irradiation is not in agreement with the proposed O_2-driven amorphization process. The formation of O_2-like molecules is accompanied by a severe decrease in all local polyhedra correlations in the modeled RDFs. Amorphous $Dy_2Sn_2O_7$ in the present study, however, shows that local order is preserved in the form of weberite-like ordering characterized by the formation of the strong peak near the original Dy-O2 correlation. The modelled RDF of Gd_2TiO_7 does show a slight increase in coordination at the original Gd-O2 peak location but it is not the predominant correlation within the amorphous phase as it is with irradiated $Dy_2Sn_2O_7$ in the present study (Figure 40). Interestingly, the simulations also show weak correlations within the amorphous phase out to at least 7 Å which is consistent with the present study but the low-*r* region is much weaker compared with the experimental data presented here.

CHAPTER IV

CRYSTAL STRUCTURE AND PARTIAL ISING-LIKE MAGNETIC ORDERING OF ORTHORHOMBIC DY_2TIO_5

A version of this article has been previously published in by Jacob Shamblin, Stuart Calder, Zhiling Dun, Minseong Lee, Eun Sang Choi, Joerg Neuefeind, Haidong Zhou, and Maik Lang in the journal *Physical Review B*.

Shamblin, J., et al. (2016). "Crystal structure and partial Ising-like magnetic ordering of orthorhombic Dy2TiO5." Physical Review B **94**(2): 024413.

J.S. and M.L. conceived the experiment, J.S., S.C., J.N. and M.L. performed the neutron diffraction measurements, M.S.L. and E.S.C. performed the ac susceptibility measurements, J.S., Z.D., and H.D.Z. performed the dc susceptibility measurements, J.S. synthesized the sample, J.S., S.C., Z.D., and H.D.Z. analyzed the data, J.S. wrote the manuscript.

Abstract

Chapters II and III have revealed that the isometric pyrochlore structure is intimately related to the orthorhombic weberite-type structure. Altering the composition, perturbing the stoichiometry, and irradiating with high energy ions all induce local orthorhombic order in materials with long range cubic symmetry. This isometric/orthorhombic relation is further evidenced in “stuffed pyrochlores” of general formula $A_{2+x}Ti_{2-x}O_{7-x/2}$ (A = La – Lu). Fully stuffed pyrochlores (A_2TiO_5) exhibit two long-range equilibrium polymorphs: disordered fluorite (isometric) (A = Ho – Lu) and orthorhombic (A = La – Dy). The isometric members have recently received increased interest due to their close relationship with the pyrochlore structure as a source of geometrically frustrated magnetism. The magnetic properties of the orthorhombic members (with structures similar to the weberite-type structure but with *periodic* modulations), however, remain uncharacterized. This chapter serves as a starting point for characterizing the physical properties of materials with this orthorhombic phase. The structure and magnetic properties of

orthorhombic Dy_2TiO_5 have been investigated using X-ray diffraction, neutron diffraction, and ac/dc magnetic susceptibility measurements. We report a continuous structural distortion below 100 K characterized by negative thermal expansion in the [0 1 0] direction. Neutron diffraction and magnetic susceptibility measurements revealed 2D magnetic ordering begins at 3.1 K which is followed by a 3D magnetic transition at 1.7 K. The magnetic structure has been solved through a representational analysis approach and can be indexed with the propagation vector k = [0 ½ 0]. The spin structure corresponds to a coplanar model of interwoven two-dimensional "sheets" extending in the [0 1 0] direction. The local crystal field is different for each Dy^{3+} ion (Dy1 and Dy2), one of which possesses strong uniaxial symmetry indicative of Ising-like magnetic ordering. Consequently, two succeeding transitions under magnetic field are observed in the ac susceptibility which are associated with flipping each Dy3+ spin independently.

Introduction

Insulators of general formula A_2TiO_5 have attracted significant attention in recent years due to their structural and chemical diversity. Depending on the A-site cation size and/or sample synthesis method, these complex oxides can form cubic, orthorhombic, hexagonal, and monoclinic polymorphs without altering the stoichiometry [29, 30, 130-132]. As a result, these materials are suitable for a wide array of technological applications including potential actinide hosts for long-term storage in a geological repository [16, 17, 25], ion conductors for fuel cells and oxygen sensors [131], and nanoparticles in oxide dispersion strengthened (ODS) steels [133]. These materials can readily incorporate rare-earth elements into their A-site resulting in many complex magnetic interactions. They are frequently end members in solid solution series' of general formula $Ln_2(Ti_{2-x}Ln_x)O_{7-x/2}$ (often referred to as "stuffed pyrochlores") in which magnetic lanthanide elements are incrementally "stuffed" into the $Ln_2Ti_2O_7$ pyrochlore matrix increasing the relative

number of spins involved in magnetic interactions [87]. $Ho_2Ti_2O_7$, for example, forms the well-studied spin-ice state at low temperatures with locally ordered magnetic moments analogous with protons in water ice [6, 8]. Stuffing additional magnetic Ho^{3+} atoms into the pyrochlore causes interesting, and seemingly counterintuitive, behavior [86]. A fully stuffed $Ho_2(Ti_{2-x}Ho_x)O_{7-x/2}$ corresponds to $Ho_{2.67}Ti_{1.33}O_{6.67}$ (x = 0.67) or Ho_2TiO_5. Depending on the sample synthesis method, this disorders the pyrochlore (at least partially) into the isometric defect-fluorite average structure with cation mixing between the Ho^{3+} and Ti^{4+} crystallographic sites. The structure is effectively converted from a network of corner sharing tetrahedra, essential for the spin-ice state, to a network of side-sharing tetrahedra with intrinsic disorder. Despite the increased concentration of magnetic moments and partially disordered structure, the zero-point entropy per spin characteristic of frustration remains more or less unchanged from that of the original pyrochlore spin-ice [86]. Other stuffed pyrochlores with cubic Ln_2TiO_5 endmembers have also been studied in detail for both structural and magnetic properties [87]. Interestingly, none of these displayed evidence of long range magnetic order above 2 K. Magnetic interactions were shown to be predominately antiferromagnetic while Ln^{3+} spins were shown to be strongly anisotropic similar to spin-ice.

Magnetic properties of the orthorhombic polymorphs, however, have not been fully characterized. $Dy_2Ti_2O_7$, for example, is another prototypical spin-ice [134] that can be readily transformed into an orthorhombic polymorph through the stuffing procedure [132]. The fully stuffed Dy_2TiO_5 endmember (P*nma* space group) is an important material in the nuclear power industry where, due to dysprosium's large thermal neutron absorption cross section (σ_a = 997 b), it is used as a neutron absorber in control rods in Russian VVER type reactors [135, 136]. This, however, makes Dy-based compounds difficult to characterize with neutron diffraction which has perhaps deterred detailed studies into any magnetic structure. Dy_2TiO_5 is isostructural with orthorhombic Y_2TiO_5 first reported by Mumme [130] in which Y^{3+} (or Dy^{3+} in this case) and Ti^{4+} are 7- and 5-coordinated

with oxygen respectively (Figure 42a). This mixture of 7- and 5-fold coordination is rather unique as compared with other rare earth titanates of the same ternary system (such as pyrochlore or layered perovskites) in which Ln^{3+} and Ti^{4+} usually form distorted cubes and octahedra respectively. Here the 7-coordinated Ln^{3+} ions are in a monocapped octrahedral configuration while 5-coordinated Ti^{4+} form square pyramidal polyhedra (Figure 42b and Figure 42c). All atoms are located in distinct 4*c* Wyckoff positions each of which requiring an x- and z-coordinate to describe the atomic positions within the unit cell. This creates structural flexibility allowing for significant distortions of local polyhedra. While both Dy^{3+} ions form similar monocapped octahedra locally, they are coordinated differently at longer length scales. The first Dy^{3+} monocapped octahedron, from now on referred to as Dy1, is edge-sharing with five additional monocapped octahedra and two square pyramids and is corner sharing with the apex of two square pyramids and the basal corner of one square pyramid. The second Dy^{3+} octahedron, Dy2, is edge-sharing with *seven* monocapped octahedra and two square pyramids and is corner sharing with the basal corner of one square pyramid. The magnetic properties of this orthorhombic polymorph of Dy_2TiO_5 remains unexplored to this point. One consequence of the differing connectivity for each Dy^{3+} ion creates is the distinct possibility of magnetic moments that can order independently for both Dy1 and Dy2. In this paper we investigate the low temperature crystal structure and magnetic order of orthorhombic Dy_2TiO_5 using a combination of X-ray/neutron diffraction and ac/dc magnetic susceptibility measurements.

Experimental Methodology

Sample Synthesis

Stoichiometric mixtures of Dy_2O_3 and TiO_2 were combined in the following solid-state reaction:

$$Dy_2O_3 + TiO_2 \rightarrow Dy_2TiO_5.$$

Dy_2O_3 was prefired at 1000°C for 8 hours to remove any adsorbed water.

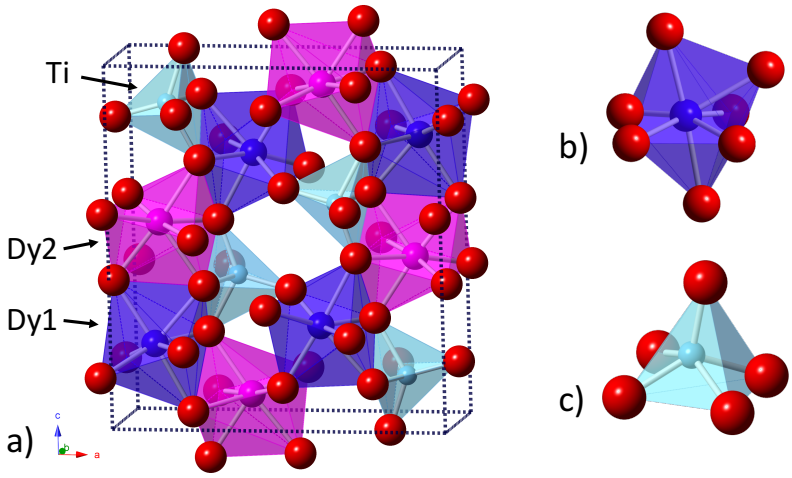

Figure 42: (a) Structure of orthorhombic Dy_2TiO_5 (*Pnma* space group). (b) Dy atoms are in monocapped octahedral coordination (shown as blue and magenta polyhedra for Dy1 and Dy2 respectively). (c) Ti atoms are in square pyramidal coordination.

Powders were ground, mixed using an acetone slurry in a mortar and pestle, and subsequently cold pressed into a pellet using a hydraulic press upon drying. The pellet was then loaded into an alumina crucible and fired at 1200°C for 12 hours. The sample was allowed to cool to room temperature and was then reground, pressed and fired at 1500°C for an additional 12 hours. The heating and cooling rates were kept below 2.5º/minute. The final pellet was ground into a fine powder and checked for purity with X-ray diffraction which revealed no evidence of impurities.

Room Temperature Neutron Diffraction

Structural characterization at 300 K was carried out using neutron diffraction at the NOMAD beamline [89]. Despite the large thermal neutron absorption cross-section there is a window of relatively high transmission extending from about 0.25 Å to 0.7 Å in wavelength and Dy2TiO5 was successfully measured using a small sample size. The sample was first loaded into a 2mm diameter quartz capillary filled to a height of 1 cm and measured for a total of 140 minutes. An identical, empty quartz capillary was also measured for 140 minutes to serve as a background. Rietveld refinement was performed on diffraction patterns from detector bank 5 using the FullProf code [18] to characterize the crystal structure and determine the unit cell parameters and atomic positions within the unit cell. Neutron absorption was accounted for in FullProf through the use of a refinable absorption correction parameter for time-of-flight data with cylindrical geometry.

Low Temperature X-ray and neutron Diffraction

The low temperature X-ray diffraction (XRD) patterns were measured with a HUBER X-ray powder diffractometer. Unit cell parameters were determined by Rietveld refinement using FullProf. All neutron diffraction measurements at 20K and below were performed at the Neutron Powder Diffractometer beamline (HB-2A) at the High Flux Isotope Reactor (HFIR) at Oak Ridge National Laboratory in

Oak Ridge, Tennessee (United States). Custom flat-plate holders with a thickness of 0.15 mm were machined from Aluminum stock to minimize absorption from Dy atoms. A wavelength of 2.4136 Å was selected using a germanium wafer-stack monochromator to provide higher resolution and access to magnetic Bragg peaks at low scattering angles. Data was collected for 5 hours at 0.3 K and 20 K and 4 hours at intermediate temperatures. Rietveld refinement was performed at 20 K (above the magnetic transition temperature) to determine atomic positions and the unit cell parameters of the crystal structure. The magnetic structure was characterized using representational analysis. The magnetic propagation k-vector was determined using the magnetic peaks at 0.3 K with the *k*-search function in Fullprof. Irreducible representations and basis vectors were obtained using the SARA*h* representational analysis code [96].

Magnetic susceptibility measurements

The dc susceptibility measurements were performed using a Quantum Design superconducting quantum interference device (SQUID) magnetometer. The ac susceptibility was measured at the National High Magnetic Field Laboratory with the conventional mutual inductance technique at frequencies between 80 Hz and 700 Hz.

Results & Discussion

Structural Characterization - Neutron Diffraction

The previously reported orthorhombic polymorph characteristic of lanthanide titanates of the Ln_2TiO_5 composition agrees very well with the measured neutron diffraction data of Dy_2TiO_5 at room temperature (Figure 43). The unit cell parameters were determined to be *a* = 10.3722(2), *b* = 3.71985(7), and *c* = 11.2379(2) Å.

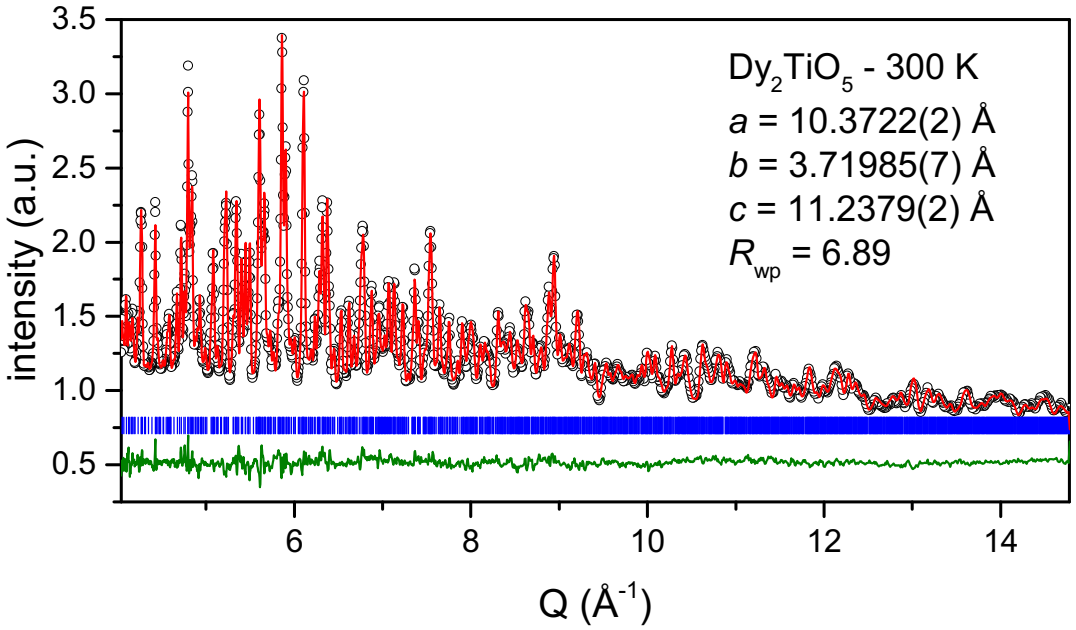

Figure 43: Room temperature neutron diffraction pattern (open circles) of Dy_2TiO_5 refined with the orthorhombic (*Pnma*) structural model (solid red line).

Vertical blue ticks denote Bragg peak positions while the solid green line is the difference between the measured data and structural model.

In general the atom positions agree well with those reported in [132] determined by synchrotron XRD, however the uncertainty is reduced by nearly an order of magnitude for the oxygens likely due to the use of neutrons in the present study (Table 5). The mean Dy-O bond length, <Dy-O>, differs for each Dy site (2.328(1) Å and 2.345(1) Å respectively). Nearest neighbor Dy atoms (Dy1 – Dy2 and Dy2 – Dy2) form two-dimensional "sheets" extending in the [0 1 0] direction (Figure 44a). There is no evidence of a structural transformation or change of *Pnma* space group down to 0.3 K (although additional diffraction peaks emerge at ~1.75 K due to a magnetic transition, discussed below). The unit cell volume contracts by 0.90(5) % and <Dy-O> bond length are reduced to 2.316(2) and 2.320(2) Å for Dy1 and Dy2 respectively (Table 5). Interestingly, Dy2 – Dy2 pairs split and are no longer nearest neighbors. Nearest neighbor Dy atoms (Dy1 – Dy2) now form two-atom "ladders" in the [0 1 0] direction (Figure 44b). The axial positions for the two monocapped octahedra display different temperature dependence. The O1-Dy2-O3 bond angle becomes increasingly distorted at low temperatures while the O1-Dy1-O2 is much more ridged with only minor temperature dependence (Figure 45). At 300 K both the O1-Dy1-O2 and O1-Dy2-O3 bond angles are close 180º (177.4(2) and 174.6(2) respectively). The bond angle significantly decreases for O1-Dy2-O3 as the temperature is lowered while it slightly increases for O1-Dy2-O2.

Structural Characterization - X-ray Diffraction

X-ray diffraction measurements also show no change in *Pnma* space group down to 10 K. The structure does, however, become continuously distorted at low temperatures (Figure 46). The is particularly evident in *b*, which shows negative thermal expansion below 100 K (Figure 46a). This has little effect on the unit cell volume as *b* is only ≈ 1/3rd as large as *a* and *c* which do not show as significant of a distortion (Figure 46b).

Table 5: Refined structural parameters for orthorhombic Dy_2TiO_5 at 300 K and 0.3 K determined by neutron diffraction.

300 K	**a (Å)**	**b (Å)**	**c (Å)**	**V (Å^3)**
Pnma	10.3722(2)	3.71985 (7)	11.2379(2)	433.59(1)

Atom	**x**	**y**	**z**	**B_{iso}**
Dy1	0.11421(13)	0.25	0.22290(11)	0.0056(3)
Dy2	0.13611(13)	0.25	0.55759(13)	0.0062(3)
Ti1	0.1740(6)	0.25	0.8833(7)	0.0081(9)
O1	0.4948(4)	0.25	0.1032(4)	0.0070(6)
O2	0.2255(4)	0.25	0.0433(4)	0.0098(8)
O3	0.2598(4)	0.25	0.7294(4)	0.0069(7)
O4	0.5097(5)	0.25	0.6537(4)	0.0146(10)
O5	0.2659(4)	0.25	0.3833(4)	0.0065(7)

Bond Length (Å)	**O1**	**O2**	**O3**	**O4**	**O5**	**<X-O>**
Dy1	2.314(5)	2.325(5)	2.227(3) ×2	2.391(3) ×2	2.393(5)	2.328(1)
Dy2	2.327(5) 2.359(3) ×2	2.355(3)	2.318(5)	--	2.377(5)	2.345(1)
Ti	--	1.876(9)	1.945(9)	1.754(8)	1.962(2) ×2	1.900(3)

Table 5. Continued.

0.3 K	a (Å)	b (Å)	c (Å)	V (Å^3)
Pnma	10.344(2)	3.7114(8)	11.193(2)	429.74(16)

Atom	x	y	z	B_{iso}
Dy1	0.116(2)	0.25	0.225(1)	--
Dy2	0.143(2)	0.25	0.559(1)	--
Ti1	0.216(7)	0.25	0.854(11)	--
O1	0.500(6)	0.25	0.091(6)	--
O2	0.244(5)	0.25	0.035(6)	--
O3	0.249(7)	0.25	0.741(4)	--
O4	0.485(4)	0.25	0.662(4)	--
O5	0.261(6)	0.25	0.368(5)	--

Bond Length (Å)	O1	O2	O3	O4	O5	<X-O>
Dy1	2.38(7)	2.50(7)	2.33(5) ×2	2.24(3) ×2	2.19(7)	2.316(2)
Dy2	2.24(7) 2.40(5) ×2	2.21(4) ×2	2.31(6)	--	2.47(6)	2.320(2)
Ti	--	2.06(14)	1.31(13)	2.40(10)	1.877(18) ×2	1.90(4)

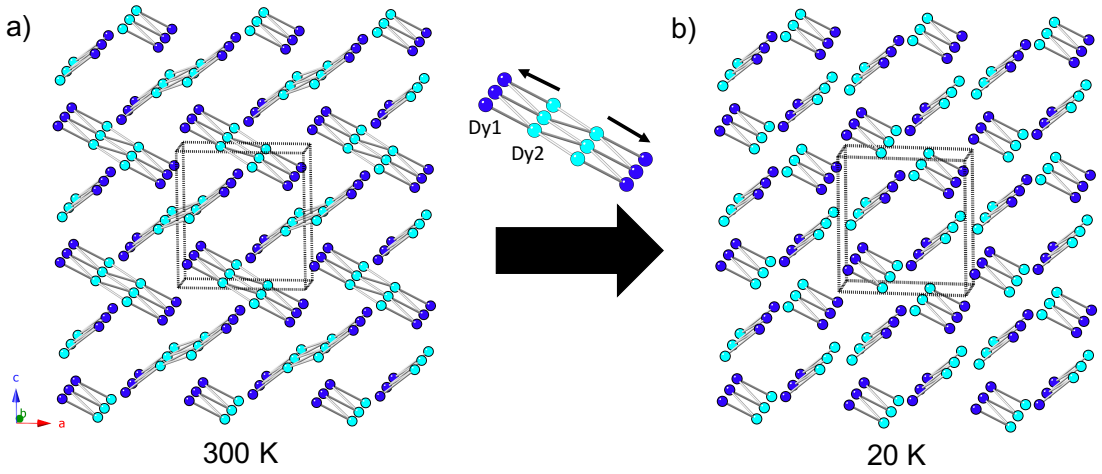

Figure 44: Dy sublattice of Dy_2TiO_5 at (a) 300 K and (b) 20 K.

Dy1 and Dy2 are denoted by dark blue and cyan spheres respectively.

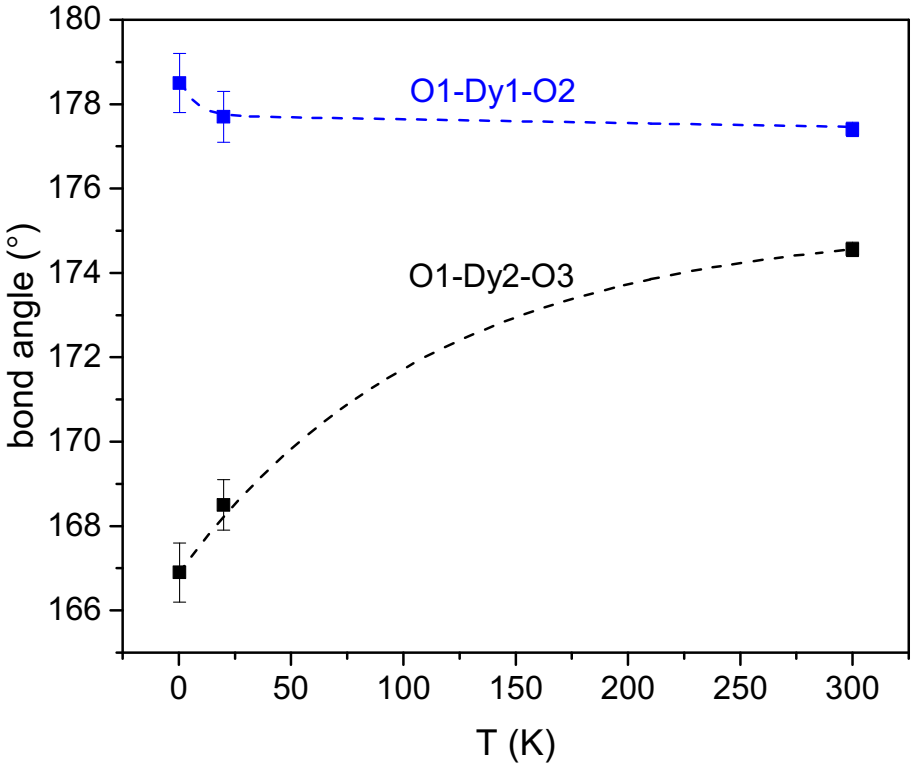

Figure 45: Axial bond angle temperature dependence for Dy1 and Dy2 monocapped octahedra determined by neutron diffraction.

The dashed lines are guides to the eye. Refer to Figure 53 for a detailed explanation of these oxygen positions.

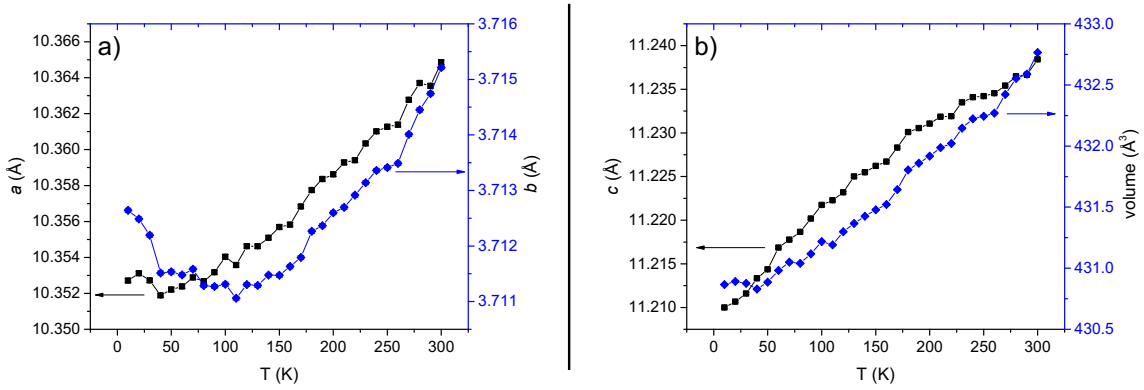

Figure 46: Low temperature XRD patterns.

(a) The "*a*" unit cell parameter (black squares, left axis) indicates only a slight distortion at low temperatures while "*b*" (blue diamonds, right axis) shows a continual *increase* below 100 K. (b) Unlike "*a*" and "*b*", "*c*" (black squares, left axis) continually decreases with temperature. The contraction of the unit cell volume (blue diamonds, right axis) saturates below 40 K.

It does, however, indicate that the Dy “ladders” described in Figure 44b become increasingly stretched along [0 1 0] at low temperatures, which could suppress any spin canting in that direction.

Magnetic Characterization - dc Susceptibility

Magnetic susceptibility measurements indicate an antiferromagnetic transition with a transition temperature of 3.5 K (Figure 47a). There is no divergence in zero-field-cooled (ZFC) and field-cooled (FC) measurements below this temperature (not shown) suggesting the absence of any irreversibility. The susceptibility follows the Curie-Weiss law above 3.5 K indicating paramagnetic behavior. The effective magnetic moment (μ_{eff}) for Dy^{3+} was evaluated to be 10.55 μ_B using the Curie constant, *C*, extracted from the fit to the Curie-Weiss law. This agrees well with the moment for free Dy^{3+} ions which has a value of 10.63 μ_B. The Curie-Weiss temperature (θ_{CW}) was evaluated to be -10.8 K, suggesting antiferromagnetic interactions. Magnetization measurements as a function of increasing field show a saturation far below the effective moment for each Dy^{3+} (Figure 47b). This is indicative of strong anisotropy for Dy^{3+} spins similar to that observed for the cubic $Dy_2(Ti_{2-x}Dy_x)O_{7-x/2}$ and $Ho_2(Ti_{2-x}Ho_x)O_{7-x/2}$ polymorphs [87, 137-139]. Interestingly, magnetization measurements in these previous studies saturate at half (or slightly below) the moment for free Dy^{3+} or Ho^{3+}. The orthorhombic polymorph in the present study, however, saturates at closer to 65% of the moment for free Dy^{3+} suggesting a lowering of anisotropy relative to spin-ice in pyrochlore.

Magnetic Characterization - ac Susceptibility

Zero-field ac magnetic susceptibility measurements also show evidence of a paramagnetic to antiferromagnetic transition beginning at 3.1 K as noted by the sluggish downturn in the real part of magnetic susceptibility, χ’ (Figure 48a). There exists only weak frequency dependence suggesting the absence of glass/ice-like dynamics. The magnetic structure is, however, strongly field dependent. There are two peaks in the field scan performed at 0.3 K (Figure 48b).

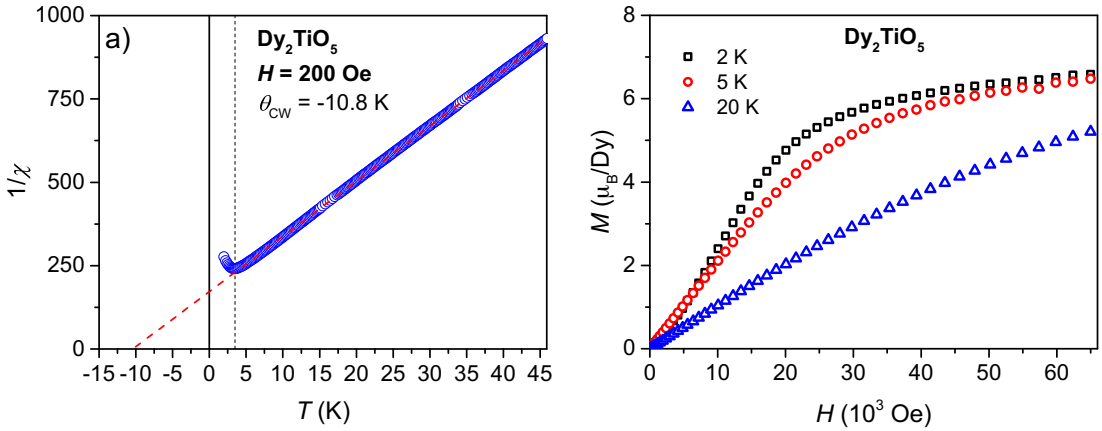

Figure 47: dc magnetic susceptibility and magnetization measurements of Dy_2TiO_5.

Inverse susceptibility (a) reveals an antiferromagnetic transition at 3.5 K (vertical dashed line) with paramagnetic behavior above this temperature. The Curie-Weiss law was fit to the data (dashed red line) resulting in a Curie-Weiss temperature (θ_{CW}) of -10.8 K. Magnetization measurements (b) at varying temperatures show a saturation below the moment for free Dy^{3+} ions but larger than that observed in spin-ice or cubic Dy_2TiO_5 polymorphs.

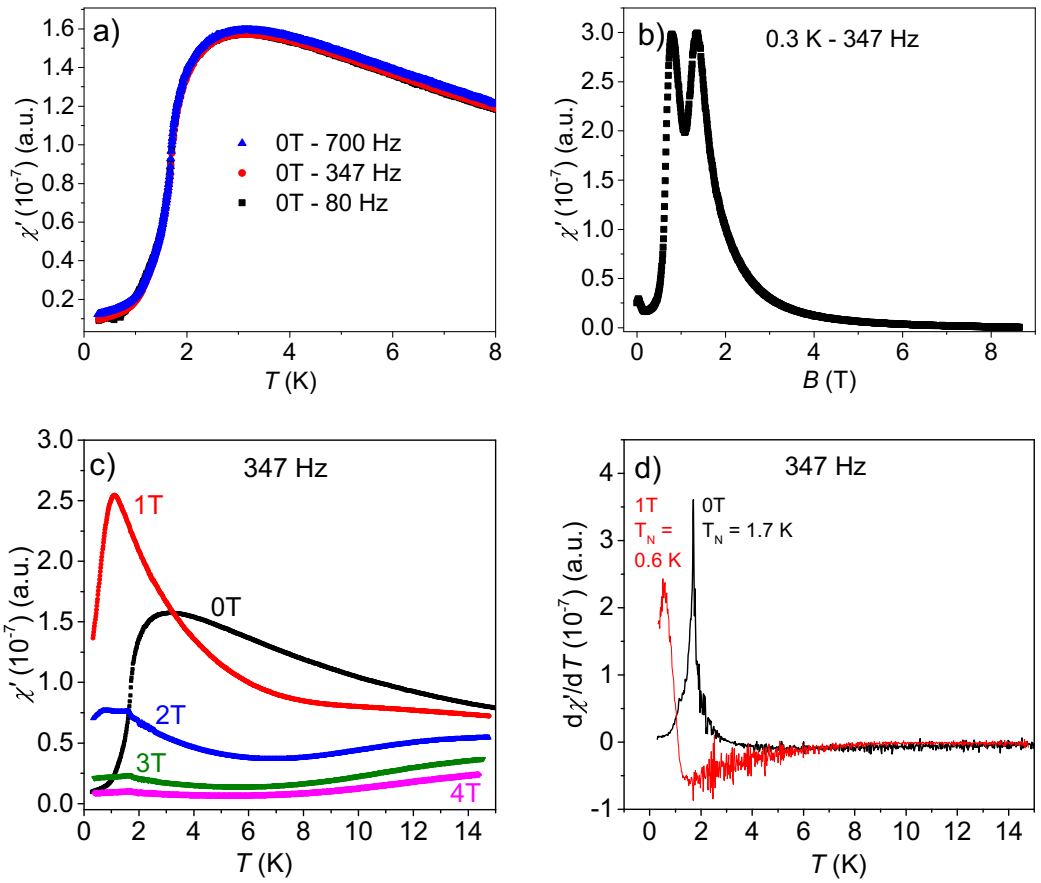

Figure 48: ac magnetic susceptibility measurements of powder Dy_2TiO_5.

(a) Real part of zero field ac magnetic susceptibility at 700 Hz, 347 Hz, and 80 Hz. (b) Magnetic field sweep at 0.3 K with a frequency of 347 Hz. There are two maxima of equal intensity at 0.79 T and 1.35 T. (c) Real part of magnetic susceptibility from B = 0 – 4 T. (d) 1st derivative of the real part of magnetic susceptibility for B = 0 T and 1 T.

Each of the moments on both Dy^{3+} atoms (Dy1 and Dy2 discussed earlier) are likely polarized by the magnetic field independently as the magnitude of the two peaks in the field scan is identical. Cooling in the presence of a 1 T magnetic field slightly sharpens the transition and lowers the maximum to 1.1 K (Figure 48c). A 2 T magnetic field suppressed susceptibility and further lowers the maximum to 0.8 K. Larger fields completely dampen the magnetic transition. There is a small kink at 1.6 K which is first apparent in the 2 T measurement. This is an artifact due to He^3 condensation as the position is invariant at stronger magnetic fields.

A peak in susceptibility is commonly assigned to the onset of long-range order. However, there is an observable inflection in χ' below the maximum at 3.1 K for the zero field measurements of Dy_2TiO_5 in Figure 48a and Figure 48c. This is most apparent when looking at $d\chi'/dT$ as sharp peaks are evident at 1.7 K and 0.6 K for 0 and 1 T measurements respectively (Figure 48d). The rapid increase in $d\chi'/dT$ at ~3 K corresponds to the maximum observed in χ'. In general, 3D antiferromagnetic ordering can be better predicted by a peak in the first derivative of χ' [140] suggesting that zero-field 3D long range ordering begins at 1.7 K.This possibly implies a shift in the dimensionality of magnetic order (*i.e.* a 2D-3D transition) with $T_{N,2D}$ = 3.1 K and $T_{N,3D}$ = 1.7 K. Low temperature neutron diffraction provides more insight into the dimensionality of the spin structure.

Magnetic Characterization - Neutron Diffraction

A magnetic transition is confirmed with neutron diffraction experiments (Figure 49a). Comparing the background of the diffraction patterns taken at 20 K and 3K reveals the onset of local magnetic ordering as noted by the appearance of a broad, diffuse peak centered at $2\theta \approx 22.5^{\circ}$. Strong resolution limited Bragg peaks are apparent at 0.3K. These peaks can be indexed with a propagation vector k = [0 ½ 0]. The diffuse peak at 3 K and the (100) magnetic peak at 0.3 K are centered at the same scattering angle but with a different peak shape (Figure 49b). To test the lower dimensionality suggested by susceptibility measurements, the

diffuse peak was fit with a Warren function characteristic of 2D magnetic ordering [141-144]:

$$\boldsymbol{P(\theta) = KmF_{hk}^2 \frac{(1+cos^2 2\theta)}{2(sin\theta)^{\frac{3}{2}}} \left(\frac{\xi}{\lambda\sqrt{\pi}}\right)^{\frac{1}{2}} F(a)} \quad (24)$$

where

$$\boldsymbol{F(a) = \int_0^{20} exp[-(x^2 - a)^2]dx} \quad (25)$$

and

$$\boldsymbol{a = \frac{2\xi\sqrt{\pi}}{\lambda}(sin\theta - sin\theta_0)} \quad (26)$$

in which K represents a scale factor, m the multiplicity of reflection, F_{hk}^2 the magnetic structure factor, ξ the spin-spin correlation length, and θ_0 the centroid of the diffuse peak. The integral in $F(a)$ was evaluated numerically and agrees with values reported in ref. [141]. The Warren function fits the diffuse peak well with $\xi \approx 22$ Å (Figure 50). This agrees with the susceptibility measurements and is strongly suggestive of low dimensionality ordering. A simple linear background was included in the fitting procedure consistent with ref. [144].

Although local ordering begins at 3K, a long range magnetic transition (T_N) is not apparent until 1.7 K as noted by the temperature dependence of the (100) magnetic peak intensity (Figure 49b inset) explaining the sluggish transition observed in susceptibility (Figure 48a) and the sharp maximum observed in the 1st derivative curve (Figure 48d). This also suggests that Dy_2TiO_5 is only moderately frustrated, as the frustration parameter, f, (defined as $|\theta_{CW}|/T_N$) is equal to 6.4.

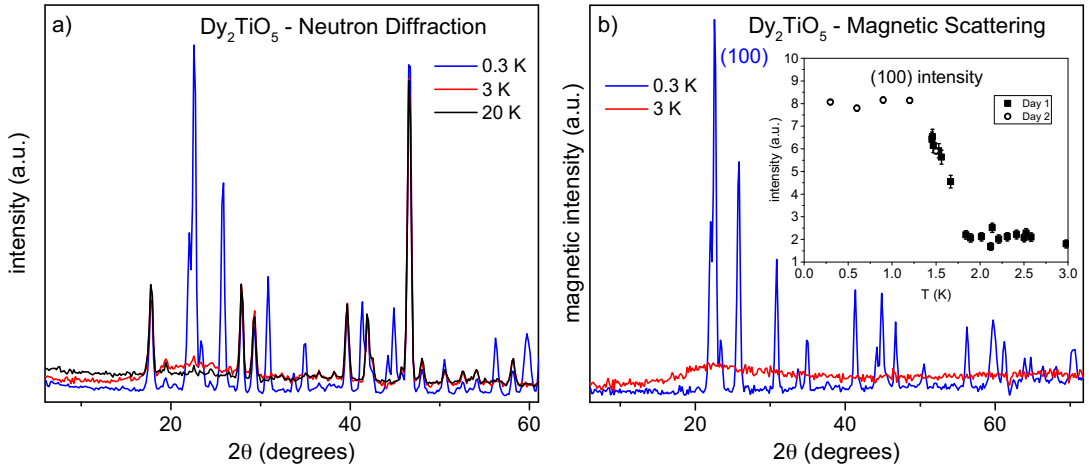

Figure 49: Low temperature neutron scattering patterns.

(a) Neutron diffraction patterns at 0.3 K, 3 K, and 20 K. (b) Magnetic contributions only at 0.3 K and 3 K obtained by subtracting the pattern at 20 K. Only diffuse magnetic scattering is observed at 3 K while long range magnetic order begins around 1.7 K (inset). Solid squares and open circles were measured on separate days.

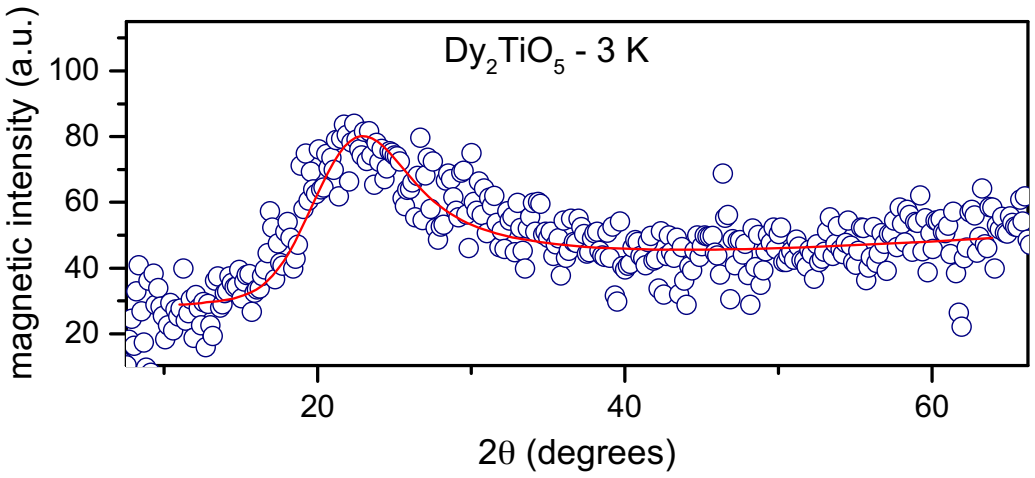

Figure 50: Fit of the diffuse magnetic scattering at 3 K using the Warren function.

Each Dy atom occupies a 4*c* Wyckoff site within the *Pnma* symmetry creating 4 equivalent positions for each Dy atom (translations are shown below).

$$\begin{aligned}
&\text{atom 1:} && x, y, z \\
&\text{atom 2:} && x+\frac{1}{2}, -y+\frac{1}{2}, -z+\frac{1}{2} \\
&\text{atom 3:} && -x+1, y+\frac{1}{2}, -z+\frac{1}{2} \\
&\text{atom 4} && : -x+\frac{1}{2}, -y+1, z+\frac{1}{2}
\end{aligned}$$

There exist two equivalent irreducible representations (IRs) each with 12 basis vectors (ψ_n). One IR was ultimately chosen for magnetic characterization. The magnetic state is therefore described by a linear combination of 12 basis vectors (6 basis vectors each for Dy1 and Dy2, shown in Table 6). The coefficients on ψ_1 must necessarily have opposite signs for Dy1 and Dy2 or else there are prominent forbidden reflections at 2θ = 18.7, 33.1, 42.5 and 54.9 among other minor reflections. This also applies to the coefficients for ψ_4. Conversely, the coefficients on ψ_2 for Dy1 and Dy2 must necessarily have the *same* sign to eliminate forbidden reflections at 2θ = 52.5 and 66.2. An analogous relationship holds for ψ_5. The coefficients on ψ_3 must also be of opposite signs for Dy1 and Dy2 to remove forbidden reflection at 2θ = 33.1, 42.5 and 52.5 among others which also applies to ψ_6. There remain, however, low intensity forbidden reflections indicating that any moment canting in the [0 1 0] direction is unlikely and this component was fixed at zero. This agrees with the negative thermal expansion observed in Figure 46a in which Dy atoms become increasingly separating along *b* at low temperatures. Assuming that C_n is equal for both Dy1 and Dy2 atoms despite them occupying crystallographically independent sites produces a reasonable fit to the experimental data (R_{WP} = 18.3, see Table 7).

Table 6: Symmetrically allowed basis vectors (BV) for the Γ_2 IR for the *Pnma* space group with a k = [0 ½ 0] propagation vector.

	Atom 1			Atom 2				Atom 3			Atom 4		
BV	m_x	m_y	m_z	m_x	m_y	m_z	BV	m_x	m_y	m_z	m_x	m_y	m_z
ψ_1	2	0	0	2	0	0	ψ_3	0	2	0	0	2	0
ψ_2	0	0	2	0	0	2	ψ_4	2	0	0	2	0	0
ψ_6	0	2	0	0	2	0	ψ_5	0	0	2	0	0	2

Table 7: Refined coefficients for magnetic basis vectors.

C_n refers to the coefficient on ψ_n described in Table 6. Data was collected at 0.3 K at the Hb-2a beamline of the High Flux Isotope Reactor. The refinement is improved if coefficients on Dy1 and Dy2 are independently refined.

Same Moments (R_{WP} = 18.3)

Atom	C_1	C_2	C_3	C_4	C_5	C_6	μ
Dy1	2.61(6)	-3.06(6)	0	-2.61(6)	3.06(6)	0	8.05(12)
Dy2	-2.61(6)	-3.06(6)	0	2.61(6)	3.06(6)	0	8.05(12)

Different Moments (R_{WP} = 13.9)

Atom	C_1	C_2	C_3	C_4	C_5	C_6	μ
Dy1	2.35(15)	-3.78(13)	0	-2.35(15)	3.78(13)	0	8.89(28)
Dy2	-3.00(17)	-2.46(12)	0	3.00(17)	2.46(12)	0	7.76(31)

The calculated moment is 8.05(12) μ_B which is reasonable but still less than the ordered moment of 10 μ_B for free Dy^{3+} ions suggesting that moments are not fully saturated even at 0.3 K or are dampened by crystal field effects. The fit is significantly improved by removing the constraint that moments be equal for Dy1 and Dy2 atoms (R_{WP} = 13.8, Figure 51). This results in a magnetic moment of 8.89(28) μ_B and 7.76(31) μ_B for Dy1 and Dy2 respectively (Table 7).

The spin directions within the magnetic structure in both scenarios follows the underlying interwoven 2D "sheets" created by the Dy ions (Figure 52). This likely confirms the 2D-3D magnetic transition postulated earlier. At 3K moments order on 2D ladders created by nearest neighbor Dy1-Dy2 pairs only (Figure 44b and grey lines in Figure 52) but do not interact with other pairs on longer length scales. Beginning at 1.7 K locally ordered moments on these ladders interact with neighboring Dy1-Dy2 pairs forming the interwoven structure shown in Figure 52. It should be noted that there is an additional magnetic peak at 2θ = 23.9º that cannot be indexed with the *k* = [0 ½ 0] propagation vector and either requires a larger unit cell, is suggestive of an incommensurate magnetic structure or is due to an unidentified low temperature phase within the measured sample.

The refined Dy1 moments always point along the O1-Dy1-O2 bond angle (Figure 53), which is nearly 180º (178.5(7)º). This is indicative of a local Ising axis explaining the anisotropy observed in the magnetization measurements discussed earlier. Dy2, however, does not possess such an "easy axis". O1, O3, and O5 all reside within a (0 1 0) plane, however none make a 180º bond angle with Dy2. The O1-Dy2-O3 bond angle is 167.2(7)º, while O5 is an octahedral monocap without an equivalent oxygen in line with Dy2. The Dy2 moments order nearly along the O1-Dy2-O3 bond angle but are canted slightly toward O5. It should be noted that the angle between O4-Dy2-O5 is close to 180º (177.9(6)º) and nearly parallel to O1-Dy1-O2 which could provide a local Ising axis, however, the Dy2-O4 spacing (3.5243(6) Å) is far beyond the ionic radius of Dy^{3+}.

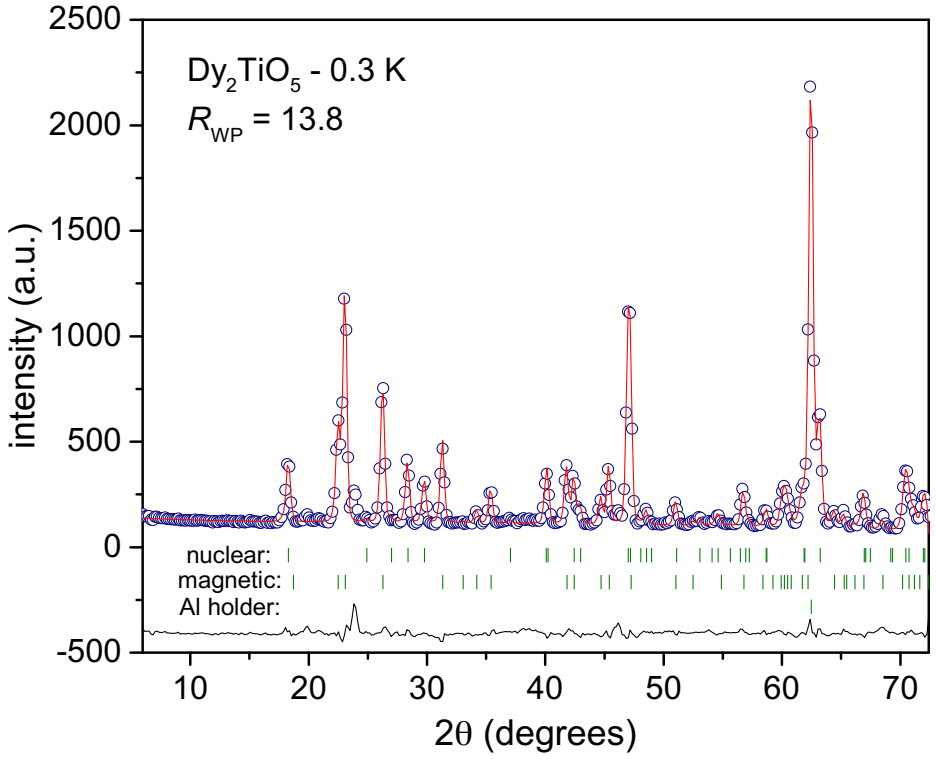

Figure 51: Magnetic neutron refinement at 0.3 K.

The refinement (solid red line) agrees well with the measured data (open circles). The nuclear structure, magnetic structure, and Al holder were all refined together. Refined Bragg peaks from each phase are shown as vertical green ticks. The solid black line represents the difference between the measured data and refinement. There exists an additional magnetic peak at 23.8º that cannot be indexed with the k = [0 ½ 0] propagation vector and requires a larger unit cell.

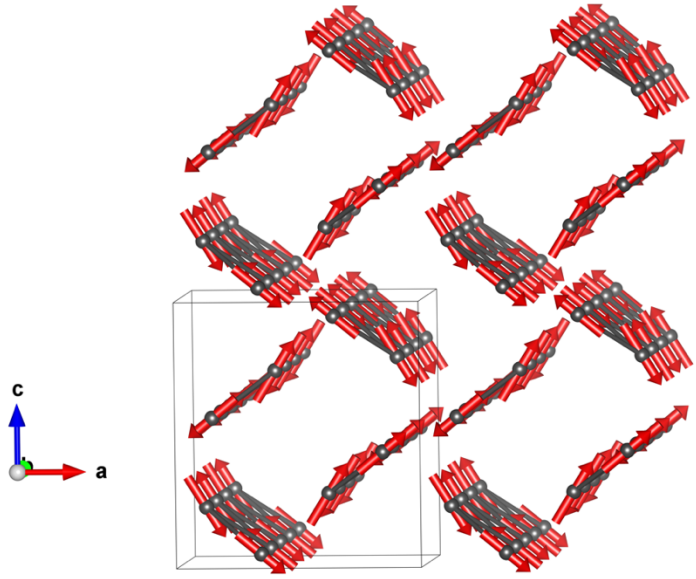

Figure 52: Refined magnetic structure of Dy_2TiO_5.

Dy atoms are shown as grey spheres while magnetic moments are shown as red arrows. Solid gray lines designate nearest neighbor Dy pairs. Ordered moments encircle nonmagnetic Ti^{4+} cations (not shown).

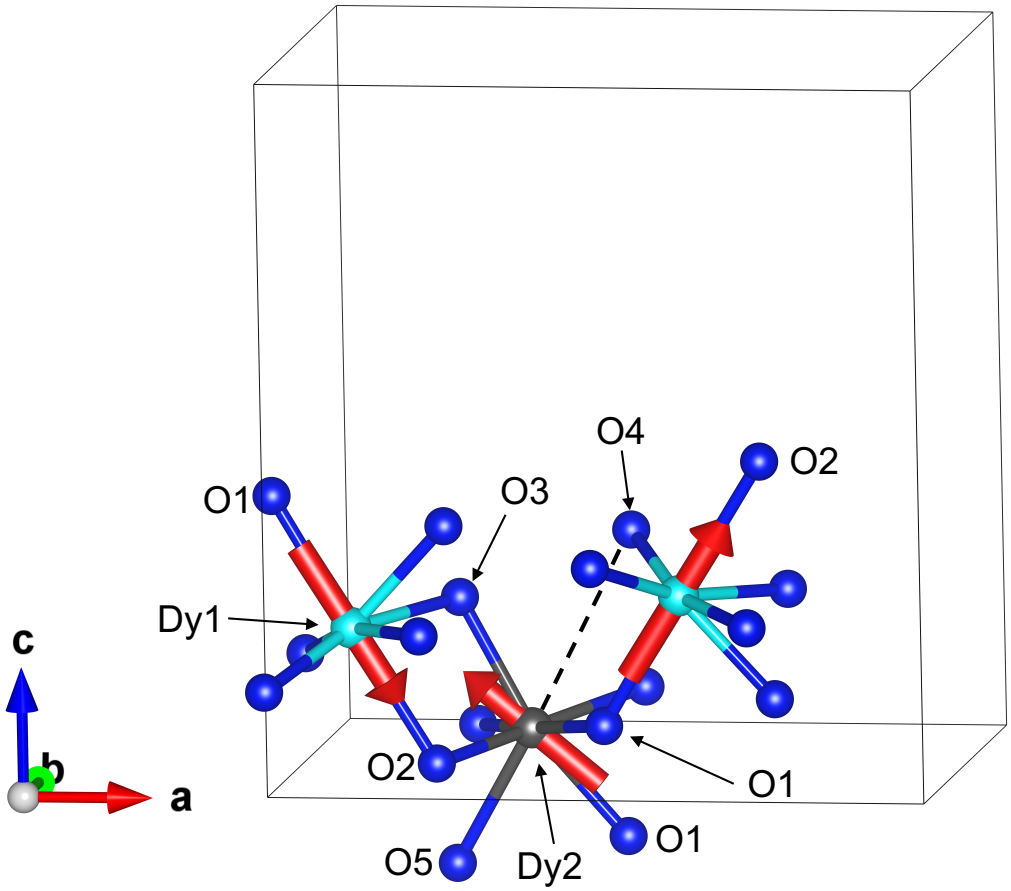

Figure 53: Relation between refined magnetic moments and oxygen coordination for Dy1 and Dy2 at 0.3 K.

Magnetic moments on Dy1 atoms (cyan spheres) order along the 180º angle formed by O1-Dy1-O2 which corresponds to a local Ising axis. Dy2 (black sphere) does not possess such a crystal field and the moment is ordered between the O1-Dy2-O3 and O1-Dy2-O5 bond angles. O5-Dy2-O4 does form a 180º angle that is nearly parallel to O1-Dy1-O2, however, the Dy2-O4 distance (shown as a dashed line) is far beyond the ionic radius of Dy^{3+}.

This axis would also be forbidden by the restrictions set on the basis vectors earlier as Dy1 and Dy2 must have opposite signs for ψ_1 and same signs for ψ_2. These cannot be simultaneously fulfilled for this direction. Thus, Dy2 moments do not order in a particular direction with strong uniaxial symmetry as required for Ising-like ordering.

This is consistent with the observed dc magnetization measurements. The anisotropic Dy1 spins lower the magnetization saturation point much like Dy spins in $Dy_2Ti_2O_7$ spin ice (approximately ½ of the free Dy^{3+} moment). The more isotropic Dy2 spins, however, raise the saturation relative to spin-ice pyrochlores (and cubic A_2TiO_5 polymorphs) resulting in a bulk saturation that is in between spin-ice and free Dy^{3+}. The distinct ordering and anisotropies for Dy1 and Dy2 potentially explains the double peak in the magnetic field scan at 0.3K (Figure 48b). In general, a sharp peak is indicative of a spin-flip transition. The double peak therefore indicates two successive spin-flip transitions. Since there are two unique Dy ions the most likely cause of this is that one peak corresponds to Dy1 and the other Dy2. The difference in the applied fields for the peaks therefore reflects the different energy scales of the magnetic exchange interactions for the Dy1 and Dy2. The origin of this in the lattice, as discussed, is the different crystal field and bond angles that lead to more Ising-like interactions for one Dy and less for the other. To assign the observed peaks we note that, in general, Ising transitions are typically sharper than non-Ising (Heisenberg) transitions. The first peak in Figure 48b at 0.79 T, which is slightly more narrow than the second peak at 1.35 T, could therefore correspond to Ising-like Dy1 spin flips. This assignment is further supported by examining the number of next nearest neighbors available for exchange interactions. As shown in Figure 44 and Figure 52, Dy atoms are ordered in “sheets” extending infinitely in the [010] direction. Dy1 atoms form the edges of the “sheet” while Dy2 atoms are on the interior (Dy1-Dy2-Dy2-Dy1). Dy2 has four next nearest neighbors that are approximately equidistant: two in the [010]

direction and two that were originally nearest neighbors at 300 K (Figure 44a). Dy1 atoms, however, only have the two next nearest neighbors in the [010] direction because they are not interior atoms. If Dy2 moments were to flip first (at 0.79 T), Dy1 spins would be isolated and rely solely on Dy1-Dy1 coupling in the [010] direction to remain ordered. If Dy1 atoms flipped first, however, Dy2 could still maintain order (with itself) within the “sheet”. Unless the Dy1-Dy1 coupling strength is very strong, the peaks at 0.79 T and 1.35 T can reasonably be attributed to flipping/polarizing Dy1 and Dy2 spins respectively. We note, however, that this is a complex problem and without the availability of a single crystal, there is not sufficient data to definitively determine the origin of the double peak since there are many interactions involved (*i.e.*, nearest neighbor and next nearest neighbor exchange, spin anisotropy, long-range dipolar interactions).

CHAPTER V

INCREASED IONIC CONDUCTIVITY IN $Gd_2Ti_2O_7$ AMORPHIZED BY SWIFT HEAVY ION IRRADIATION

Abstract

It has previously been suggested that ion irradiation can be used to improve the ionic conductivity in pyrochlore-type oxides. Sample quantities from irradiation experiments with MeV ions, however, are typically far too small to produce sufficiently large sample quantities for accurate measurements of macroscopic properties such as ionic conductivity. Here we present a novel experiment utilizing the SIS heavy-ion synchrotron in Darmstadt, Germany to irradiate macroscopic quantities of $Gd_2Ti_2O_7$ suitable for electrochemical characterization. Electrical properties of Gd_2TiO_7 amorphized by irradiation with 150 MeV/u Au ions were measured using broadband dielectric spectroscopy as a function of increasing and decreasing temperature. Dramatic changes to ionic conductivity have been observed after irradiation with a 250-fold increase compared to the corresponding unirradiated pyrochlore sample. Two abrupt decreases in conductivity were observed at 440 ºC and 720 ºC when the sample was heated within a dry nitrogen atmosphere. The critical temperature associated with these transitions was dependent on the sample atmosphere and showed an increase to 575 ºC and 800 ºC respectively when the measurements were performed in air. Based on complementary XRD and Raman spectroscopy experiments, it can be concluded that the first transition (400 ºC and 575 ºC) is caused by a decrease in charge carrier concentration related to short range reordering of the oxygen-sublattice, and the second transition (720 ºC and 800 ºC) is due to a decrease in charge mobility as a result of recrystallization of the amorphous phase.

Experimental Methodology

$Gd_2Zr_2O_7$ and $Gd_2Ti_2O_7$ samples were prepared as dense pellets (1 cm diameter) by the solid-state reaction method from constituent oxides. The samples were then thinned down to 400 and 300 μm (for $Gd_2Zr_2O_7$ and $Gd_2Ti_2O_7$ respectively) and polished to a mirror finish using diamond lapping film. Swift heavy ion irradiation was performed at the heavy-ion synchrotron (SIS) of the GSI

Helmholtz Center for Heavy Ion Research using 150 MeV/u Au ions (29 GeV). $Gd_2Zr_2O_7$ and $Gd_2Ti_2O_7$ pellets were irradiated together as a stack to an ion fluence of 4×10^{12} ions/cm^2. The mean energy loss across the $Gd_2Zr_2O_7$ sample was 14.1(4) keV/nm while for $Gd_2Ti_2O_7$ it was 15.7(6) keV/nm. The beam spot was a 1 cm x 1 cm square and covered the entire stack. $Gd_2Zr_2O_7$ is not the focus of this work and is only mentioned for repeatability. $Gd_2Ti_2O_7$ was broken into 4 pieces for experimental characterization.

Complex conductivity and dielectric properties were assessed using a Novocontrol Alpha A analyzer and ProboStat dielectric sample cell. High purity platinum cylinders (American Elements 99+%, 3 mm diameter × 3 mm height) were used as the top and bottom electrodes. The electrodes were aligned and connected to platinum leads using a stacked series of alumina disks with three alumina alignment rods (Figure 54). Complex conductivity and permittivity was calculated from the measured current using WinDeta software. A grounded, metal shield (NorEcs) was used to filter out unwanted ambient electromagnetic signal from the dielectric spectra. Unfortunately, this was not available when measurements were performed in air, and only the low frequency region of the dielectric spectra could be analyzed (DC conductivity).

Samples were then annealed at 200 ºC for 24 hours to remove any adsorbed water which could affect the dielectric properties. The samples were continuously measured during the heating to ensure that the complex conductivity and permittivity were no longer changing as a function of time by the end of the 12 hours. The samples were then measured from 400 ºC to 1200 ºC in 10 ºC increments for dry nitrogen and 25 ºC steps for air and were again measured back down to 400 ºC using the same temperature steps. The ramp from one temperature to the next took approximately 25 minutes depending on the temperature. The measurement started once the sample temperature stabilized to less than 0.5 ºC/min. Each measurement consisted of 63 frequencies ranging from 1×10^{7} Hz to 1×10^{-2} Hz which took 30 minutes to complete.

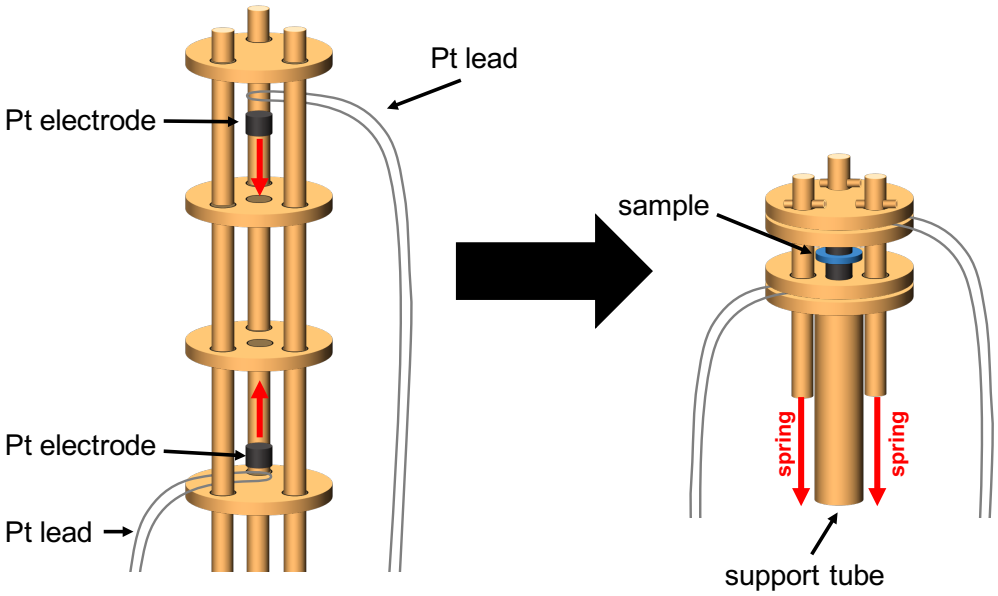

Figure 54: Sample cell for impedance spectroscopy measurements.

The time between subsequent measurements at the same frequency was approximately 1 hour which is typically considered long enough for any defects to anneal in irradiated materials. All measurements were completed in an ultra-high purity dry nitrogen atmosphere.

Complementary to broadband dielectric spectroscopy measurements, irradiated and unirradiated $Gd_2Ti_2O_7$ samples were analyzed by means of synchrotron X-ray diffraction (XRD) and Raman spectroscopy (including annealing experiments). A small amount of powder was scratched off of unheated pristine and irradiated $Gd_2Ti_2O_7$ pellet fragments and was subsequently pressed into separate 100 μm diameter holes drilled into molybdenum foil with a thickness of 25 μm (explained in detail in [102]) for X-ray diffraction measurements. Synchrotron X-ray diffraction was performed at the 16-BM-D beamline (HPCAT) at the Advanced Photon Source in Argonne, Illinois. The beam energy was 29.2 keV and the samples were measured in transmission mode. The diffraction rings were recorded using a MAR CCD detector. The two-dimensional MAR images were processed into one-dimensional X-ray diffraction patterns using the Dioptas software [145].

Because Gadolinium is a strong neutron absorber, Raman spectroscopy was employed to obtain information on the irradiation induced modifications to the local structure of $Gd_2Ti_2O_7$ rather than neutron total scattering which has been central to this dissertation. Raman spectra were recorded using a LabRAM HR Evolution Raman spectrometer from Horiba Scientific with a 50 mW, 532 nm laser source. The diffraction grating was set to 1800 gr/mm and the spectral resolution was approximately 0.01 nm. A small piece of the sample pellet was measured before and after heating to temperatures of up to 900 ºC using 300 ºC steps. The sample was heated to the desired temperature in a box furnace in air with a ramp rate of 45 ºC/minute, held for 30 minutes, then cooled down naturally to room temperature before each Raman spectroscopy measurement. All spectra were

independently recorded three times for 30 seconds each. The final spectra for each sample was obtained by averaging the three measurements.

Results and Discussion

Radiation-induced amorphization in $Gd_2Ti_2O_7$ irradiated to 4×10^{12} ions/cm^2 is evident in the XRD patterns by the disappearance of Bragg reflections and the emergence of diffuse scattering bands centered at Q ≈ 2.1 Å^{-1}, 3.5 Å^{-1}, and 5.4 Å^{-1} (Figure 55). There remains a miniscule fraction of crystallinity as evidenced by the small Bragg peaks at Q ≈ 2.8 Å^{-1}, 3.5 Å^{-1}, and 4 Å^{-1}. However, the intensity of the remaining Bragg peaks is so small that it can be reasonably said that any dielectric properties measured arise primarily from the amorphous phase (until defects anneal at high temperatures).

Conductivity and charge carrier dynamics in irradiated $Gd_2Ti_2O_7$ were assessed using the real part of complex conductivity (σ') and the real part of the complex dielectric permittivity (ϵ'). In general, the DC conductivity (σ_{DC}) corresponds to a plateau in σ' that is invariant with frequency. This plateau is often not apparent due to due to interfacial (grain boundaries) and electrode polarization effects and σ_{DC} must be estimated or assessed by fitting models to the spectra. However, for irradiated $Gd_2Ti_2O_7$, the plateau is clearly visible and the DC conductivity can be reasonably assessed at a frequency of 10 Hz for the entire temperature range (Figure 56). When plotted to scale, the spectra at intermediate temperatures is complex with multiple relaxation processes within the frequency range studied (discussed later). The increase in σ_{DC} with temperature, however, is very large and the small kinks in the each spectrum do not significantly affect the estimation of σ_{DC} when compared with other temperatures.

There are two abrupt decreases in σ_{DC} for measurements with increasing temperature in nitrogen at 440 ºC and 720 ºC, respectively (Figure 57). The two discontinuities in σ_{DC} are consistently observed when measured in air, but they are increased to 575 ºC and 800 ºC.

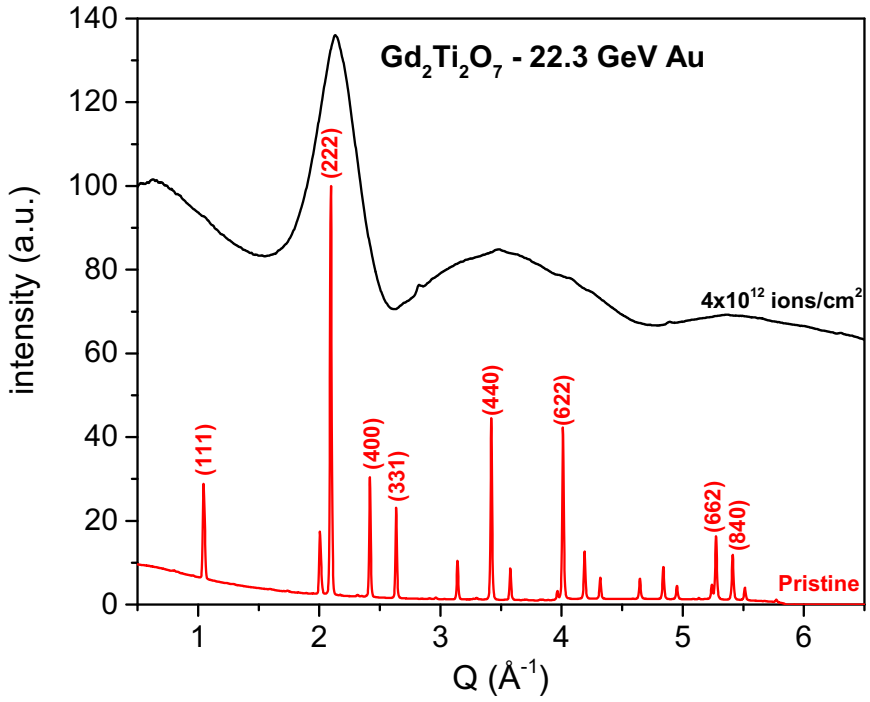

Figure 55: Synchrotron XRD pattern of $Gd_2Ti_2O_7$ before (red) and after (black) irradiation.

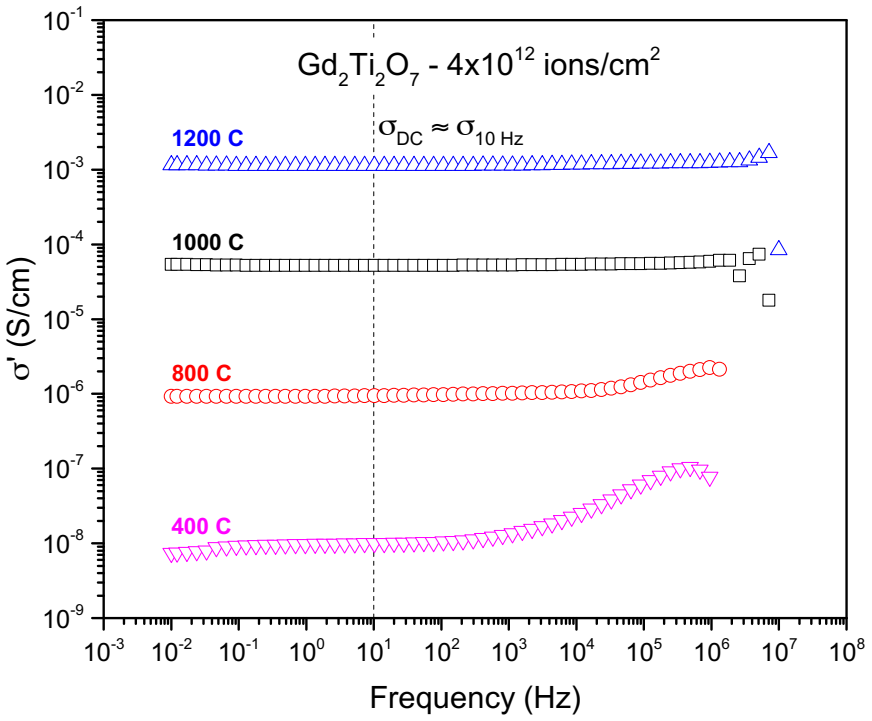

Figure 56: DC conductivity was approximated at 10 Hz for all spectra (dashed line).

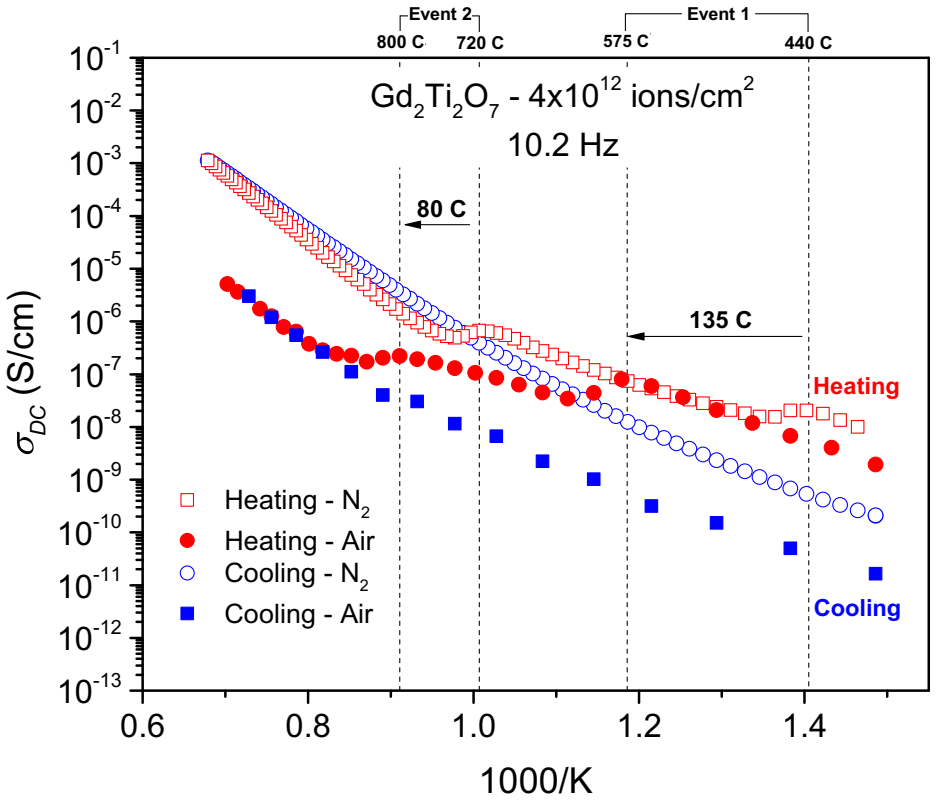

Figure 57: DC conductivity measurements as a function of temperature during heating (red) and cooling (blue) in air (solid) and nitrogen (open).

From this point on, these two discontinuities (440 ºC (N_2), 575 ºC (air) and 720 ºC (N_2), 800 ºC (air)) are referred to as Event 1 and Event 2 respectively. Event 2 in air at 800 ºC is in agreement to the onset of recrystallization of amorphous $Gd_2Ti_2O_7$ as demonstrated in a previous ion-beam study using similar radiation conditions (2 GeV ^{181}Ta ions) [146]. The onset of recrystallization was reported at 750 ºC and completed at 800 ºC. No changes in the XRD patterns were apparent at annealing temperatures below 750 ºC. Taking into account the annealing results of [143] and the dielectric measurements of the present study, it can be concluded that the conductivity in the amorphous phase is higher than in the crystalline phase. This is further supported by calorimetry measurements on $Gd_2Ti_2O_7$ disordered through mechanical milling [147, 148]. Depending on the post milling temperature treatment, a sharp exothermic event was observed anywhere between 780 ºC and 822 ºC that was associated with the reordering of defects on both the anion and cation sublattice [148]. Interestingly, these authors reported an additional much broader exothermic event at higher temperatures, which was related to an increase in grain size. There was no observed effect in conductivity in this higher temperature regime (> 800 ºC) in the present study. This is not surprising as the mean crystallite diameter of the mechanically milled samples (before temperature treatment) was on the order of 10 nm which is much smaller than the grain size of the pyrochlore sample of the present study which was on the order of 1 μm.

The conductivity measured in dry nitrogen is larger than in air when comparing identical temperature regimes in the present pyrochlore sample This reflects the mixed electronic/ionic nature of conduction for $Gd_2Ti_2O_7$. The total measured conductivity can simply be represented by Eq. (2) which is simply the sum of ionic, n-type, and p-type conductivity. While it may seem counterintuitive, it has been well established that ionic contribution in pyrochlores (and most fluorite-related oxides) is invariant of the oxygen partial pressure, pO_2, in the sample environment (see Ionic Conductivity section on page 15) [21, 22, 73-75, 80]. For mixed conductors, lowering pO_2 increases the n-type (electron) conduction while

raising pO_2 increases p-type (hole) conduction. Both calculations and experiments have shown that n-type conduction is dominant in undoped $Gd_2Ti_2O_7$ and p-type conduction is not significant until pO_2 is larger than 1 atm [80, 149]. Thus, the increased total conductivity when measured in N_2 relative to air is caused by n-type conduction.

For both atmospheres, the conductivity measured before Event 1 on heating is much larger than the conductivity measured at the same temperature on cooling. Assuming the majority of defects have been annealed at 1200 ºC (which is supported by refs. [146] and [148]), the cooling curve is comparable to an unirradiated sample which is dominated completely by n-type conductivity rather than ionic or p-type conductivity. The maximum increase (before Event 1) between the heating and cooling measurements is about 250 fold when measured in air and only 50 fold when measured in N_2. If the increased conductivity in the amorphous phase was solely due to increased electronic conduction, the relative increase when measured on heating compared with cooling should be invariant of the atmosphere; it should always follow a $pO_2^{-1/4}$ dependence at any given temperature in accordance with Eq. (6). The conductivity of cooling curve (which is analogous to pristine $Gd_2Ti_2O_7$, an n-type semiconductor) increases dramatically in N_2 (low pO_2). The heating curve (before Event 1 and 2), however, shows much less dependence on the atmosphere than the cooling curve. It can therefore be concluded that this radiation-induced increase in conductivity (heating compared with cooling) is largely attributed to ionic conduction within the amorphous phase rather than increased electronic conductivity.

Conductivity is equally affected by both the concentration of charge carriers, n or $[V_O^{\cdot\cdot}]$, as well as the mobility, μ, of the charge carriers:

$$\boldsymbol{\sigma_{DC} = nZe\mu} \tag{27}$$

where Z and e are the number of charges per carrier and electron charge respectively. Frequency dependent models of the real part of permittivity, ϵ', and real part of conductivity, σ', were used to investigate the origin of the increased conductivity (charge carrier concentration *vs.* charge carrier mobility). This was first performed at 440 ºC on heating and on cooling which is before Event 1 and 2. This analysis was only performed for measurements in N_2 for reasons described earlier.

In accordance with Maxwell's equations, the complex permittivity is essentially a measure of how easily an external electric field can penetrate a medium. Dielectric relaxation processes (*i.e.*, time-dependent polarizations) and charge transport therefore have a strong effect on the permittivity. In general, a dielectric relaxation/polarization process is reflected in ϵ' as a step-like increase in ϵ' with decreasing frequency or as a peak in ϵ''. Irradiated $Gd_2Ti_2O_7$ shows a single process at 440 ºC when heating and possibly two processes (denoted as asterisks) when cooling (Figure 58a). Several models have been developed to characterize this frequency response, the most general being the Havriliak/Negami function (HN-function) [150], which was fit to the data on heating to obtain a characteristic relaxation time, τ, of $2.8(8)\times10^{-4}$ seconds. The two processes on cooling are nearly overlapping making it difficult isolate each process individually. Van Turnhout and Wübbenhorst developed a method of instead analyzing the derivative, $\partial\epsilon'/\partial \log \omega$, with respect to frequency to better resolve broad relaxations or separate multiple processes (Figure 58b). The two processes are much more evident and were again fit with a modified HN-function incorporating the derivative. The uncertainty of the relaxation process on heating was significantly reduced (τ = $2.0(3)\times10^{-4}$ s) while the two processes on cooling were able to be reasonably separated (τ_{HF} = $1.06(11)\times10^{-4}$ s and τ_{LF} = $7.2(28)\times10^{-3}$ s for the high- and low-frequency processes respectively). Because electron mobility is higher than ionic mobility, the high frequency process is likely associated with electronic conductivity (*i.e.*, polaronic lattice distortions).

Figure 58: (a) Real part of complex permittivity at 440 ºC when heating (open red squares) and cooling (open blue circles). (b) Derivative of the real part of complex permittivity with respect to the log of angular frequency.

Solid lines represent fits of the HN-function.

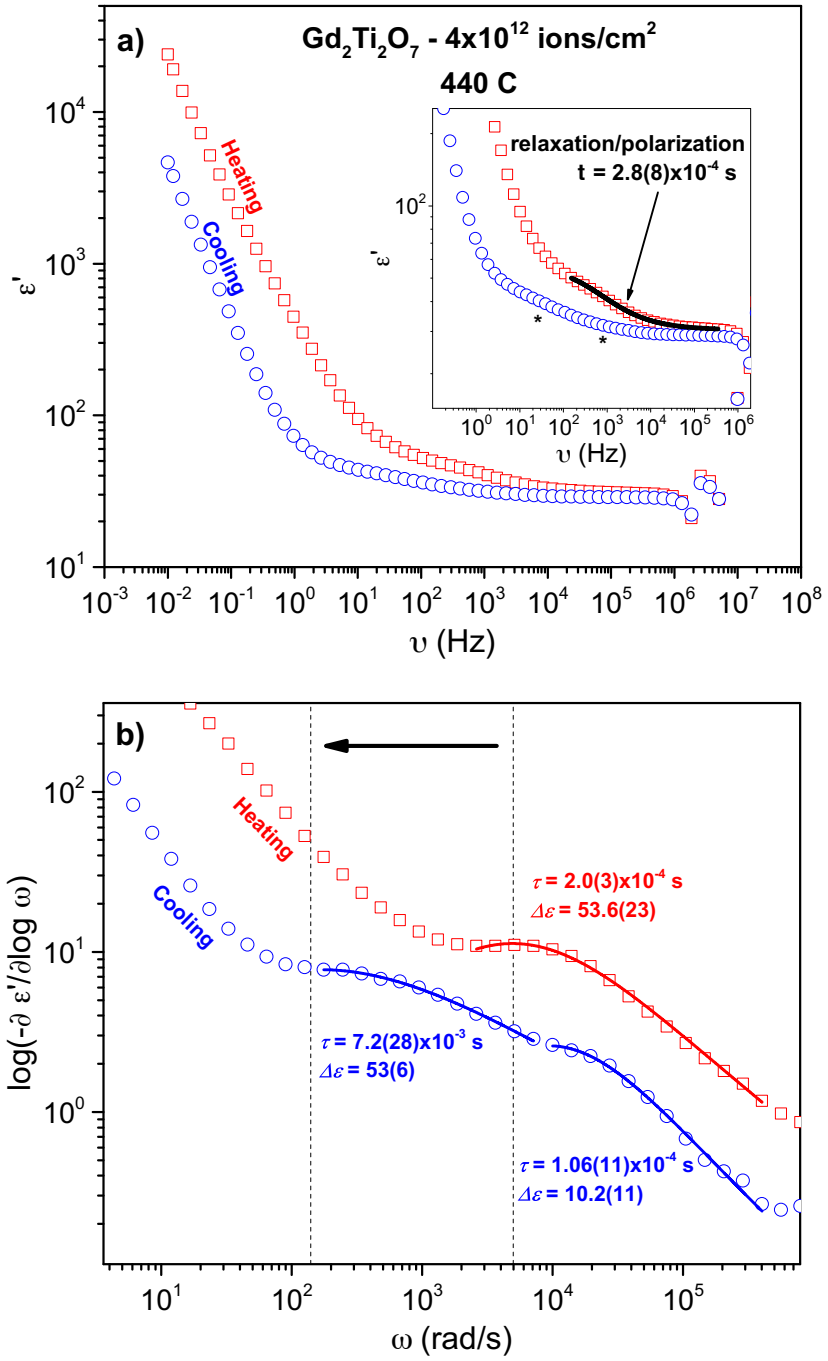

Figure 58. Continued.

The dielectric loss, $\Delta\epsilon$, on heating and the low frequency process on cooling have similar magnitudes (53.6(23) and 53(6) respectively) and likely correspond to the same process (ion hopping) but with shifted dynamics. This is further demonstrated through examining the real part of complex conductivity (Figure 59, top).

Complex conductivity, $\sigma^*(\omega)$, in many systems can be modeled by the random free energy barrier model [151]:

$$\boldsymbol{\sigma^*(\omega) = \sigma_{DC}\left[\frac{i\omega\tau}{\ln(1+i\omega\tau)}\right]} \quad (28)$$

where the DC conductivity, σ_{DC}, is limited by the largest energy barrier and $\sigma^*(\omega)$ is dependent on the attempt frequency, $(1/\tau)$, of the charge carriers to overcome this barrier. For ionic conductors, τ, corresponds to the mean time it takes for charge carriers to jump to adjacent sites (hopping time). This model can be decomposed into real and imaginary parts and fit to experimental data to obtain values for both σ_{DC} and τ (Figure 59, bottom). The hopping times associated with the bulk conductivity measured at 440 ºC when heating and cooling agree well with the relaxation times obtained from fitting the HN-function to $\partial\epsilon'/\partial\log\omega$ (Figure 59) confirming that they correspond to the same process: charge carrier hopping. The ion hopping time on heating ($2.0(1)\times10^{-4}$ s) is markedly faster than when measured on cooling ($8.0(2)\times10^{-3}$ s).

This different in ion hopping dynamics plays a large role in the increase in conductivity caused by swift heavy ion irradiation. As previously mentioned, ionic conductivity depends equally on charge carrier concentration and mobility. Explicitly determining mobility is complex and depends on a number of factors including charge carrier jump distance, double layer formation (interfacial/electrode polarization), and grain size among others.

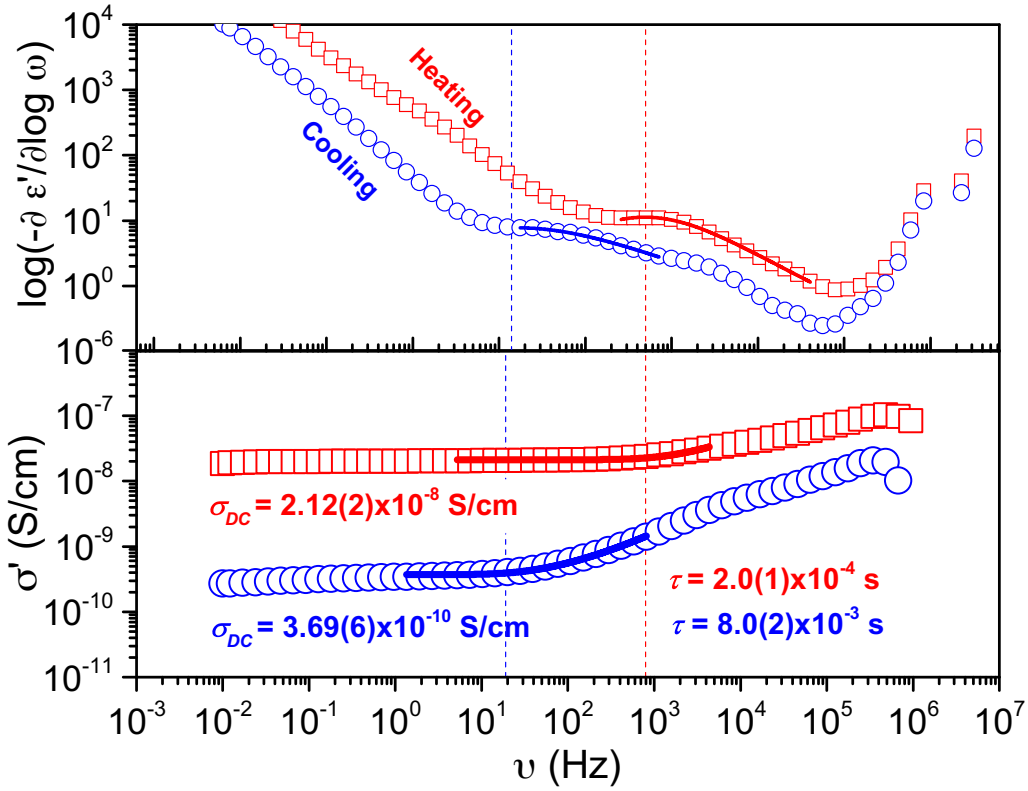

Figure 59: (top) Derivative of the real part of complex permittivity with respect to the log of angular frequency measured at 440 ºC when heating (red squares) and cooling (blue circles). (bottom) Real part of complex conductivity measured when heating (red squares) and cooling (blue circles).

Vertical dashed lines in each plot correspond to the characteristic hopping frequency obtained from fitting the HN-function (top, solid lines) and random free energy barrier model (bottom, solid lines) to the experimental data.

The hopping time on heating is ≈ 40 times faster than cooling. However, conductivity on heating is ≈ 57 times larger (in N_2) than cooling. Larger mobility in the amorphous phase therefore contributes to approximately 70% of the increase in conductivity while the other 30% is due to increased concentration of charge carriers.

Examining changes in relaxation/hopping time at temperatures above and below the Event 1 and Event 2 reveals the origin of the two discontinuities in conductivity on the atomic level (Figure 60). The derivative curves in Figure 60 were again fit with a modified HN-function to extract relaxation times and dielectric loss for each temperature. Despite the decrease in conductivity from 440 ºC to 460 ºC, the relaxation time associated with charge carrier hopping still decreases with increasing temperature as one would expect for an ionic conductor. Event 1 can therefore be primarily attributed to a decrease in charge carrier density. On the contrary, the relaxation time *increases* from 700 ºC to 740 ºC, signifying that charge carrier mobility in amorphous pyrochlore is higher than the crystalline pyrochlore.

The decrease in charge carrier density corresponding to Event 1 is particularly interesting because no ordering was previously seen in the average structure in that temperature range [146]. This suggests, although the average structure remains amorphous across this temperature range, multiple degrees of disorder may be present locally. This is confirmed through Raman spectroscopy measurements as a function of isochronal annealing temperature (Figure 61). The ordered pyrochlore structure contains six Raman-active modes [152]. In titanate pyrochlores, the two strongest bands are the E_g mode at 300 cm^{-1} attributed to O-Gd-O bending [152] and the A_{1g} mode at 500 cm^{-1} which is a 48*f* oxygen vibrational mode [153] (the spectra for irradiated $Gd_2Ti_2O_7$ annealed at 900 ºC is consistent with that of a pristine sample). After irradiation, the Raman modes corresponding to the pyrochlore structure have significantly dampened and new bands have formed.

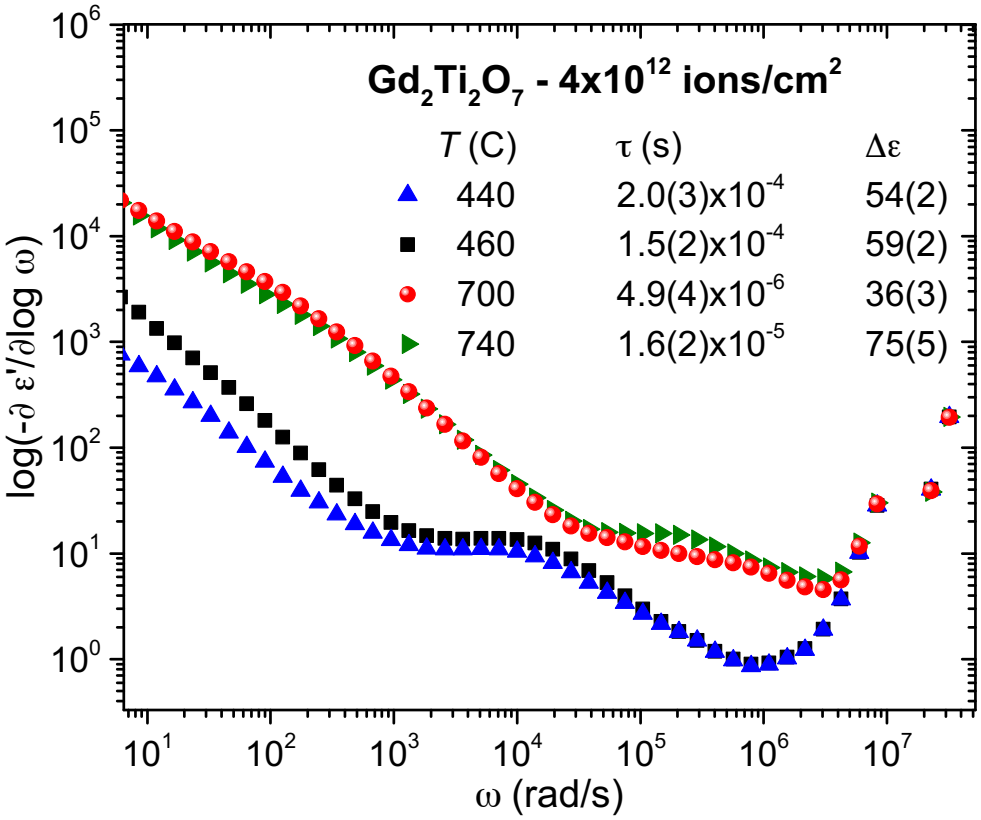

Figure 60: Derivative of the real part of complex permittivity with respect to the log of angular frequency measured before and after the two discontinuities in DC conductivity from Figure 57.

The spectra at all temperatures were fit with the modified HN-function. Hopping times and dielectric losses are displayed in the legend for each temperature.

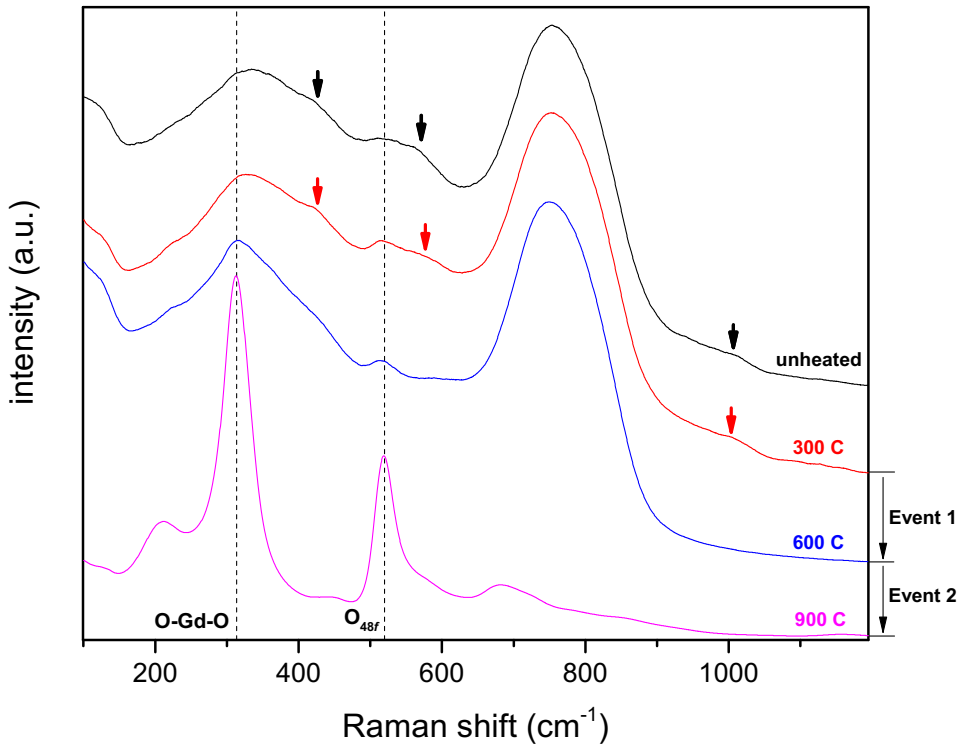

Figure 61: Raman spectra of irradiated $Gd_2Ti_2O_7$ as a function of isochronal annealing temperature

Tracy *et al.* have previously shown that, in the case of irradiated stannate pyrochlores, this is consistent with a transformation to a weberite-type arrangement [129]. While there is no observable change in the Raman spectra when annealed to 300 C, several features of the Raman spectra change when annealed at 600 C, a temperature that is above Event 1 but below Event 2 in air. In particular, weak bands at approximately 425 cm^{-1}, 600 cm^{-1}, and 1000 cm^{-1} disappear (see arrows in Figure 61) while the Raman modes associated with O-Gd-O bending and O_{48f} vibration significantly sharpen. This suggests a partial reordering of the oxygen sublattice which is consistent with the conclusions drawn from Figure 60 in which Event 1 was associated with a decrease in oxygen defect concentration. The O-Gd-O band also shifts to lower wavenumbers suggesting that local strain is partially relieved with Event 1. Upon heating to 900 C, the Raman spectra of an ordered titanate pyrochlore is recovered confirming that Event 2 is caused by an amorphous-to-crystalline transition.

Such a phenomenon in which there are varying degrees of disorder in amorphous materials has been seen experimentally in amorphous SiO_2 irradiated with Au and Xe ions of varying energies [154]. Despite already having a fully amorphous structure, well defined ion tracks were produced with an amorphous structure that was not coherent with that of the bulk sample. Similar mechanisms could be at play in amorphous pyrochlore in the present study. Here, low-temperature heating reorders local structural units without affecting longer length scales resulting in two distinct forms of disorder within an amorphous phase.

Defect annealing is often thought of as solely a thermal process. It is generally understood that defects confined inside a potential barrier must be supplied with enough kinetic energy to overcome this barrier. For example, in the case of Frenkel pairs, this is typically thought of as a “required temperature” that must be met before defects have enough energy to migrate and recombine. The fact that Event 1 and Event 2 occur at different temperatures depending on the atmosphere demonstrates that annealing is not only a thermal process but an

electronic process as well. A recent computational study on amorphization in select titanate pyrochlores, including $Gd_2Ti_2O_7$, found that large concentrations of electronic excitations, as would be present in irradiated materials, cause severe anion disorder and the formation of O_2-like molecules which subsequently disorders the cation arrangement thus driving the system into an amorphous state [67]. This supports an X-ray absorption study claiming that irradiated $Gd_2Ti_2O_7$ could be oxygen deficient and that redox effects can play a role in amorphization [117]. This could potentially explain why high electronic conductivity lowers the recrystallization temperature as free electrons are required to reduce the O_2-like molecules before they can recombine with a vacancy. This, of course, cannot be confirmed without a more detailed analysis into the energetics involved which would require more measurements as a function of atmosphere in which pO_2 is explicitly known.

CONCLUSION

Disorder in complex, $A_2B_2O_7$ oxides such as pyrochlore can be induced by in a variety of manners including changing the chemical composition, altering the stoichiometry, and irradiation with swift heavy ions. The effect on the average structure is complex and can lead to partial or complete loss of crystallinity. The work presented here demonstrates that despite differing behavior over longer length scales, the pyrochlore in prone to disorder to a lower symmetry, orthorhombic arrangement locally. Orthorhombic order can be induced locally, as seen in isometric defect-fluorite oxides, or in the long range structure which is observed in A_2TiO_5-type oxides. The magnetic properties of Dy_2TiO_5, with a long range orthorhombic structure, were determined with neutron diffraction and magnetic susceptibility measurements. Dy_2TiO_5 displays evidence of a 2D-3D magnetic transition and mixed Ising/Heisenberg magnetic order. The research shown here also demonstrates that ionic conductivity in $Gd_2Ti_2O_7$ can be increased by at least 250-fold using swift heavy ions to amorphize the structure. This was due to a combination of increased charge carrier concentration as well as increased mobility.

REFERENCES

1. Subramanian, M.A., G. Aravamudan, and G.V.S. Rao, *Oxide pyrochlores - a review.* Progress in Solid State Chemistry, 1983. **15**(2): p. 55-143.
2. Chakoumakos, B.C., *SYSTEMATICS OF THE PYROCHLORE STRUCTURE TYPE, IDEAL A2B2X6Y.* Journal of Solid State Chemistry, 1984. **53**(1): p. 120-129.
3. Yu, T.H. and H.L. Tuller, *Electrical conduction and disorder in the pyrochlore system (Gd1-xCax)(2)Sn2O7.* Journal of Electroceramics, 1998. **2**(1): p. 49-55.
4. Yonezawa, S., et al., *Superconductivity in a pyrochlore-related oxide KOs2O6.* Journal of Physics-Condensed Matter, 2004. **16**(3): p. L9-L12.
5. Hanawa, M., et al., *Superconductivity at 1 K in Cd2Re2O7.* Physical Review Letters, 2001. **87**(18).
6. Harris, M.J., et al., *Geometrical frustration in the ferromagnetic pyrochlore Ho2Ti2O7.* Physical Review Letters, 1997. **79**(13): p. 2554-2557.
7. Bramwell, S.T., et al., *Measurement of the charge and current of magnetic monopoles in spin ice.* Nature, 2009. **461**(7266): p. 956-U211.
8. Bramwell, S.T. and M.J.P. Gingras, *Spin ice state in frustrated magnetic pyrochlore materials.* Science, 2001. **294**(5546): p. 1495-1501.
9. Castelnovo, C., R. Moessner, and S.L. Sondhi, *Magnetic monopoles in spin ice.* Nature, 2008. **451**(7174): p. 42-45.
10. Wu, J., et al., *Low-thermal-conductivity rare-earth zirconates for potential thermal-barrier-coating applications.* Journal of the American Ceramic Society, 2002. **85**(12): p. 3031-3035.
11. Cao, X.Q., et al., *Thermal stability of lanthanum zirconate plasma-sprayed coating.* Journal of the American Ceramic Society, 2001. **84**(9): p. 2086-2090.
12. Wan, C.L., et al., *Order-Disorder Transition and Unconventional Thermal Conductivities of the (Sm1-xYbx)(2)Zr2O7 Series.* Journal of the American Ceramic Society, 2011. **94**(2): p. 592-596.
13. Saruhan, B., et al., *EB-PVD processing of pyrochlore-structured La2Zr2O7-based TBCs.* Surface & Coatings Technology, 2004. **182**(2-3): p. 175-183.
14. Lehmann, H., et al., *Thermal conductivity and thermal expansion coefficients of the lanthanum rare-earth-element zirconate system.* Journal of the American Ceramic Society, 2003. **86**(8): p. 1338-1344.
15. Ewing, R.C., *The design and evaluation of nuclear-waste forms: Clues from mineralogy.* Canadian Mineralogist, 2001. **39**: p. 697-715.
16. Ewing, R.C., W.J. Weber, and J. Lian, *Nuclear waste disposal-pyrochlore (A(2)B(2)O(7)): Nuclear waste form for the immobilization of plutonium and "minor" actinides.* Journal of Applied Physics, 2004. **95**(11): p. 5949-5971.
17. Weber, W.J., et al., *Radiation effects in crystalline ceramics for the immobilization of high-level nuclear waste and plutonium.* Journal of Materials Research, 1998. **13**(6): p. 1434-1484.

18. Heremans, C., et al., *FAST-ION CONDUCTING Y-2(ZRYTI1-Y)(2)O-7 PYROCHLORES - NEUTRON RIETVELD ANALYSIS OF DISORDER-INDUCED BY ZR SUBSTITUTION.* Journal of Solid State Chemistry, 1995. **117**(1): p. 108-121.
19. Heremans, C., et al., *FAST-ION CONDUCTION AND DISORDER IN CATION AND ANION ARRAYS IN Y2(ZRYTI1-Y)2O7 PYROCHLORES INDUCED BY ZR SUBSTITUTION - A NEUTRON RIETVELD ANALYSIS*, in *Solid State Ionics Iii*, G.A. Nazri, J.M. Tarascon, and M. Armand, Editors. 1993. p. 349-354.
20. Wuensch, B.J., et al., *Connection between oxygen-ion conductivity of pyrochlore fuel-cell materials and structural change with composition and temperature.* Solid State Ionics, 2000. **129**(1-4): p. 111-133.
21. Moon, P.K. and H.L. Tuller, *IONIC-CONDUCTION IN THE GD2TI2O7-GD2ZR2O7 SYSTEM.* Solid State Ionics, 1988. **28**: p. 470-474.
22. Tuller, H.L. and P.K. Moon, *FAST ION CONDUCTORS - FUTURE-TRENDS.* Materials Science and Engineering B-Solid State Materials for Advanced Technology, 1988. **1**(2): p. 171-191.
23. Sickafus, K.E., et al., *Radiation-induced amorphization resistance and radiation tolerance in structurally related oxides.* Nature Materials, 2007. **6**(3): p. 217-223.
24. Li, Y., et al., *Defect formation energies in A(2)B(2)O(7) pyrochlores.* Scripta Materialia, 2015. **107**: p. 18-21.
25. Sickafus, K.E., et al., *Radiation tolerance of complex oxides.* Science, 2000. **289**(5480): p. 748-751.
26. Zhang, F.X., et al., *Pressure-induced disordering and anomalous lattice expansion in La2Zr2O7 pyrochlore.* Physical Review Letters, 2010. **105**(1).
27. Zhang, F.X., et al., *Phase stability and pressure dependence of defect formation in Gd(2)Ti(2)O(7) and Gd(2)Zr(2)O(7) pyrochlores.* Physical Review Letters, 2008. **100**(4).
28. Trachenko, K., et al., *How the nature of the chemical bond governs resistance to amorphization by radiation damage.* Physical Review B, 2005. **71**(18).
29. Shepelev, Y.F. and M.A. Petrova, *Crystal Structures of Ln(2)TiO(5) (Ln = Gd, Dy) Polymorphs.* Inorganic Materials, 2008. **44**(12): p. 1354-1361.
30. Petrova, M.A. and R.G. Grebenshchikov, *Specific features of the phase formation in the titanate systems Ln(2)TiO(5)-Ln ' 2TiO5 (Ln = La, Gd, Tb, Er; Ln '= Tb, Lu).* Glass Physics and Chemistry, 2008. **34**(5): p. 603-607.
31. Tracy, C.L., et al., *Structural response of A(2)TiO(5) (A = La, Nd, Sm, Gd) to swift heavy ion irradiation.* Acta Materialia, 2012. **60**(11): p. 4477-4486.
32. Lian, J., et al., *Radiation-induced amorphization of rare-earth titanate pyrochlores.* Physical Review B, 2003. **68**(13).

33. Lian, J., et al., *Effect of structure and thermodynamic stability on the response of lanthanide stannate-pyrochlores to ion beam irradiation.* Journal of Physical Chemistry B, 2006. **110**(5): p. 2343-2350.
34. Lian, J., et al., *Nanoscale manipulation of pyrochlore: New nanocomposite ionic conductors.* Physical Review Letters, 2001. **87**(14).
35. Lian, J., et al., *Ion-irradiation-induced amorphization of La2Zr2O7 pyrochlore.* Physical Review B, 2002. **66**(5).
36. Norberg, S.T., et al., *Pyrochlore to fluorite transition: the Y-2(Ti1-xZrx)(2)O-7 (0.0 <= x <= 1.0) system.* Chemistry of Materials, 2012. **24**(22): p. 4294-4300.
37. Sanjuan, M.L., et al., *Raman and x-ray absorption spectroscopy study of the phase evolution induced by mechanical milling and thermal treatments in R2Ti2O7 pyrochlores.* Physical Review B, 2011. **84**(10).
38. Blanchard, P.E.R., et al., *Does local disorder occur in the pyrochlore zirconates?* Inorganic Chemistry, 2012. **51**(24): p. 13237-13244.
39. Mitamura, H., et al., *AGING EFFECTS ON CURIUM-DOPED TITANATE CERAMIC CONTAINING SODIUM-BEARING HIGH-LEVEL NUCLEAR WASTE.* Journal of the American Ceramic Society, 1992. **75**(2): p. 392-400.
40. Laverov, N.P., et al., *Effect of radiation on properties of confinement matrices for immobilization of actinide-bearing wastes.* Geology of Ore Deposits, 2003. **45**(6): p. 423-451.
41. Weber, W.J., J.W. Wald, and H. Matzke, *EFFECTS OF SELF-RADIATION DAMAGE IN CM-DOPED GD2TI2O7 AND CAZRTI2O7.* Journal of Nuclear Materials, 1986. **138**(2-3): p. 196-209.
42. Jiang, C., et al., *First-principles prediction of disordering tendencies in pyrochlore oxides.* Physical Review B, 2009. **79**(10).
43. Stanek, C.R. and R.W. Grimes, *Prediction of rare-earth A(2)Hf(2)O(7) pyrochlore phases.* Journal of the American Ceramic Society, 2002. **85**(8): p. 2139-2141.
44. Rushton, M.J.D., et al., *Predicted pyrochlore to fluorite disorder temperature for A(2)Zr(2)O(7) compositions.* Journal of Materials Research, 2004. **19**(6): p. 1603-1604.
45. Ushakov, S.V., et al., *Structure and Thermal Expansion of YSZ and La2Zr2O7 Above 1500 degrees C from Neutron Diffraction on Levitated Samples.* Journal of the American Ceramic Society, 2015. **98**(10): p. 3381-3388.
46. Itoh, N., et al., *Making tracks: electronic excitation roles in forming swift heavy ion tracks.* Journal of Physics-Condensed Matter, 2009. **21**(47).
47. Sattonnay, G., et al., *Structural stability of Nd2Zr2O7 pyrochlore ion-irradiated in a broad energy range.* Acta Materialia, 2013. **61**(17): p. 6492-6505.
48. Lang, M., et al., *Swift heavy ion track formation in Gd2Zr2-xTixO7 pyrochlore: Effect of electronic energy loss.* Nuclear Instruments & Methods

in Physics Research Section B-Beam Interactions with Materials and Atoms, 2014. **336**: p. 102-115.
49. Sattonnay, G., et al., *Phase transformations induced by high electronic excitation in ion-irradiated Gd-2(ZrxTi1-x)(2)O-7 pyrochlores.* Journal of Applied Physics, 2010. **108**(10).
50. Sattonnay, G., et al., *Effect of composition on the behavior of pyrochlores irradiated with swift heavy ions.* Nuclear Instruments & Methods in Physics Research Section B-Beam Interactions with Materials and Atoms, 2012. **272**: p. 261-265.
51. Lang, M., et al., *Structural modifications of Gd(2)Zr(2-x)Ti(x)O(7) pyrochlore induced by swift heavy ions: Disordering and amorphization.* Journal of Materials Research, 2009. **24**(4): p. 1322-1334.
52. Zhang, J., et al., *Nanoscale phase transitions under extreme conditions within an ion track.* Journal of Materials Research, 2010. **25**(7): p. 1344-1351.
53. Lang, M., et al., *Single-ion tracks in Gd2Zr2-xTixO7 pyrochlores irradiated with swift heavy ions.* Physical Review B, 2009. **79**(22).
54. Lang, M., et al., *Nanoscale manipulation of the properties of solids at high pressure with relativistic heavy ions.* Nature Materials, 2009. **8**(10): p. 793-797.
55. Tracy, C.L., et al., *Phase transformations in Ln(2)O(3) materials irradiated with swift heavy ions.* Physical Review B, 2015. **92**(17).
56. Benyagoub, A., *Phase transformations in oxides induced by swift heavy ions.* Nuclear Instruments & Methods in Physics Research Section B-Beam Interactions with Materials and Atoms, 2006. **245**(1): p. 225-230.
57. Lang, M., et al., *Advances in understanding of swift heavy-ion tracks in complex ceramics.* Current Opinion in Solid State & Materials Science, 2015. **19**(1): p. 39-48.
58. Meftah, A., et al., *TRACK FORMATION IN SIO2 QUARTZ AND THE THERMAL-SPIKE MECHANISM.* Physical Review B, 1994. **49**(18): p. 12457-12463.
59. Meftah, A., et al., *SWIFT HEAVY-IONS IN MAGNETIC INSULATORS - A DAMAGE-CROSS-SECTION VELOCITY EFFECT.* Physical Review B, 1993. **48**(2): p. 920-925.
60. Toulemonde, M., S. Bouffard, and F. Studer, *SWIFT HEAVY-IONS IN INSULATING AND CONDUCTING OXIDES - TRACKS AND PHYSICAL-PROPERTIES.* Nuclear Instruments & Methods in Physics Research Section B-Beam Interactions with Materials and Atoms, 1994. **91**(1-4): p. 108-123.
61. Apel, P., *Swift ion effects in polymers: industrial applications.* Nuclear Instruments & Methods in Physics Research Section B-Beam Interactions with Materials and Atoms, 2003. **208**: p. 11-20.

62. Toulemonde, M., et al., *Track formation and fabrication of nanostructures with MeV-ion beams.* Nuclear Instruments & Methods in Physics Research Section B-Beam Interactions with Materials and Atoms, 2004. **216**: p. 1-8.
63. Civale, L., et al., *Vortex confinement by columnar defects in yba2cu3o7 crystals - enhanced pinning at high fields and temperatures.* Physical Review Letters, 1991. **67**(5): p. 648-651.
64. Studer, F., et al., *SPONTANEOUS MAGNETIZATION INDUCED IN THE SPINEL ZNFE2O4 BY HEAVY-ION IRRADIATION IN THE ELECTRONIC STOPPING POWER REGIME.* Nuclear Instruments & Methods in Physics Research Section B-Beam Interactions with Materials and Atoms, 1993. **82**(1): p. 91-102.
65. Aidhy, D.S., et al., *Fast ion conductivity in strained defect-fluorite structure created by ion tracks in Gd2Ti2O7.* Scientific Reports, 2015. **5**.
66. Wang, J., et al., *Multi-scale simulation of structural heterogeneity of swift-heavy ion tracks in complex oxides.* Journal of Physics-Condensed Matter, 2013. **25**(13).
67. Xiao, H.Y., et al., *Electronic excitation induced amorphization in titanate pyrochlores: an ab initio molecular dynamics study.* Scientific Reports, 2015. **5**.
68. Lang, M., et al., *Review of A(2)B(2)O(7) pyrochlore response to irradiation and pressure.* Nuclear Instruments & Methods in Physics Research Section B-Beam Interactions with Materials and Atoms, 2010. **268**(19): p. 2951-2959.
69. Minh, N.Q., *CERAMIC FUEL-CELLS.* Journal of the American Ceramic Society, 1993. **76**(3): p. 563-588.
70. Steele, B.C.H. and A. Heinzel, *Materials for fuel-cell technologies.* Nature, 2001. **414**(6861): p. 345-352.
71. Wachsman, E.D. and K.T. Lee, *Lowering the Temperature of Solid Oxide Fuel Cells.* Science, 2011. **334**(6058): p. 935-939.
72. Ku, E.M., E.M.E. Yeo, and B.J. Wuensch, *Crystal chemistry of Y-2(ZrySn1-y)(2)O-7 pyrochlore solid solutions and its relation to fast-ion conduction*, in *Solid-State Chemistry of Inorganic Materials Ii*, S.M. Kauzlarich, et al., Editors. 1999. p. 327-332.
73. Kramer, S., M. Spears, and H.L. Tuller, *CONDUCTION IN TITANATE PYROCHLORES - ROLE OF DOPANTS.* Solid State Ionics, 1994. **72**: p. 59-66.
74. Kramers, S.A. and H.L. Tuller, *A NOVEL TITANATE-BASED OXYGEN-ION CONDUCTOR - GD2TI2O7.* Solid State Ionics, 1995. **82**(1-2): p. 15-23.
75. Tuller, H.L., *Ionic and mixed conductors: Materials design and optimization*, in *High Temperature Electrochemistry: Ceramics and Metals*, F.W. Poulsen, et al., Editors. 1996. p. 139-153.
76. Yu, T.H. and H.L. Tuller, *Ionic conduction and disorder in the Gd2Sn2O7 pyrochlore system.* Solid State Ionics, 1996. **86-8**: p. 177-182.

77. Williford, R.E., et al., *Effects of cation disorder on oxygen vacancy migration in Gd2Ti2O7.* Journal of Electroceramics, 1999. **3**(4): p. 409-424.
78. Pirzada, M., et al., *Oxygen migration in A(2)B(2)O(7) pyrochlores.* Solid State Ionics, 2001. **140**(3-4): p. 201-208.
79. Wilde, P.J. and C.R.A. Catlow, *Molecular dynamics study of the effect of doping and disorder on diffusion in gadolinium zirconate.* Solid State Ionics, 1998. **112**(3-4): p. 185-195.
80. Tuller, H.L., *MIXED IONIC ELECTRONIC CONDUCTION IN A NUMBER OF FLUORITE AND PYROCHLORE COMPOUNDS.* Solid State Ionics, 1992. **52**(1-3): p. 135-146.
81. Yang, F., et al., *Enhanced ionic conductivity in pyrochlore and fluorite mixed phase yttrium-doped lanthanum zirconate.* Journal of Power Sources, 2015. **273**: p. 290-297.
82. Bramwell, S.T., *MAGNETIC MONOPOLES Magnetricity near the speed of light.* Nature Physics, 2012. **8**(10): p. 703-704.
83. Keen, D.A. and A.L. Goodwin, *The crystallography of correlated disorder.* Nature, 2015. **521**(7552): p. 303-309.
84. Pauling, L., *The structure and entropy of ice and of other crystals with some randomness of atomic arrangement.* Journal of the American Chemical Society, 1935. **57**: p. 2680-2684.
85. Giblin, S.R., et al., *Creation and measurement of long-lived magnetic monopole currents in spin ice.* Nature Physics, 2011. **7**(3): p. 252-258.
86. Lau, G.C., et al., *Zero-point entropy in stuffed spin-ice.* Nature Physics, 2006. **2**(4): p. 249-253.
87. Lau, G.C., et al., *Stuffed rare earth pyrochlore solid solutions.* Journal of Solid State Chemistry, 2006. **179**(10): p. 3126-3135.
88. Ziegler, J.F., M.D. Ziegler, and J.P. Biersack, *SRIM - The stopping and range of ions in matter (2010).* Nuclear Instruments & Methods in Physics Research Section B-Beam Interactions with Materials and Atoms, 2010. **268**(11-12): p. 1818-1823.
89. Neuefeind, J., et al., *The Nanoscale Ordered MAterials Diffractometer NOMAD at the Spallation Neutron Source SNS.* Nuclear Instruments & Methods in Physics Research Section B-Beam Interactions with Materials and Atoms, 2012. **287**: p. 68-75.
90. Egami, T. and S.J.L. Billinge, *Underneath the Bragg Peaks: Structural Analysis of Complex Materials, 2nd Edition.* Underneath the Bragg Peaks: Structural Analysis of Complex Materials, 2nd Edition, 2012. **16**: p. 1-481.
91. Rodriguez-Carvajal, J., *FULLPROF version 1.2.7.* ILL (unpublished), 2009-2012.
92. Toby, B.H., *EXPGUI, a graphical user interface for GSAS.* Journal of Applied Crystallography, 2001. **34**: p. 210-213.
93. Jahn, H.A. and E. Teller, *Stability of polyatomic molecules in degenerate electronic states. I. Orbital degeneracy.* Proceedings of the Royal Society

of London Series a-Mathematical and Physical Sciences, 1937. **161**(A905): p. 220-235.
94. Salamon, M.B. and M. Jaime, *The physics of manganites: Structure and transport.* Reviews of Modern Physics, 2001. **73**(3): p. 583-628.
95. Farrow, C.L., et al., *PDFfit2 and PDFgui: computer programs for studying nanostructure in crystals.* Journal of Physics-Condensed Matter, 2007. **19**(33).
96. Wills, A.S., *A new protocol for the determination of magnetic structures using simulated annealing and representational analysis (SARAh).* Physica B, 2000. **276-278**: p. 680-681.
97. Moll, S., et al., *Swift heavy ion irradiation of pyrochlore oxides: Electronic energy loss threshold for latent track formation.* Nuclear Instruments & Methods in Physics Research Section B-Beam Interactions with Materials and Atoms, 2010. **268**(19): p. 2933-2936.
98. Wang, S.X., et al., *Radiation stability of gadolinium zirconate: A waste form for plutonium disposition.* Journal of Materials Research, 1999. **14**(12): p. 4470-4473.
99. Sattonnay, G., et al., *Phenomenological model for the formation of heterogeneous tracks in pyrochlores irradiated with swift heavy ions.* Acta Materialia, 2012. **60**(1): p. 22-34.
100. Zhang, J., et al., *Liquid-like phase formation in Gd2Zr2O7 by extremely ionizing irradiation.* Journal of Applied Physics, 2009. **105**(11).
101. Zhang, J.M., et al., *C-60 and U ion irradiation of Gd2TixZr2-xO7 pyrochlore.* Journal of Materials Research, 2015. **30**(16): p. 2456-2466.
102. Lang, M., et al., *Characterization of ion-induced radiation effects in nuclear materials using synchrotron x-ray techniques.* Journal of Materials Research, 2015. **30**(9): p. 1366-1379.
103. Hammersley, A.P., et al., *Two-dimensional detector software: From real detector to idealised image or two-theta scan.* High Pressure Research, 1996. **14**(4-6): p. 235-248.
104. Syassen, K., *DATLAB, version 1.29.* MPI/FKF Stuttgart, Germany.
105. Lang, M., et al., *Swift heavy ion-induced amorphization of CaZrO3 perovskite.* Nuclear Instruments & Methods in Physics Research Section B-Beam Interactions with Materials and Atoms, 2012. **286**: p. 271-276.
106. Toulemonde, M., et al., *Transient thermal processes in heavy ion irradiation of crystalline inorganic insulators.* Nuclear Instruments & Methods in Physics Research Section B-Beam Interactions with Materials and Atoms, 2000. **166**: p. 903-912.
107. Zinkle, S.J., V.A. Skuratov, and D.T. Hoelzer, *On the conflicting roles of ionizing radiation in ceramics.* Nuclear Instruments & Methods in Physics Research Section B-Beam Interactions with Materials and Atoms, 2002. **191**: p. 758-766.

108. Wang, S.X., et al., *Ion irradiation-induced phase transformation of pyrochlore and zirconolite.* Nuclear Instruments & Methods in Physics Research Section B-Beam Interactions with Materials and Atoms, 1999. **148**(1-4): p. 704-709.
109. Debye, P., *Interferenz von Röntgenstrahlen und Wärmebewegung.* Annalen der Physik, 1913. **348**(1): p. 49-92.
110. Waller, I., *On the question of the influence of thermal motion on the interference of X-rays.* Zeitschrift Fur Physik, 1923. **17**: p. 398-408.
111. Billinge, S.J.L. and M.G. Kanatzidis, *Beyond crystallography: the study of disorder, nanocrystallinity and crystallographically challenged materials with pair distribution functions.* Chemical Communications, 2004(7): p. 749-760.
112. Billinge, S.J.L. and I. Levin, *The problem with determining atomic structure at the nanoscale.* Science, 2007. **316**(5824): p. 561-565.
113. Padture, N.P., M. Gell, and E.H. Jordan, *Materials science - Thermal barrier coatings for gas-turbine engine applications.* Science, 2002. **296**(5566): p. 280-284.
114. Finkeldei, S., et al., *Dissolution of ZrO2 based pyrochlores in the acid pH range: A macroscopic and electron microscopy study.* Applied Geochemistry, 2014. **49**: p. 31-41.
115. King, G., et al., *Local structure of the vacancy disordered fluorite Yb3TaO7 from neutron total scattering.* Journal of Materials Chemistry A, 2013. **1**(35): p. 10487-10494.
116. Rooksby, H.P. and E.A.D. White, *Rare-earth niobates and tantalates of defect fluorite-type and weberite-type structures.* Journal of the American Ceramic Society, 1964. **47**(2): p. 94-96.
117. Walker, J.D.S., et al., *A case for oxygen deficiency in Gd2Ti2-xZrxO7 pyrochlore-type oxides.* Journal of Alloys and Compounds, 2013. **565**: p. 44-49.
118. Verwey, E.J.W. and E.L. Heilmann, *Physical properties and cation arrangement of oxides with spinel structures I. cation arrangement in spinels.* Journal of Chemical Physics, 1947. **15**(4): p. 174-180.
119. Sickafus, K.E., et al., *Cation disorder in high-dose, neutron-irradiated spinel.* Journal of Nuclear Materials, 1995. **219**: p. 128-134.
120. Redfern, S.A.T., et al., *Thermodynamics and kinetics of cation ordering in MgAl2O4 spinel up to 1600 degrees C from in situ neutron diffraction.* American Mineralogist, 1999. **84**(3): p. 299-310.
121. Asbrink, S., et al., *High-pressure phase of the cubic spinel NiMn2O4.* Physical Review B, 1998. **57**(9): p. 4972-4974.
122. Ivanov, V.G., et al., *Short-range B-site ordering in the inverse spinel ferrite NiFe2O4.* Physical Review B, 2010. **82**(2).
123. Jiang, C., et al., *Cation disorder in MgX2O4 (X = Al, Ga, In) spinels from first principles.* Physical Review B, 2012. **86**(2).

124. Soper, A.K. and E.R. Barney, *On the use of modification functions when Fourier transforming total scattering data.* Journal of Applied Crystallography, 2012. **45**: p. 1314-1317.
125. Shamblin, J., et al., *Probing disorder in isometric pyrochlore and related complex oxides.* Nat Mater, 2016. **advance online publication**.
126. Weber, W.J., *Models and mechanisms of irradiation-induced amorphization in ceramics.* Nuclear Instruments & Methods in Physics Research Section B-Beam Interactions with Materials and Atoms, 2000. **166**: p. 98-106.
127. Shamblin, J., et al., *Probing disorder in isometric pyrochlore and related complex oxides.* Nat Mater, 2016. **15**(5): p. 507-511.
128. Shamblin, J., et al., *Structural response of titanate pyrochlores to swift heavy ion irradiation.* Acta Materialia, 2016. **117**: p. 207-215.
129. Tracy, C.L., et al., *Role of composition, bond covalency, and short-range order in the disordering of stannate pyrochlores by swift heavy ion irradiation.* Physical Review B (in press), 2016.
130. Mumme, W.G. and A.D. Wadsley, *STRUCTURE OF ORTHORHOMBIC Y2TIO5 AN EXAMPLE OF MIXED 7- AND FIVEFOLD COORDINATION.* Acta Crystallographica Section B-Structural Crystallography and Crystal Chemistry, 1968. **B 24**: p. 1327-&.
131. Shlyakhtina, A.V., et al., *Ordering processes in Ln(2)TiO(5) (Ln = Dy-Lu): The role of thermal history.* Journal of Alloys and Compounds, 2009. **479**(1-2): p. 6-10.
132. Aughterson, R.D., et al., *Crystal chemistry of the orthorhombic Ln(2)TiO(5) compounds with Ln=La, Pr, Nd, Sm, Gd, Tb and Dy.* Journal of Solid State Chemistry, 2015. **227**: p. 60-67.
133. Jiang, Y., J.R. Smith, and G.R. Odette, *Prediction of structural, electronic and elastic properties of Y2Ti2O7 and Y2TiO5.* Acta Materialia, 2010. **58**(5): p. 1536-1543.
134. Ramirez, A.P., et al., *Zero-point entropy in 'spin ice'.* Nature, 1999. **399**(6734): p. 333-335.
135. Risovany, V.D., E.E. Varlashova, and D.N. Suslov, *Dysprosium titanate as an absorber material for control rods.* Journal of Nuclear Materials, 2000. **281**(1): p. 84-89.
136. Sinha, A. and B.P. Sharma, *Development of dysprosium titanate based ceramics.* Journal of the American Ceramic Society, 2005. **88**(4): p. 1064-1066.
137. Morris, D.J.P., et al., *Dirac Strings and Magnetic Monopoles in the Spin Ice Dy2Ti2O7.* Science, 2009. **326**(5951): p. 411-414.
138. Ueland, B.G., et al., *Magnetothermal study of a Dy-stuffed spin ice: Dy(2)(Dy(x)Ti(2-x))O(7-x/2).* Physical Review B, 2008. **77**(14).
139. Lau, G.C., et al., *Structural disorder and properties of the stuffed pyrochlore Ho2TiO5.* Physical Review B, 2007. **76**(5).

140. Fisher, M.E., *RELATION BETWEEN SPECIFIC HEAT AND SUSCEPTIBILITY OF AN ANTIFERROMAGNET.* Philosophical Magazine, 1962. **7**(82): p. 1731-&.
141. Warren, B.E., *X-ray diffraction in random layer lattices.* Physical Review, 1941. **59**(9): p. 693-698.
142. Greedan, J.E., *Geometrically frustrated magnetic materials.* Journal of Materials Chemistry, 2001. **11**(1): p. 37-53.
143. Wills, A.S., et al., *Two-dimensional short-range magnetic order in the tetragonal spinel Li2Mn2O4.* Chemistry of Materials, 1999. **11**(7): p. 1936-1941.
144. Knee, C.S., et al., *Two- and three-dimensional magnetic order in the layered cobalt oxychloride Sr2CoO3Cl.* Physical Review B, 2003. **68**(17).
145. Prescher, C. and V.B. Prakapenka, *DIOPTAS: a program for reduction of two-dimensional X-ray diffraction data and data exploration.* High Pressure Research, 2015. **35**(3): p. 223-230.
146. Park, S., et al., *Response of Gd2Ti2O7 and La2Ti2O7 to swift-heavy ion irradiation and annealing.* Acta Materialia, 2015. **93**(0): p. 1-11.
147. Fuentes, A.F., et al., *Synthesis of disordered pyrochlores, A(2)Ti(2)O(7) (A = Y, Gd and Dy), by mechanical milling of constituent oxides.* Solid State Sciences, 2005. **7**(4): p. 343-353.
148. Hayun, S., et al., *Energetics of stepwise disordering transformation in pyrochlores, RE2Ti2O7 (RE=Y, Gd and Dy).* Acta Materialia, 2012. **60**(10): p. 4303-4310.
149. Pandit, A.K., et al., *ELECTRICAL-CONDUCTIVITY, THERMOELECTRIC-POWER AND DIELECTRIC-CONSTANT OF A GD2TI2O7 SINGLE-CRYSTAL.* Journal of Materials Science, 1991. **26**(24): p. 6759-6763.
150. Havrilia.S and S. Negami, *A COMPLEX PLANE REPRESENTATION OF DIELECTRIC AND MECHANICAL RELAXATION PROCESSES IN SOME POLYMERS.* Polymer, 1967. **8**(4): p. 161-&.
151. Dyre, J.C., *THE RANDOM FREE-ENERGY BARRIER MODEL FOR AC CONDUCTION IN DISORDERED SOLIDS.* Journal of Applied Physics, 1988. **64**(5): p. 2456-2468.
152. Vandenborre, M.T., et al., *RARE-EARTH TITANATES AND STANNATES OF PYROCHLORE STRUCTURE - VIBRATIONAL-SPECTRA AND FORCE-FIELDS.* Journal of Raman Spectroscopy, 1983. **14**(2): p. 63-71.
153. Hess, N.J., et al., *Spectroscopic investigations of the structural phase transition in Gd2(Ti1-yZry)(2)O-7 pyrochlores.* Journal of Physical Chemistry B, 2002. **106**(18): p. 4663-4677.
154. Kluth, P., et al., *Fine Structure in Swift Heavy Ion Tracks in Amorphous SiO(2).* Physical Review Letters, 2008. **101**(17).

VITA

Thomas (Jacob) Shamblin was born on August 13, 1988 in Maryville, TN. He graduated from the University of Tennessee with a Bachelor of Science Degree in Nuclear Engineering in August of 2010. Following graduation, Jacob immediately began his graduate career at the University of Tennessee in professor Howard Hall's research group. He worked in conjunction with the US-Russian Plutonium Disposition Program at Oak Ridge National Laboratory. After earning his Master of Science in Nuclear Engineering in May of 2012, Jacob began working full time as a subcontractor at Oak Ridge National Laboratory through Primm Consulting. He returned to the University of Tennessee in January of 2014 to work in Professor Maik Lang's research group. He earned his Doctor of Philosophy Degree in August of 2016. During his graduate studies, Jacob published three papers as lead author in the journals *Nature Materials*, *Physical Review B*, and *Acta Materialia*. He was also a coauthor on several additional papers.